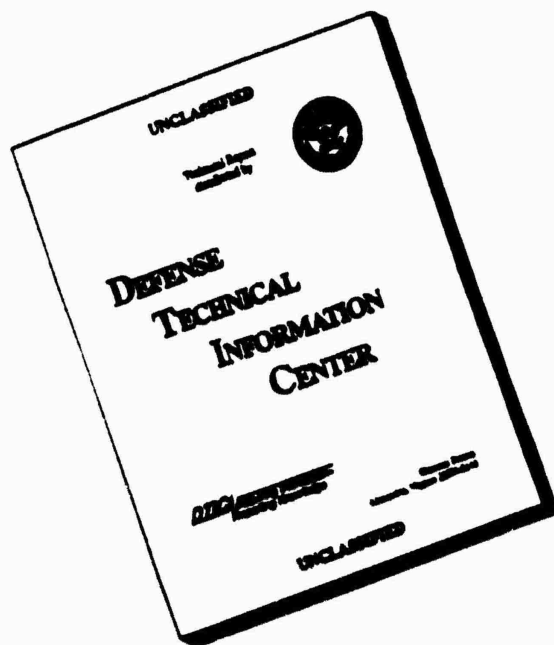


UNCLASSIFIED

AD NUMBER	
ADA076361	
CLASSIFICATION CHANGES	
TO:	UNCLASSIFIED
FROM:	SECRET
LIMITATION CHANGES	
TO: Approved for public release; distribution is unlimited. Document partially illegible.	
FROM: Distribution authorized to DoD only; Administrative/Operational Use; FEB 1954. Other requests shall be referred to Armed Forces Special Weapons Project, Sandia Base, Albuquerque, NM. Pre-dates formal DoD distribution statements. Treat as DoD only. Document partially illegible.	
AUTHORITY	
DSWA memo dtd 8 May 1998; DSWA memo dtd 8 May 1998	

THIS PAGE IS UNCLASSIFIED

# DISCLAIMER NOTICE

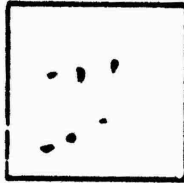


**THIS DOCUMENT IS BEST QUALITY AVAILABLE. THE COPY FURNISHED TO DTIC CONTAINED A SIGNIFICANT NUMBER OF PAGES WHICH DO NOT REPRODUCE LEGIBLY.**

PHOTOGRAPH THIS SHEET

AD A 076361

DTIC ACCESSION NUMBER



LEVEL



INVENTORY

AEC

WT-714

DOCUMENT IDENTIFICATION

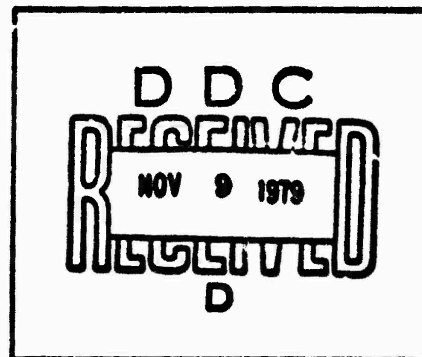
**DISTRIBUTION STATEMENT A**

Approved for public release;  
Distribution Unlimited

**DISTRIBUTION STATEMENT**

ACCESSION FOR	
NTIS	GRAB
DTIC	TAB
UNANNOUNCED	
JUSTIFICATION	
Per Hq. on Eila	
BY	
DISTRIBUTION /	
AVAILABILITY CODES	
DTIC	MAIL AND/OR SPECIAL
A	

DISTRIBUTION STAMP



DATE ACCESSIONED

DATE RECEIVED IN DTIC

PHOTOGRAPH THIS SHEET AND RETURN TO DTIC-DDA-2

UNCLASSIFIED

019064 354.2

WT-714

RECORDED **UNCLASSIFIED**

BY AUTHORITY OF AG 2374 (GAL) 67  
BY *Handwritten signature* 20 APR 1953

# Operation UPSHOT-KNOTHOLE

NEVADA PROVING GROUNDS

March - June 1953

RECORDED *Handwritten signature* 1954  
BY AUTHORITY OF *Handwritten signature* (Dec 59)  
BY *Handwritten signature*

Project 1.1d

DYNAMIC PRESSURE VS TIME AND SUPPORTING  
AIR BLAST MEASUREMENTS

11/12  
1000 100 9/10 1004

*[Large redacted block]*

HEADQUARTERS FIELD COMMAND, ARMED FORCES SPECIAL WEAPONS PROJECT  
SANDIA BASE, ALBUQUERQUE, NEW MEXICO

79 11 01 070

UNCLASSIFIED

FC *Handwritten signature*

AD A 076361





If this report is no longer needed, return it to  
AEC Technical Information Service  
P. O. Box 401  
Oak Ridge, Tennessee

WT-714

UNCLASSIFIED

This document consists of 116 pages

No. 1 of 225 copies, Series A

OPERATION UPSHOT-KNOTHOLE

Project 1.1d

DYNAMIC PRESSURE VS TIME AND SUPPORTING  
AIR BLAST MEASUREMENTS

REPORT TO THE TEST DIRECTOR

by

C. D. Broyles

RECORDED  
BY AUTHORITY OF  
SR 1238 (9/2/57)  
K. [Signature]

February 1954

per telecon w/Betty Fox (DNA Tech Libr, Chief), the  
classified references contained herein may remain.

P. C. Chance (DDA-2)  
9-5-79

UNCLASSIFIED

Sandia Corporation  
Albuquerque, New Mexico

UNCLASSIFIED

ABSTRACT

Project 1.1d of Operation UPSHOT-KNOTHOLE measured dynamic pressures in the shock wave and preshock pressures. It also conducted a feasibility study of new and modified gages to measure dynamic pressure, density, temperature, and particle velocity.

Measured dynamic pressures can be compared with those calculated from the measured overpressures using the Rankine-Hugoniot shock relations and regular reflection theory. When no precursor is formed, measured dynamic pressures are in reasonable agreement with those calculated although some effects of thermal and mechanical interaction are noted. Dynamic pressures measured in the precursor are much higher than those calculated. Laboratory tests have indicated that the end instrument used does respond to dust as well as to air, and the quantity measured by these gages is apparently  $(\frac{1}{2} \rho u^2)_{\text{air}} + (\rho u^2)_{\text{dust}}$  when dust is present in the shock wave, as is true in the precursor.

Measurements have shown a few instances of real but small preshock increases in air pressure, all apparently caused by thermal radiation alone.

Results of the gage feasibility study indicate that the q-tube (dynamic pressure) and the centripetal density gage are suitable for use on full-scale nuclear tests. Both the modified sonic wind and sound speed indicator and the whistle temperature gage must be subjected to further modification before they are suitable for field use.

UNCLASSIFIED



UNCLASSIFIED

#### FOREWORD

This report is one of the reports presenting the results of the 78 projects participating in the Military Effects Tests Program of Operation UPSHOT-KNOTHOLE, which included 11 test detonations. For readers interested in other pertinent test information, reference is made to WT-782, Summary Report of the Technical Director, Military Effects Program. This summary report includes the following information of possible general interest.

- a. An over-all description of each detonation, including yield, height of burst, ground zero location, time of detonation, ambient atmospheric conditions at detonation, etc., for the 11 shots.
- b. Compilation and correlation of all project results on the basic measurements of blast and shock, thermal radiation, and nuclear radiation.
- c. Compilation and correlation of the various project results on weapons effects.
- d. A summary of each project, including objectives and results.
- e. A complete listing of all reports covering the Military Effects Tests Program.

UNCLASSIFIED

UNCLASSIFIED

CONTENTS

ABSTRACT . . . . .	3
FOREWORD . . . . .	5
LIST OF ILLUSTRATIONS . . . . .	9
LIST OF TABLES . . . . .	11
CHAPTER 1 DYNAMIC PRESSURE . . . . .	13
1.1 Objective . . . . .	13
1.2 Theory and Background . . . . .	13
1.2.1 Theory . . . . .	13
1.2.2 Earlier Experimental Measurements . . . . .	15
1.3 Instrumentation . . . . .	17
1.3.1 The Pitot-Static Gage . . . . .	17
1.3.2 Yawmeters . . . . .	19
1.3.3 Tower Accelerometers . . . . .	19
1.3.4 The Recording System . . . . .	19
1.4 Experimental Design . . . . .	19
1.4.1 Gage Coding System . . . . .	19
1.4.2 Shot 1 . . . . .	23
1.4.3 Shot 9 . . . . .	24
1.4.4 Shot 10 . . . . .	24
1.4.5 Shot 11 . . . . .	27
1.5 Results and Discussion . . . . .	27
1.5.1 Presentation of Results . . . . .	27
1.5.2 Dynamic Pressures in the Regular and Mach Reflection Regions (no Precursor) . . . . .	34
1.5.3 Dynamic Pressures in the Precursor Region . . . . .	38
1.5.4 Dynamic Pressures in Secondary Shocks . . . . .	43
1.6 Conclusions and Recommendations . . . . .	45
CHAPTER 2 FRESHOCK PRESSURE MEASUREMENTS . . . . .	47
2.1 Objective . . . . .	47
2.2 Background . . . . .	47
2.3 Instrumentation . . . . .	47
2.4 Results and Discussion . . . . .	47

UNCLASSIFIED

UNCLASSIFIED

2.4.1	Shot 9 . . . . .	47
2.4.2	Shot 10 . . . . .	48
2.5	Conclusions and Recommendations . . . . .	51
CHAPTER 3 GAGE EVALUATION AND SUPPORTING AIR BLAST MEASUREMENTS. .		52
3.1	Scope and Design of the Experiment . . . . .	52
3.2	Centripetal Density Gage . . . . .	52
3.2.1	Background . . . . .	52
3.2.2	Instrumentation . . . . .	56
3.2.3	Results and Discussion . . . . .	56
3.2.4	Conclusions and Recommendations . . . . .	60
3.3	q-Tube . . . . .	60
3.3.1	Background . . . . .	60
3.3.2	Instrumentation . . . . .	62
3.3.3	Results and Discussion . . . . .	62
3.3.4	Conclusions and Recommendations . . . . .	66
3.4	Whistle Temperature Gage . . . . .	67
3.4.1	Background . . . . .	67
3.4.2	Instrumentation . . . . .	67
3.4.3	Results and Discussion . . . . .	69
3.4.4	Conclusions and Recommendations . . . . .	69
3.5	Sonic Wind and Sound Speed Indicator (SWASSI) . . . . .	73
3.5.1	Background and Theory . . . . .	73
3.5.2	Instrumentation . . . . .	73
3.5.3	Results and Discussion . . . . .	74
3.5.4	Conclusions and Recommendations . . . . .	75
APPENDIX A ABBREVIATIONS AND SYMBOLS . . . . .		76
APPENDIX B SUMMARY DATA FOR OPERATION UPSHOT-KNOTHOLE . . . . .		78
APPENDIX C MEASURED WAVEFORMS, SHOTS 1, 9, AND 10 . . . . .		79
APPENDIX D PRELIMINARY INVESTIGATION OF THE RESPONSE OF PRES- SURE GAGES TO DUST-LADEN AIR . . . . .		89
APPENDIX E DYNAMIC PRESSURES IN DUST-LADEN SHOCKS . . . . .		105
REFERENCES . . . . .		112

UNCLASSIFIED

# UNCLASSIFIED

## LIST OF ILLUSTRATIONS

Fig. 1.1	Dynamic Pressure Height-of-Burst Chart ( $q = \frac{1}{2}\rho u^2$ ) . . .	16
Fig. 1.2	Detail Drawing of Pitot-Static Gage . . . . .	18
Fig. 1.3	Wind-Tunnel Calibration -- Pitot-Static Gage, Yaw Angle . . . . .	20
Fig. 1.4	Wind-Tunnel Calibration -- Pitot-Static Gage, Pitch Angle . . . . .	21
Fig. 1.5	Wind-Tunnel Calibration -- Pitot-Static Gage, Mach Number . . . . .	22
Fig. 1.6	Pitot-Static Gage Mounted on 10-ft Tower at Station J-284 on Shot 1 . . . . .	23
Fig. 1.7	Layout of Blast Line, U-K Shots 9 and 10 . . . . .	25
Fig. 1.8	Pitot-Static Gage at Station F-214, Mounted to Measure Vertical Flow . . . . .	26
Fig. 1.9	Pitot-Static Gage at the 10-ft Level at Station F-280 . . . . .	26
Fig. 1.10	Preshot View of Pitot-Static Gages at the 10-, 35-, and 60-ft Levels in the Tree Stand for Shot 9 . . . . .	27
Fig. 1.11	Representative Dynamic Pressure- and Overpressure- Time Waveforms . . . . .	35
Fig. 1.12	Comparison of Measured and Calculated Dynamic Pressures on Shot 9 . . . . .	39
Fig. 1.13	Remains of Pitot-Static Gage from Station J-285, Shot 1 . . . . .	41
Fig. 1.14	Post-Shot View of Station F-200, Shot 10 . . . . .	41
Fig. 1.15	Comparison of Dynamic Pressures Measured in the Precursor with Dynamic Pressure-Distance Curves from Porzel (Fig. 1.1) . . . . .	44
Fig. 2.1	Preshot Pressure-Time Waveforms from Shots 9 and 10 . . . . .	50
Fig. 3.1	Views of Experimental Gages Installed in the Field . . .	53

UNCLASSIFIED

UNCLASSIFIED

Fig. 3.2	Temperature-Time Waveforms, Resistance Temperature Gage . . . . .	55
Fig. 3.3	Detail Drawing, Centripetal Density Gage . . . . .	57
Fig. 3.4	Diaphragm-Type Differential Pressure Transducer . . . . .	58
Fig. 3.5	Density and Static Pressure Gages in Side-On Baffle in Field . . . . .	58
Fig. 3.6	Density-Time and Overpressure-Time Waveforms from Centripetal Density Gage . . . . .	61
Fig. 3.7	Detail Drawing of Sensing Element for q-Tube . . . . .	63
Fig. 3.8	Dynamic Pressure-Time Waveforms from q-Tube . . . . .	65
Fig. 3.9	Post-Shot View of Station 3-289 . . . . .	66
Fig. 3.10	Block Diagram Showing Operation of Whistle Temperature Gage . . . . .	68
Fig. 3.11	Detail Drawing of Whistle Temperature Gage . . . . .	70
Fig. 3.12	Whistle Gage Mounted in the Field with Dust Cover Removed . . . . .	71
Fig. 3.13	Detail Drawing of Siren Sound Source for SWASSI . . . . .	72
Fig. C.1	Pressure-Time Waveforms -- Pitot-Static Gage, Shot 1 . . . . .	80
Fig. C.2	Dynamic Pressure-Time Waveforms -- Pitot-Static Gage, Shot 9 . . . . .	81
Fig. C.3	Dynamic Pressure-Time Waveforms -- Pitot-Static Gage, Shot 9 . . . . .	82
Fig. C.4	Overpressure-Time Waveforms -- Pitot-Static Gage, Shot 9 . . . . .	83
Fig. C.5	Overpressure-Time Waveforms -- Pitot-Static Gage, Shot 9 . . . . .	84
Fig. C.6	Pressure-Time Waveforms in Precursor -- Pitot-Static Gage, Shot 10 . . . . .	85
Fig. C.7	Pressure-Time Waveforms in Precursor -- Pitot-Static Gage, Shot 10 . . . . .	86
Fig. C.8	Pressure-Time Waveforms (Nonprecursor) -- Pitot- Static Gage, Shot 10 . . . . .	87
Fig. C.9	Acceleration, Velocity, and Displacement Waveforms -- Shots 1 and 10 . . . . .	88
Fig. D.1	Cross-Sectional Views of Wiancko and Rutishauser Gages . . . . .	91
Fig. D.2	Diagram of the Experimental Arrangement . . . . .	92
Fig. D.3	Some Wiancko and Rutishauser Records . . . . .	98

10 UNCLASSIFIED



UNCLASSIFIED

LIST OF TABLES

TABLE 1.1	Dynamic Pressure, Pitot-Static Gage, Shot 1 . . . . .	28
TABLE 1.2	Overpressure, Pitot-Static Gage, Shot 1 . . . . .	28
TABLE 1.3	Dynamic Pressure, Pitot-Static Gage, Shot 9 . . . . .	29
TABLE 1.4	Overpressure, Pitot-Static Gage, Shot 9 . . . . .	30
TABLE 1.5	Dynamic Pressure, Pitot-Static Gage, Shot 10 . . . . .	31
TABLE 1.6	Overpressure, Pitot-Static Gage, Shot 10 . . . . .	31
TABLE 1.7	Dynamic Pressure and Overpressure, Pitot-Static Gage, Shot 11 . . . . .	32
TABLE 1.8	Wind Direction, Yawmeter . . . . .	32
TABLE 1.9	Tower Acceleration Measurements . . . . .	33
TABLE 1.10	Comparison of Measured and Calculated Dynamic Pressures in the Region of no Precursor . . . . .	37
TABLE 1.11	Comparison of Measured and Calculated Dynamic Pressures in Precursor Region . . . . .	43
TABLE 2.1	Free Shock Pressure Measurements . . . . .	49
TABLE 3.1	Shock Temperatures, Resistance Temperature Gage . . . . .	54
TABLE 3.2	Density, Centripetal Density Gage . . . . .	59
TABLE 3.3	Overpressure, Centripetal Density Gage . . . . .	59
TABLE 3.4	Dynamic Pressures, q-Tube . . . . .	64
TABLE 3.5	Comparison of Measured and Calculated Dynamic Pressures, q-Tube . . . . .	64
TABLE 3.6	Temperatures, Whistle Temperature Gage . . . . .	71
TABLE 3.7	Sound and Wind Velocities, SWASSI . . . . .	74
TABLE D.1	Computed Characteristics of the Clean Shock After Passing Through the Screen . . . . .	93
TABLE D.2	Times Required for Smooth Spheres to Reach Various Fractions of the Air Velocity . . . . .	95

UNCLASSIFIED 11

TABLE D.3	Summary of Experimental Data . . . . .	100
TABLE D.4	Average Peak Dynamic Pressures for Strong Shocks and $\text{SiO}_2$ . . . . .	101
TABLE D.5	Summary of Dynamic Impulse Calculations . . . . .	103
TABLE E.1	Dynamic Pressure Ratios for Various Dust Densities and Shock Strengths . . . . .	110

~~FORMERLY RESTRICTED DATA~~

**UNCLASSIFIED**

# SECRET

## CHAPTER 1

### DYNAMIC PRESSURE

#### 1.1 OBJECTIVE

This phase of Project 1.1d of Operation UPSHOT-KNOTHOLE was designed to measure experimentally, near ground level, the dynamic pressures associated with blast waves from nuclear explosions. At the request of the conducting agencies special measurements of dynamic pressure were also made in conjunction with studies of the effects of blast on bridge structures (Project 3.4) and tree stands (Project 3.19).

Past practice in formulating blast damage criteria has been to associate damage to targets with a specific overpressure level.<sup>1</sup> It must be recognized, however, that damage to wind-sensitive targets such as towers, bridges, and trees is almost entirely a function of dynamic pressure level and that dynamic pressure may also play a significant role in damage to targets normally thought of as overpressure-sensitive. The validity of using overpressure alone as a damage criterion, especially for wind-sensitive targets, depends upon the existence of a unique relation between overpressure and dynamic pressure in the region of interest. For a single shock wave the Rankine-Rugoniot shock relations<sup>2</sup> show that a unique relation does exist. For shock waves reflected from plane surfaces this relation is no longer one between overpressure and dynamic pressure alone, but is also a function of the angle of incidence of the shock wave.

#### 1.2 THEORY AND BACKGROUND

##### 1.2.1 Theory

The Rankine-Rugoniot shock relations permit us to write, for shocks in air,

$$q = \frac{1}{2} \rho u^2 = 2.5 \frac{(\Delta P)^2}{7P_0 + \Delta P} \quad (1.1)$$

where  $q$  is dynamic pressure,  $\rho$  is air density,  $u$  is air velocity,  $P_0$  is ambient pressure, and  $\Delta P$  is overpressure. Either of two basic assumptions regarding the behavior of a shock wave may be used to derive the conservation equations of mass, momentum, and energy which are used to

UNCLASSIFIED

~~SECRET~~  
~~FORMERLY RESTRICTED DATA~~  
~~Handwritten: Handle As Restricted Data In Force~~  
~~SECRET~~



This relation and Figs. 4.b and 5.b of Polachek and Seeger provide a straightforward means of calculating  $q$  in the region of regular reflection. Experimentally measured  $q$ 's may then be compared with  $q$ 's calculated from the measured incident overpressures and from the angles of incidence computed from the relative positions of the burst point and the gage. Such a comparison will be not simply a check on the validity of the Rankine-Hugoniot relations but will be indicative of the combined effects upon the reflection process of such factors as thermal gradients, dust, nonrigidity of the reflecting surface, and the characteristic decaying nature of the shock wave itself.

Theoretical values for various parameters of the shock front can be computed from the Rankine-Hugoniot shock relations; conditions at the shock front may then be used as initial conditions to calculate these parameters for the portion of the wave behind the front from the equations for isentropic flow. Forzel<sup>8/</sup> has given these theoretical values of overpressure, dynamic pressure, particle velocity, and density, both at the shock front and behind it, for the expansion of a blast wave into free air, that is, into a homogeneous atmosphere containing no perturbing influences. Because of the complicated interactions inherent in the reflection process, theoretical values for these parameters have not been calculated throughout the shock wave in the regions of regular and Mach reflection. All experimental measurements presented here were made near the ground and therefore in the regions of regular or Mach reflection. Consequently any comparison of measured and theoretical dynamic pressures must be limited to peak values.

Forzel also presents theoretical height-of-burst charts for overpressures and dynamic pressures at the shock front; that for dynamic pressure is presented as Fig. 1.1. The horizontal component of dynamic pressure, after reflection in the regular reflection region, is given here. We can see from this figure that regular reflection leads to reduction of dynamic pressures at small ground distances from ground zero for airbursts; therefore choosing a height of burst to maximize the radius of a given dynamic pressure level will result in an inner circle in which dynamic pressures are smaller than desired. This circle may, in fact, be quite large.

Formation of a precursor shock wave can have a decided influence on dynamic pressures in both the regular and Mach reflection regions. While there is general agreement<sup>8,9,10/</sup> regarding the phenomenon leading to precursor formation, ie, a heated layer of air near the earth's surface, the theoretical description of its effect on dynamic pressure is incomplete. In his discussion of the dynamic pressure height-of-burst chart Forzel asserts that "Theoretical considerations indicate that to a fair approximation, the height-of-burst curves for dynamic pressures are applicable to all types of surfaces". A theoretical and experimental investigation of the problem by J. R. Banister and the author (App D, E) has shown that measured dynamic pressures are affected by the presence of large quantities of suspended dust.

#### 1.2.2 Earlier Experimental Measurements

Dynamic pressure measurements on Operation TUMBLER-SNAPPER<sup>11/</sup>

15

~~CONFIDENTIAL RESTRICTED DATA~~

~~CONFIDENTIAL RESTRICTED DATA~~  
Section 44B Atomic  
-SECRET-  
-SECRET-

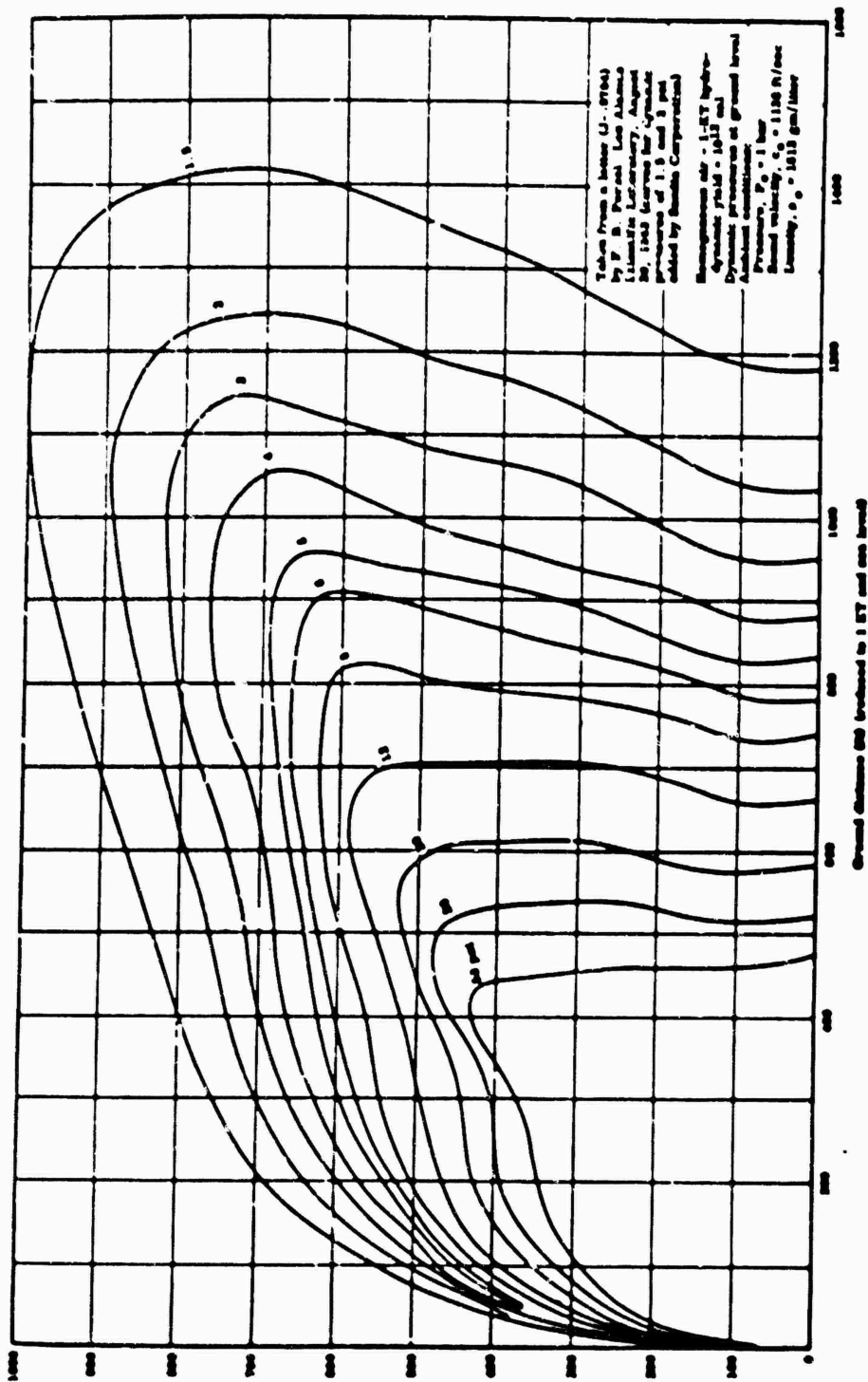


Fig. 1.1 -- Dynamic Pressure Height-of-Burst Chart ( $q = \frac{1}{2} \rho u^2$ )

FORMERLY RESTRICTED DATA  
 UNCLASSIFIED

Hydrodynamic Section 1.1.1  
 Distribution Section 1.1.1

and IVY<sup>12/</sup> using the pitot-static gage (Section 1.3) gave valid experimental values covering an overpressure range of 1-20 psi. When these measured dynamic pressures were compared with those calculated from the corresponding measured overpressures, no systematic trend of differences as a function of overpressure could be found; 9 were greater and 5 smaller than those calculated from the overpressures, deviations ranging from -25 to +35 per cent. The algebraic mean deviation was +3 per cent, and the RMS deviation 17 per cent. This algebraic mean deviation is not significant because of the small number of values and the wide spread in deviations. The logarithmic derivative of Eq 1.1,

$$\frac{dq}{q} = \left[ 2 - \frac{\Delta P}{7P_0 + \Delta P} \right] \frac{d\Delta P}{\Delta P}, \quad (1.4)$$

shows that the fractional error in  $q$  approaches twice the fractional error in  $\Delta P$  as  $\Delta P$  approaches zero. For  $\Delta P/P_0 = 1$ ,  $dq/q = 1.875 d\Delta P/\Delta P$ , and errors of 10 per cent in  $\Delta P$  correspond to errors of the order of 20 per cent in  $q$ .

### 1.3 INSTRUMENTATION

#### 1.3.1 The Pitot-Static Gage

This gage (Fig. 1.2) was selected as the instrument for dynamic pressure measurements on the basis of feasibility tests<sup>11/</sup> conducted during Operation TUMBLER-SNAPPER. Essentially it is a double-ended pitot-static tube on a mounting stem. It contains a front and a rear differential gage, each connected between a pitot opening at the end of the tube and a static pressure opening on the side of the tube six inches from the end. Ideally, for flow along the axis of the pitot tube, the differential gage responds to the difference in pressure,<sup>11,13/</sup>

$$q_c = P_t - P_s = q (1 + 0.25 M^2 + 0.025 M^4 + \dots)$$

where  $P_t$  = total or stagnation pressure

$P_s$  = free-stream static pressure

$M$  = local Mach number of flow = velocity of air divided by local speed of sound.

For this series of measurements only the front differential gage was used, and no attempt was made to measure dynamic pressures in the negative phase. A gage which reads static pressure alone is also connected to the static pressure orifices.

Actual pressures at the total and static pressure inlets are dependent upon the angle between the direction of flow and the axis of the tube as well as upon the Mach number of the air flow in more ways than the above formula suggests. Although the pitot-static gage had

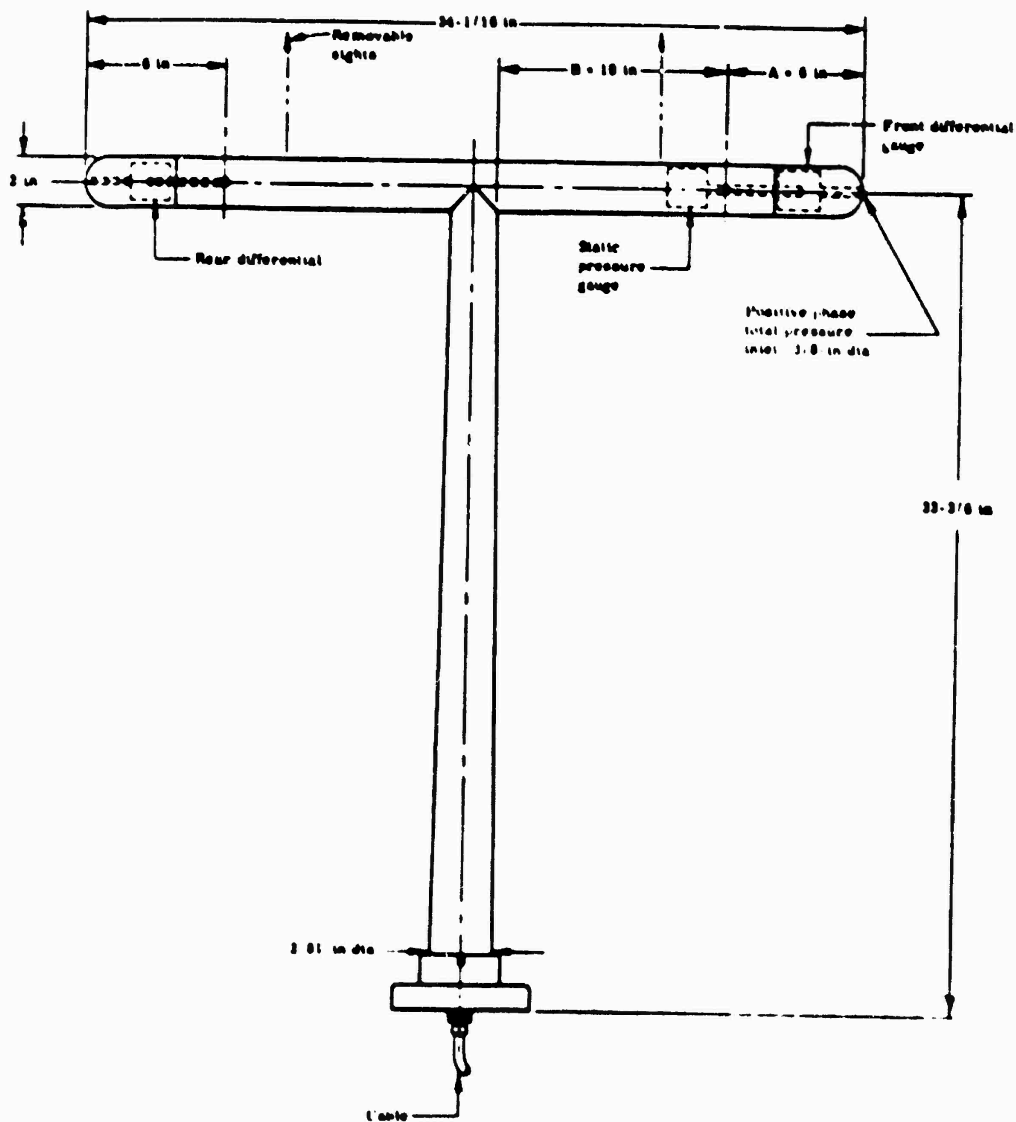


Fig. 1.2 -- Detail Drawing of Pitot-Static Jage

**UNCLASSIFIED**



been calibrated in previous wind-tunnel tests,<sup>11/</sup> it was recalibrated under more realistic conditions -- a larger range of Mach number and of yaw and pitch angles. Yaw angle ( $\psi$ ) is defined here as the angle in the plane normal to the mounting stem between the wind direction and axis of the pitot-static tube (Fig. 1.3); pitch angle ( $\theta$ ) is the corresponding angle in the plane of the mounting stem and the pitot-static tube (Fig. 1.4). The relations between actual measured differential pressure,  $q_m$ , and  $q_c$  as well as between measured static pressure,  $P_m$ , and free-stream static pressure,  $P_s$ , are presented in Figs. 1.3, 1.4, and 1.5 as functions of  $\psi$ ,  $\theta$ , and Mach number. Calibration covered  $\psi$ 's ranging from  $-30^\circ$  to  $+30^\circ$ ,  $\theta$ 's ranging from  $-45^\circ$  to  $+45^\circ$ , and Mach numbers of 0.1 to 0.9. Asymmetry of the resulting curves is largely traceable to the design of the static-pressure orifices, which can be improved by redesign. Calibration is accurate to within 1 per cent.

### 1.3.2 Yawmeters

Yawmeters<sup>11/</sup> were used to determine the direction of the blast winds. In this yawmeter pressure orifices at the end points of two orthogonal radii of a sphere are connected to a differential pressure gage whose record is calibrated to provide a measure of wind direction.

### 1.3.3 Tower Accelerometers

Wiancko accelerometers<sup>14/</sup> were used to measure radial acceleration of the towers to which the gages were mounted so that the behavior of the gages could be evaluated. The accelerometers were placed at the 10-ft level in regions where overpressures were expected to be high.

### 1.3.4 The Recording System

To record the data, electrical signals from the gages were fed through individual information cables to a Consolidated Recording System D in an underground shelter; the Consolidated galvanometer recorders were backed up in parallel by Ampex magnetic tape recorders (Model S-3128). A detailed description of this recording system is presented in the Sandia Corporation operational report on UFSROT-KNOTHOLE.<sup>15/</sup>

## 1.4 EXPERIMENTAL DESIGN

### 1.4.1 Gage Coding System

The coding system used to identify gages at various locations was similar to that used by other agencies. The first two digits designated the station number, the letter or letters the type of gage (App A), and the last one or two digits the height above ground. For example, 08F8 was the front differential element of the pitot-static gage at Station F-208, which was mounted 8 feet above ground.

UNCLASSIFIED

19

FORMERLY RESTRICTED DATA

Handle As [REDACTED]

[REDACTED]

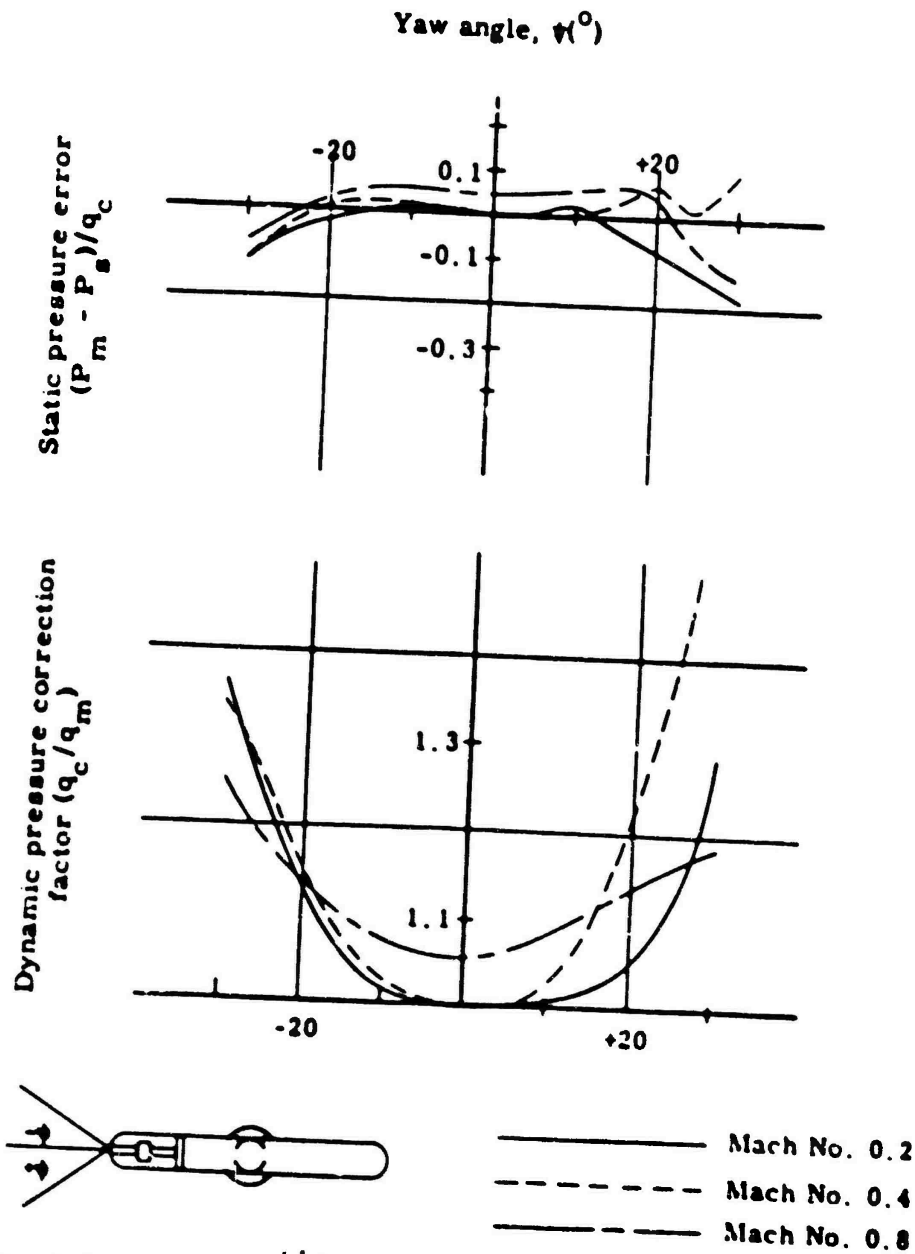


Fig. 1.3 -- Wind-Tunnel Calibration -- Pitot-Static Gage, Yaw Angle

UNCLASSIFIED

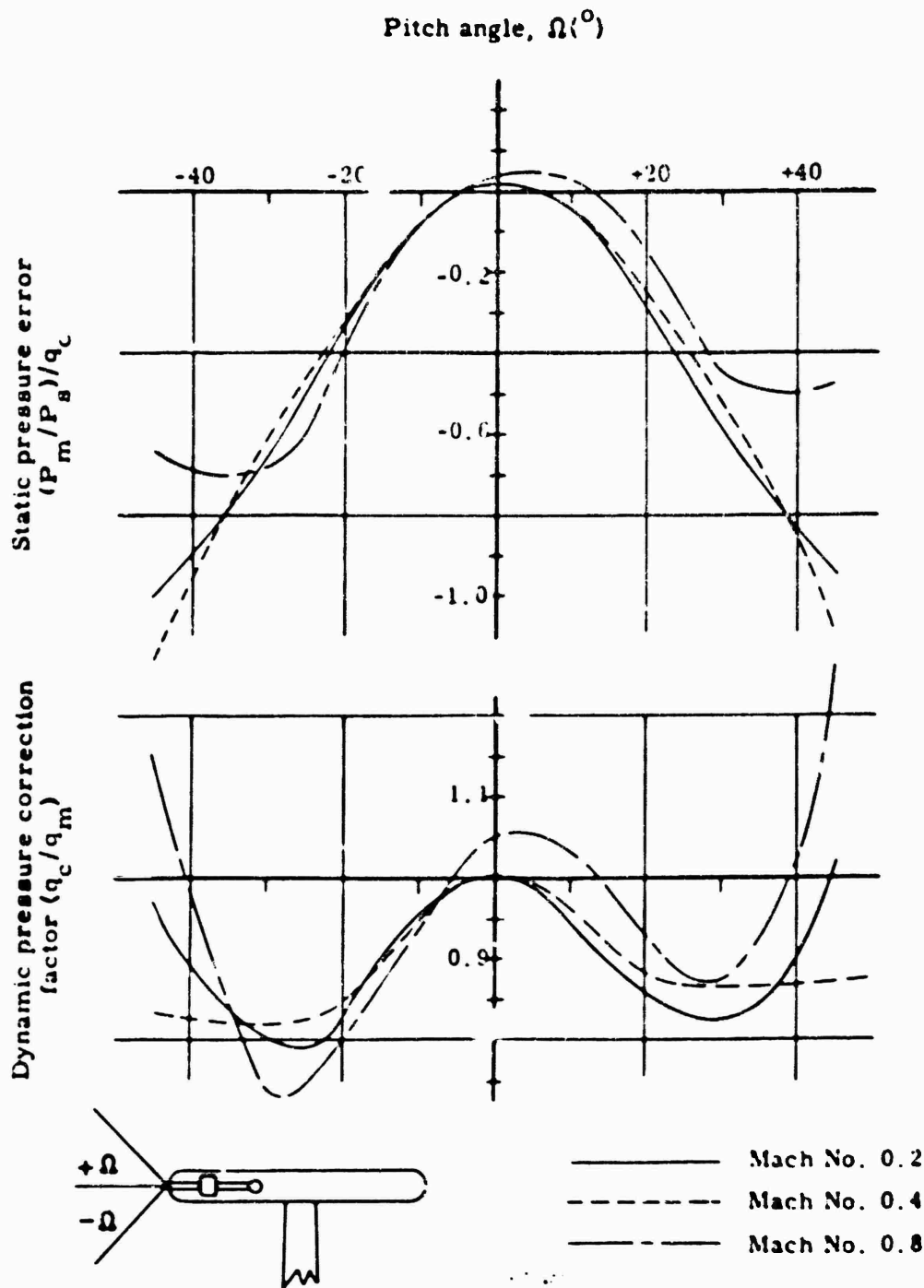


Fig. 1.4 -- Wind-Tunnel Calibration -- Pitot-Static Probe, Pitch Angle

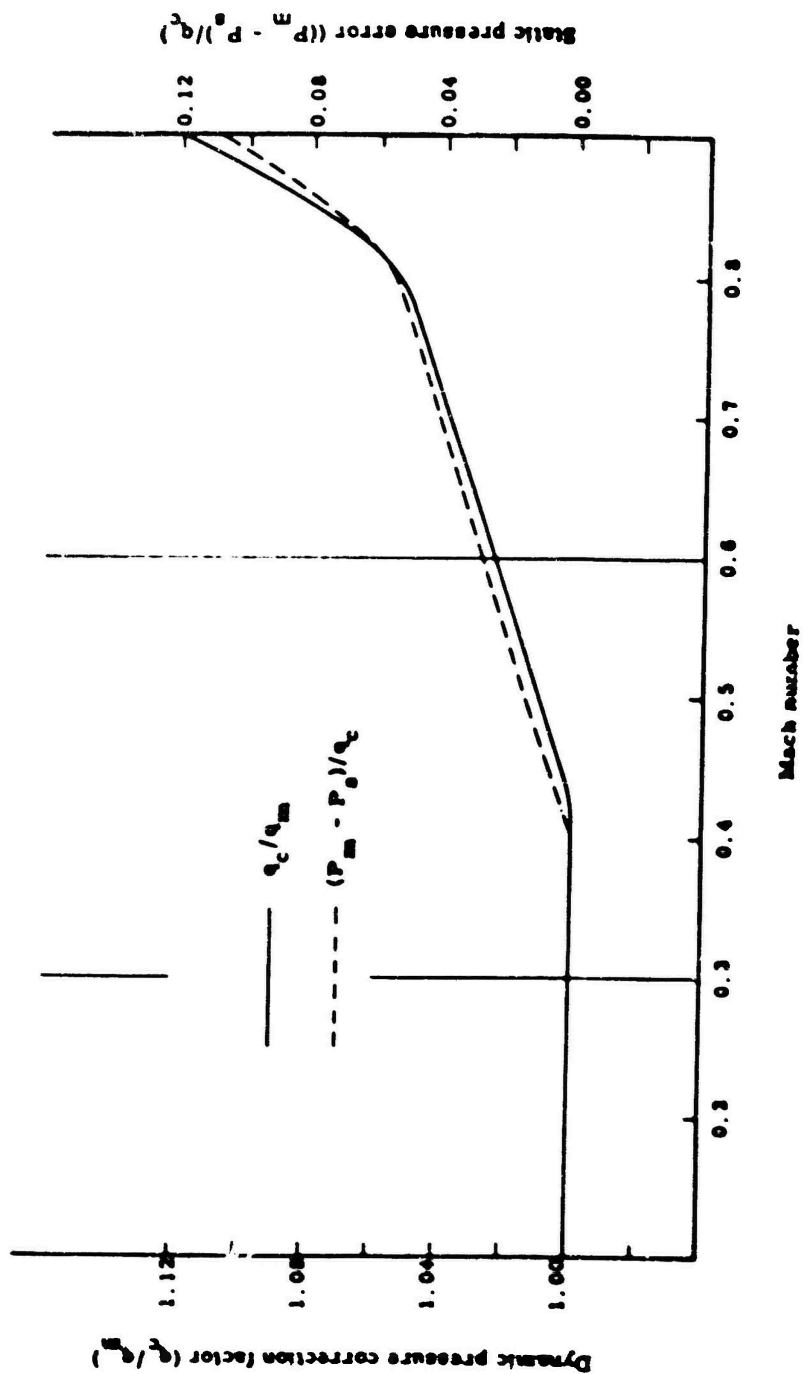


Fig. 1.5 -- Wind-Tunnel Calibration -- Pitot-Static Gage, Mach Number

FORMERLY CLASSIFIED DATA UNCLASSIFIED

#### 1.4.2 Shot 1

Shot 1 was a tower burst (300 ft) of a 16.2-KT weapon. Since in this series of measurements there was particular interest in measuring dynamic pressures at higher overpressure levels than on previous operations, pitot-static gages were installed at predicted overpressure levels of 40 and 25 psi (Stations 3-264 and 3-285)(Fig. 1.6) to determine the maximum overpressures that could be withstood by the instrument. Resulting data could, of course, be compared with those obtained from later measurements on Shots 9 and 10.



Fig. 1.6 -- Pitot-Static Gage Mounted on 10-Ft Tower at Station 3-264 on Shot 1

A tower accelerometer was mounted at Station 3-284 to measure radial acceleration of the tower at the predicted overpressure level of 40 psi.

**UNCLASSIFIED**

~~FORMERLY RESTRICTED DATA~~

A third pitot-static gage was installed at the 10-psi overpressure level (Station 3-289) on this shot so that data recorded by it could be correlated with those from a group of experimental gages being evaluated under another phase of this project (Ch 3).

#### 1.4.3 Shot 9

Shot 9 was an airburst having an intended yield of 30 KT and a height of burst (2420 ft) scaled from that for TUMBLER Shot 1. Since no precursor was expected to form, it was anticipated that measurements made on this shot would serve as an experimental check on Eqs 1.1 and 1.3 under the conditions of ideal shock waves.

The layout of the blast line is illustrated in Fig. 1.7, and pertinent details of the instrumentation are presented in Tables 1.3 and 1.4. Except for that at intended ground zero, which was mounted to measure vertical flow (Fig. 1.8), all pitot-static gages were mounted to respond to horizontal flow. At stations along the main blast line the gages were mounted at elevations of 10 feet (Fig. 1.9).

At the request of Project 3.4 (bridge structures) pitot-static gages were also placed at the 25- and 40-ft levels at Station F-200 to provide measurements of dynamic pressure as a function of height above ground. And at the request of Project 3.19 gages were installed at the 10- and 35-ft levels at Station F-285 on the blast line and at corresponding ground range at the 10-, 35-, and 60-ft levels (Station F-286) in the tree stand (Fig. 1.10).

Yawmeters installed on this shot were mounted to measure the vertical component of wind direction in the region of regular reflection to verify the assumption that flow behind the reflected shock wave actually was horizontal. Pertinent details of their positions are given in Table 1.8.

Accelerometers were installed at Station F-280 on the goal post and at Station F-216 on the 50-ft tower to determine whether accelerations were large enough to affect the pressure gages significantly.

#### 1.4.4 Shot 10

The intended yield (15 KT) and height of burst (500 ft) for this shot were such that a precursor was expected to form. Except for several minor changes the gage layout was essentially the same as for Shot 9 (Tables 1.5 and 1.6). Station F-214 at ground zero was removed, and an additional pitot-static gage was mounted at the 40-ft level at Station F-217. Station F-286 in the tree stand was instrumented with a q-tube (Ch 3) for this shot, it being felt by this time that this instrument would be more accurate for recording the low dynamic pressures anticipated here.

Yawmeters for this shot (Table 1.8) were oriented to measure the angle in the horizontal plane between the direction of the shock winds and the blast line to determine whether cross flow in the precursor was significant.

Both the tower accelerometers (Table 1.9) used to measure radial acceleration on Shot 9 were reactivated for Shot 10.

FORMERLY RESTRICTED DATA UNCLASSIFIED

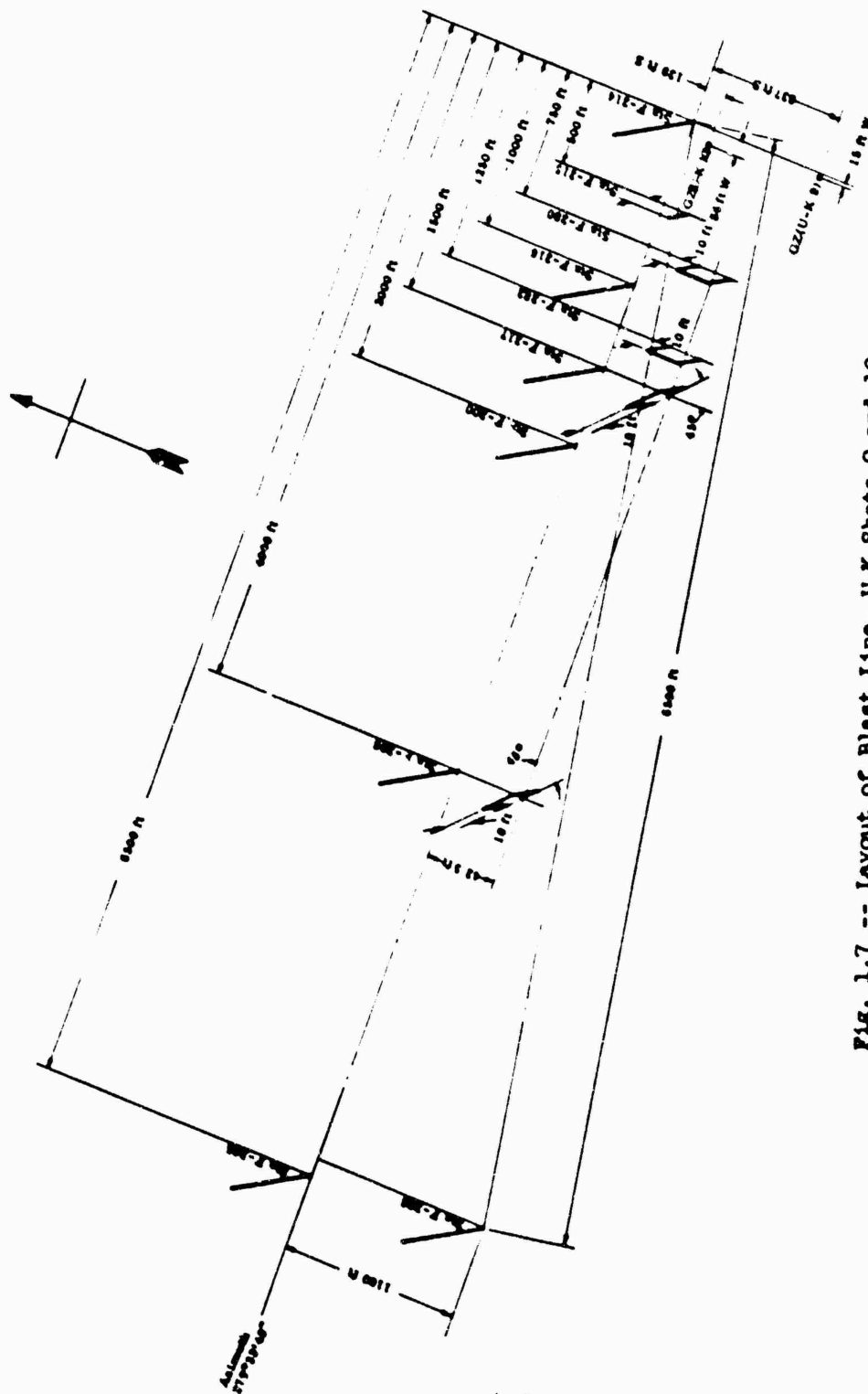


Fig. 1.7 -- Layout of Elast Line, U-K Shots 9 and 10



Fig. 1.8 -- Pitot-Static Gage at Station F-214 (intended ground zero), Mounted to Measure Vertical Flow

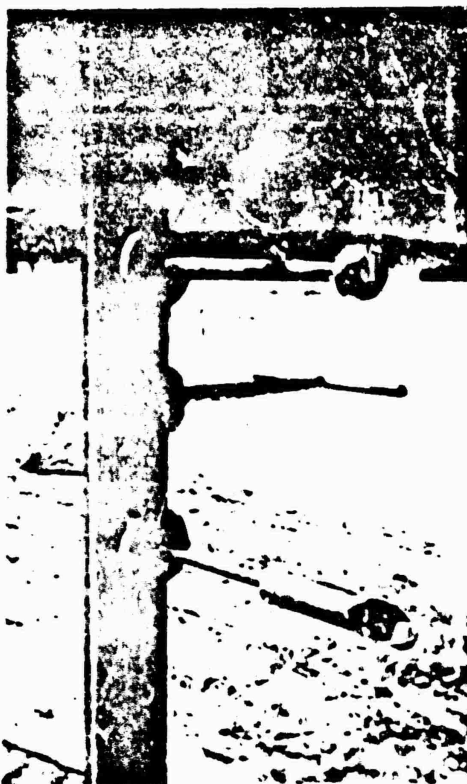


Fig. 1.9 -- Pitot-Static Gage at the 10-ft Level at Station F-280. Also Shown are the Yawmeter (top) and the Resistance Temperature Gage (bottom)

UNCLASSIFIED

~~FORMERLY RESTRICTED DATA~~





Fig. 1.10 -- Preshot View (looking toward intended ground zero) of Pitot-Static Gages at the 10-, 35-, and 60-ft Levels in the Tree Stand for Shot 9

#### 1.4.5 Shot 11

Instrument towers had been blown down in the region where the precursor existed on Shots 1 and 10, apparently because of large dynamic pressures in the precursor region. Hurried plans were therefore made to install a single pitot-static gage on Shot 11. This gage was loaned to the Stanford Research Institute, the instrumenting agency for the blast line, who installed, calibrated, and recorded the information from this gage. Its location and other pertinent details of its installation are presented in Table 1.7.

### 1.5 RESULTS AND DISCUSSION

#### 1.5.1 Presentation of Results

Data from the pitot-static gage are listed in Tables 1.1 and 1.2 for Shot 1, in Tables 1.3 and 1.4 for Shot 9, in Tables 1.5 and 1.6 for Shot 10, and in Table 1.7 for Shot 11. Data from the yawmeters and tower accelerometers are presented in Tables 1.8 and 1.9. The usual

TABLE 1.1 - Dynamic Pressure, Pitot-Static Gage, Shot 1

Sta. No.	Gage No.	Ground range (ft.)	Elev (ft.)	Type wave-form	$t_a$ (sec)	$\Delta t_1$ (sec)	$\Delta t_2$ (sec)	$\Delta t_3$ (sec)	$q_1$ (psi)	$q_2$ (psi)	$q_3$ (psi)	$\Delta t_4$ (sec)	Record duration <sup>a</sup> (sec)
3-284	85710	1250	10	E	0.2154	0.0031	0.0226	0.0286	4.5	62.0	115	-	0.044
3-285	85710	1450	10	E	0.2878	0.004	0.0137	0.0242	3.3	7.2	37	-	0.043
3-289	85713	2600	13	P	1.0704	-	0.013	-	0.55	2.20	-	0.73	-

<sup>a</sup> From arrival of blast wave until cable break.

TABLE 1.2 - Overpressure, Pitot-Static Gage, Shot 1

Sta. No.	Gage No.	Ground range (ft.)	Elev (ft.)	Type wave-form	$t_a$ (sec)	$\Delta t_1$ (sec)	$\Delta t_2$ (sec)	$\Delta t_3$ (sec)	$\Delta p_1$ (psi)	$\Delta p_2$ (psi)	$\Delta p_3$ (psi)	$\Delta t_4$ (sec)	Record duration <sup>a</sup> (sec)
3-285	85610	1450	10	E'	0.2875	0.004	0.0137	0.0242	6.6	9.9	13.0	-	0.043
3-289	85613	2600	13	P'	1.0702	-	0.013	-	3.9	8.1	-	0.730	-

<sup>a</sup> From arrival of blast wave until cable break.

UNCLASSIFIED

UNCLASSIFIED

TABLE 1.3 - Dynamic Pressure, Pitot-Static Gage, Clot 3

Sta No.	Gage No.	Ground range (ft)	Plant range (ft)	Elev (ft)	Type wave-form	t <sub>a</sub> (sec)	t <sub>r</sub> (sec)	q <sub>i</sub> (psi)	q <sub>r</sub> (psi)	Δt <sub>r</sub> (sec)	Δt <sub>i</sub> (sec)	Δt <sub>2</sub> (sec)
P-214	14711	837	2550	11	B	1.0966	1.1100	1.77	a	0.30	0.002	-
	1489	837	2552	9	B	1.0980	1.1087	a	a	0.30	-	-
P-280	80713	1087	2645	13	B	1.1657	1.1815	a	a	0.26	-	-
P-216	16710	1300	2740	10	B	1.2368	1.2480	a	1.53	0.53	0.008	0.012
P-282	82713	1473	2820	13	B	1.3012 <sup>b</sup>	1.3151	0.20	0.90	0.59	0.006	0.016
P-217	17710	1712	2965	10	B	1.4025	1.4090	a	1.40	0.70	0.001	0.011
P-200	00710	2160	3240	10	B	1.6175	1.6197	a	2.20	0.83	0.001	0.012
	00725	2160	3230	25	B	1.6097	1.6250	a	1.45	0.80	0.015	0.019
	00740	2160	3220	40	B	1.6012	1.6352	a	1.32	0.80	0.010	0.022
P-208	0878	4075	4740	8.5	D	2.8246	-	1.50	-	1.00	0.004	-
P-285	85710	6545	6560	10	D	4.7000	-	0.60	-	1.10	0.003	-
	85735	6545	6570	35	D	4.7000	-	0.54	-	1.00	0.005	-
P-286	86710	6460	6500	10	C	4.5902	-	0.47	-	0.91	-	-
	86735	6460	6500	35	D	4.5898	-	0.47	-	0.91	0.007	-
	86760	6460	6500	60	C	4.5804	-	0.37	-	0.91	0.007	-

<sup>a</sup> Records show negative values because of orientation of gage; not interpretable.

<sup>b</sup> Second step at 1.3074 sec shows negative value.

UNCLASSIFIED

TABLE 1.4 - Overpressure, Pitot-Static Gage, Shot 9

Sta No.	Gage No.	Ground range (ft)	Blant range (ft)	Elev (ft)	Type wave-form	$t_a$ (sec)	$t_r$ (sec)	$\Delta P_1$ (psi)	$\Delta P_r$ (psi)	$\Delta t_p$ (sec)	$\Delta t_s$ (sec)	$\Delta t_1$ (sec)	$\Delta t_2$ (sec)
P-214	14911	837	2551	11	A'	1.0965	1.1089	8.3	23.4	0.668	2.89	-	-
P-220	82813	1087	2645	13	B'	1.1662	1.1877	5.7	17.0	0.684	3.30	0.016	0.009
P-216	16810	1300	2740	10	B'	1.2317	1.2480	7.6	15.5	0.716	3.05	0.012	0.007
P-202	82813	1473	2880	13	B'	1.3015 <sup>a</sup>	1.3150	6.2	15.9	0.696	2.95	0.005	0.025
P-217	17810	1712	2965	10	B'	1.4024	1.4080	5.4	13.8	0.736	3.21	0.006	0.007
P-200	00810	2160	3240	10	B'	1.6177	1.6197	4.4	11.4	0.787	2.96	0.002	0.030
	00825	2160	3230	25	B'	1.6098	1.6260	5.3	10.8	0.794	2.96	0.016	0.023
	00840	2160	3280	40	B'	1.6012	1.6356	5.4	10.2	0.783	3.12	0.020	0.026
P-208	00808	4075	4740	8.5	D'	2.8242	-	7.5	-	0.917	3.14	0.008	-
P-205	85410	6545	6480	10	D'	4.700	-	4.50	-	0.963	3.22	0.013	-
	85435	6545	6570	35	C'	4.700	-	4.20	-	1.011	3.16	-	-
P-206	86410	6460	6500	10	D'	4.5907	-	4.30	-	1.101	3.05	0.005	-
	86435	6460	6550	35	D'	4.5903	-	3.62	-	1.104	3.09	0.021	-
	86460	6460	6680	60	D'	4.5885	-	3.90	-	0.972	3.23	0.009	-

<sup>a</sup> Flurst step was 4.8 psi, second step of 6.2 psi at 1.3077 sec.

TABLE 1.5 - Dynamic Pressure, Pitot-Static Gage, Shot 10

Sta. No.	Gage No.	Ground range (ft)	Blast range (ft)	Elev (ft)	Type wave form	$t_a$ (sec)	$\Delta t_1$ (sec)	$\Delta t_2$ (sec)	$\Delta t_3$ (sec)	$\Delta t_4$ (sec)	$q_1$ (psi)	$q_2$ (psi)	$q_3$ (psi)	$q_4$ (psi)	$\Delta t_5$ (psi)	Record duration (sec)
P-202	02713	1169	1277	13	E	0.2675	0.005	0.015	0.030	0.052	1.0	3.7	39	57	-	0.058
P-217	17720	1422	1512	10	E	0.3580	0.008	0.012	0.018	0.044	-0.52	0.52	> 9.6	> 9.6	-	0.140
	17740	1422	1502	40	E	0.3715	0.003	0.051	0.088	0.104	-1.54	1.54	> 11.6	> 11.6	-	0.120
P-200	02720	1980	1988	10	E	0.6060	0.015	0.027	0.144	0.199	0.31	0.51	10.9	10.9	-	0.461
	02725	1980	1984	25	E	0.6155	0.037	0.067	0.114	0.164	0.29	1.15	4.0	11.6	-	0.417
	02740	1980	1980	40	E	0.6255	0.072	0.096	0.224	0.244	1.36	2.30	12.4	12.4	-	0.573
P-208	0270	3918	3952	8.5	D	2.1298	0.080	-	-	-	0.600	-	-	-	0.87	-
P-205	02710	6417	6438	10	D	4.1709	0.080	-	-	-	0.150	-	-	-	1.13	-
	02735	6417	6436	35	C	4.1716	-	-	-	-	0.180	-	-	-	1.03	-

\* From arrival of blast wave until cable break.

TABLE 1.6 - Overpressure, Pitot-Static Gage, Shot 10

Sta. No.	Gage No.	Ground range (ft)	Blast range (ft)	Elev (ft)	Type wave form	$t_a$ (sec)	$\Delta t_1$ (sec)	$\Delta t_2$ (sec)	$\Delta t_3$ (sec)	$\Delta t_4$ (sec)	$\Delta P_1$ (psi)	$\Delta P_2$ (psi)	$\Delta P_3$ (psi)	$\Delta P_4$ (psi)	$\Delta t_5$ (sec)	$\Delta t_6$ (sec)	Record duration (sec)
P-202	02813	1169	1277	13	E	0.2670	0.005	0.015	0.030	0.052	8.6	8.6	27.0	30.0	-	-	0.058
P-217	17810	1422	1512	10	E	0.3580	0.008	0.012	0.018	0.044	8.7	10.1	12.5	26.4	-	-	0.140
	17840	1422	1502	40	E	0.3720	0.003	0.031	0.094	0.114	4.3	12.9	-7.6	12.9	-	-	0.120
P-200	02810	1980	1988	10	E	0.6065	0.015	0.027	0.144	0.199	6.1	6.1	9.4	11.0	-	-	0.461
	02825	1980	1984	25	E	0.6165	0.037	0.067	0.114	0.164	7.9	8.4	8.2	12.1	-	-	0.654
	02840	1980	1980	40	E	0.6260	0.072	0.096	0.224	0.244	8.3	8.1	8.4	8.1	-	-	0.573
P-208	0280	3918	3952	8.5	D	2.1303	0.080	-	-	-	4.10	-	-	-	6.810	3.45	-
P-205	02810	6417	6438	10	D	4.1716	0.080	-	-	-	2.15	-	-	-	0.980	3.35	-
	02835	6417	6436	40	C	4.1721	-	-	-	-	2.02	-	-	-	0.973	3.14	-

\* From arrival of blast wave until cable break.

UNCLASSIFIED

FORMERLY RESTRICTED DATA

UNCLASSIFIED

TABLE 1.7 - Dynamic Pressure and Overpressure, Pitot-Static Gage, Shot 11

	Gage No.	Elev (ft)	Ground range (ft)	Slant range (ft)	$t_a$ (sec)	$\Delta t_2$ (sec)	$\Delta t_+$ (sec)	$\Delta P_1$ (psi)	$\Delta P_2$ (psi)	$q_1$ (psi)	$q_2$ (psi)
7-204	485	5	3437	3685	1.493	0.044	0.970	-	-	3.0 <sup>a</sup>	5.92
	485	5	3437	3685	1.493	0.044	1.6	5.24	11.5	-	-

<sup>a</sup> Taken 0.033 second after  $t_a$ 

TABLE 1.8 - Wind Direction, Yawmeter

Shot No.	Sta No.	Gage No.	Ground range (ft)	Slant range (ft)	Elevation (ft)	$t_a$ (sec)	$t_r$ (sec)	Wind direction
9	P-280	80710	1087	2645	10	1.1673	1.1787	Horizontal after reflected shock
	P-216	16711	1300	2790	11.6	1.2351	1.2477	Horizontal after reflected shock
	P-282	32110	1473	2830	10	1.3023	1.3119	Horizontal after reflected shock
	P-217	17710	1712	2965	10	1.4013	1.4072	Horizontal after reflected shock
10	P-216	16711	926	1059	11.6	0.1979		Small oscillation of wind in horizontal plane about radius from ground zero
	P-282	82710	1169	1277	10	0.2676		until the gages were blown away (20-60 msec)
	P-217	17710	1422	1512	10	0.3569		

UNCLASSIFIED

TABLE 1.9 - Tower Acceleration Measurements

Shot No.	Sta No.	Cage No.	Ground Fringe (ft)	Elev (ft)	Type tower	Direction	$t_a$ (sec)	$\Delta t_a$ (sec)	$A_1$ (g)	$V_1$ (ft/sec)	$D_1$ (in.)
1	3-209	80A10	1250	10	10-ft, 3-1a diameter, 6 guys	Radial	0.2133	0.0461	63	60	8
9	F-280	80A10	1087	10	Goal post	Along blast line	1.1671		+4, -3, +2.5		
10	F-216	16A10	1300	10	50-ft	Along blast line	1.2182				
	F-200	80A10	680	10	Goal post	Along blast line	0.1381	0.0313	82	50	5.9
	F-216	16A10	986	10	50-ft	Along blast line	0.1956	0.0281	60	25	2.5

<sup>a</sup> Time from blast arrival until cable break; when measured it is time at which  $A_1$ ,  $D_1$ , and  $V_1$  are measured.

FORMERLY RESTRICTED DATA

significant information on arrival times, peak pressures, positive and negative phase durations, and details of gage locations is tabulated. All symbols and abbreviations are defined in Appendix A; yields, burst points, and shot conditions are tabulated in Appendix B; and tracings of the records from individual gages are presented in Appendix C.

As might be expected, the type of reflection region in which they are recorded and effects of localized thermal or mechanical interactions imparts certain characteristic features to the overpressure- and dynamic pressure-time waveforms observed at various locations. Some of these characteristic waveforms are illustrated in Fig. 1.11, Types A-F representing dynamic pressure-time waveforms and Types A'-F' the corresponding overpressure-time waveforms. Those observed near the ground when no precursor has formed are typified by A-D and A'-D'. In the region of regular reflection ideal waveforms will be like those of A and A', while B and B' show the effects of localized disturbances upon the initial portions of these same shock waves. Types C-C' and D-D' are exemplary waveforms for the region of Mach reflection under analogous conditions. The two-step rise in the region of regular reflection indicates that the incident and reflected shock waves arrived at the gage at different times; in the region of Mach reflection, of course, only a single wave is recorded so long as the Mach stem is higher than the height of the gage off the ground. Types E and E' are highly stylized representations of waveforms observed in the precursor shock wave; while the rounded fronts and erratic fluctuations behind the front are generally characteristic, they vary considerably in actual measured waveforms. Types F and F', while observed in the precursor shock wave on Shot 1, were actually measured at a ground distance such that the precursor had virtually died out. Although identical in shape to A and A', they are a manifestation of an entirely different phenomenon, as is indicated by the fact that the same type waveform was observed by the ground baffle gages as by the gages above ground.

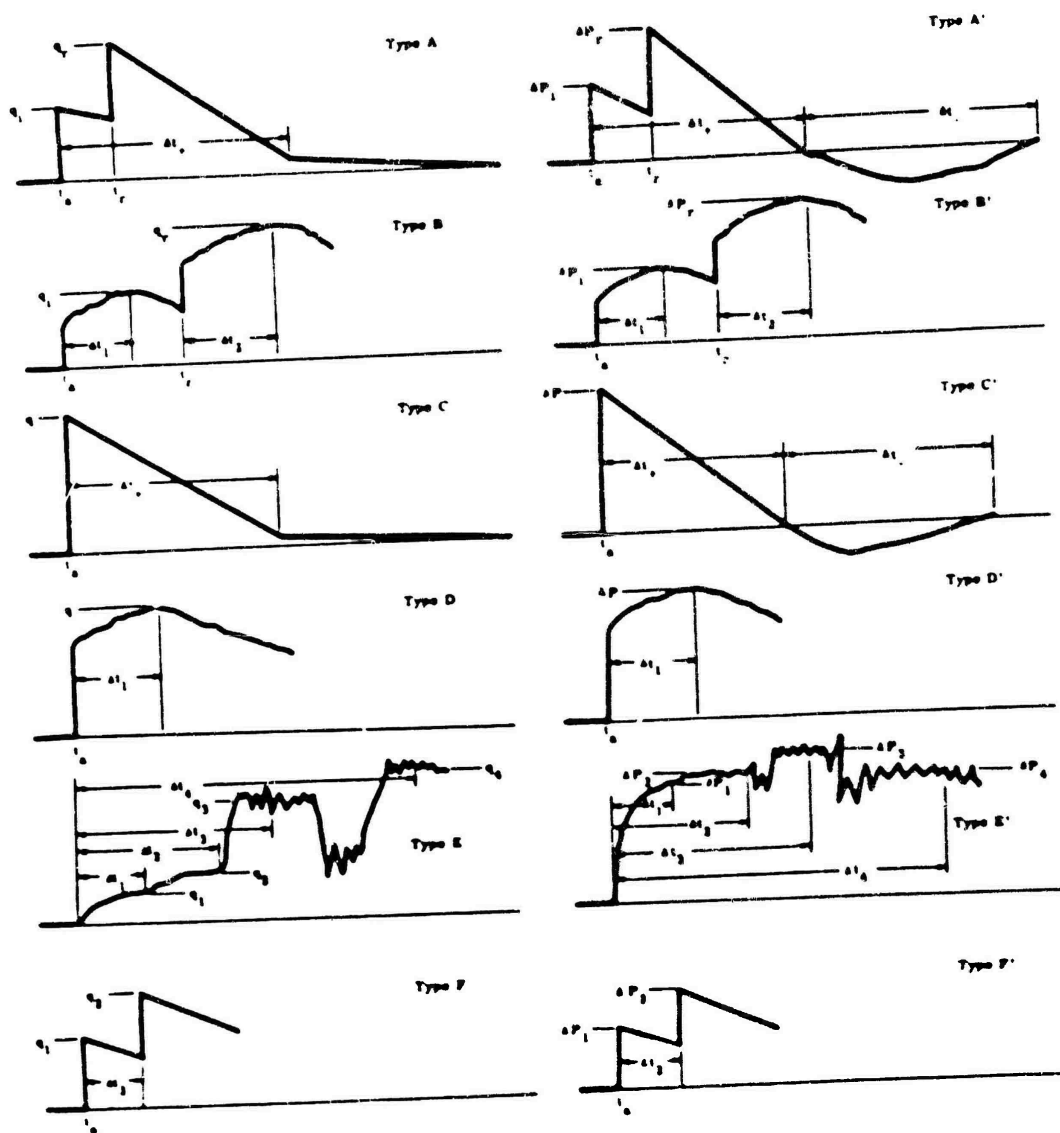
#### 1.5.2 Dynamic Pressures in the Regular and Mach Reflection Regions (No Precursor)

Most of the measurements of dynamic pressure that were unaffected by precursor formation were made on Shot 9; only three were made on Shot 10. Before discussing the significance of these measured values, however, the following observations should be made.

1. It will be noted that in waveforms of Types A and C the record does not decay to zero. Because the front differential gage of the pitot tube is much less sensitive in the negative than in the positive direction, and because maximum dynamic pressures in the negative phase are much smaller than in the positive phase, we would expect any signal from the gage during the negative phase to be so small as to be hardly detectible. To determine why the signals were actually positive, the gage was tested in the laboratory by applying a pressure pulse which decayed to zero in approximately two seconds. These tests revealed short-time "hysteresis" of variable magnitude which was attributed principally to the grease damping used in the Wiancko gage. It is therefore concluded that the end of the positive phase of dynamic

**UNCLASSIFIED**





$AP$  Overpressure  
 $AP_1$  Maximum overpressure of incident wave  
 $AP_2$  Maximum overpressure of reflected wave  
 $AP_3, AP_4$  Overpressures at times  $\Delta t_1, \Delta t_2, \Delta t_3, \Delta t_4$

$\Delta t_1$  Positive phase duration  
 $\Delta t_2$  Negative phase duration  
 $\Delta t_3$  Time interval after arrival of blast wave  
 $\Delta t_4$  Initial arrival time of blast wave  
 $\Delta t_5$  Arrival time of reflected wave

$q_1$  Maximum dynamic pressure, incident wave  
 $q_2$  Maximum dynamic pressure, reflected wave  
 $q_3$  Dynamic pressure measured at  $\Delta t_1, \Delta t_2, \Delta t_3, \Delta t_4$

Fig. 1.11 -- Representative Dynamic Pressure- and Overpressure-Time Waveforms

UNCLASSIFIED

pressure should be taken to be the end of the period of rapid decay as illustrated in the waveforms of Types A and C; and the tabulated durations on Shots 1, 9, and 10 have been read in this fashion.

2. On Shot 9 the yawmeters in the region of regular reflection showed flow to be horizontal after arrival of the reflected wave. Records from the yawmeters at Stations F-280 and F-282 did indicate, however, that flow was apparently not horizontal until 20 and 40 msec after arrival of the reflected shock wave. Subsequent calibration of these two gages revealed that the slow decay of these signals was caused by obstructions in the pressure inlets to the gage. Thus the apparent nonhorizontal flow was not real but the result of a spurious response of the gage.

3. Tower accelerations measured in the regular reflection region on Shot 9 were so small as to have little effect on gage performance.

4. Waveforms for Shot 9 (Figs. C.2 through C.5) give evidence of a general rounding of the shock fronts and irregularities of the waveform during the first few milliseconds after arrival at the gage. This behavior is more pronounced for the reflected wave in the region of regular reflection, but the over-all effect became less pronounced at increasing ground distances with two exceptions. One of these was at Station F-286 in the tree stand and the other at Station F-285 (Fig. C.3b), which had a road intersection in front of it. It is believed that the 6-12-in. layer of fine loose dust in front of the latter station may have contributed to the irregularity of the initial portion of the shock at this station. Because of this general rounding of the shock fronts,  $t^*$  times after arrival at which maximum pressures were recorded are also tabulated.

These observations should be kept in mind in the following comparison of measured dynamic pressures with those calculated from the measured overpressures. In the regular reflection region the horizontal component of  $q$  after reflection is calculated in accordance with Section 1.2.1. Overpressures used for these calculations were obtained by averaging those measured by Projects 1.1a<sup>16,17</sup> and 1.1b<sup>18</sup> with those measured by the pitot-static gage. These measured and calculated values of dynamic pressure as well as fractional deviations of the measured from the calculated values are presented in Table 1.10. The algebraic mean of all deviations is 4.4 per cent, the measured dynamic pressures averaging greater.

In the region of Mach reflection, 7 of the 10 measured values deviated in the positive direction, the mean deviation for this region being +8.4 per cent. With a single exception all records from this region manifested rounded, irregular waveforms. Four of these records were taken at Station F-285, where dust loading was anticipated, and three were taken at Station F-286 in the tree stand. Dynamic pressures measured on previous experimental operations had been found to be in good agreement with those calculated from the measured overpressures (Section 1.2.2), but it should be pointed out, too, that those recorded pressure-time waveforms were Type C waveforms. It would seem probable, then, on the basis of this experimental evidence, that if dynamic pressures are measured in the Mach region under conditions such that the waveforms are rounded by mechanical interaction so that they more

~~FORMERLY RESTRICTED~~  
~~UNCLASSIFIED~~

UNCLASSIFIED

TABLE 1.10 - Comparison of Measured and Calculated Dynamic Pressures  
in the Region of no Precursor

Shot No.	Type of shock	Gage No.	Angle of incidence (°)	$\Delta P$ used for calculation (psi)	Calculated $q$ (psi)	Measured $q$ (psi)	Fractional deviation
9	Incident	14711	-	8.3	1.73 <sup>a</sup>	1.77 <sup>a</sup>	+0.023
	Reflected	16710	28	7.7	1.26	1.53	+0.21
	Reflected	82713	32	6.6	1.21	0.90	-0.26
	Reflected	17710	35	6.2	1.25	1.40	+0.12
	Reflected	00740	42	5.3	1.57	1.32	-0.16
	Reflected	00725	42	5.3	1.57	1.45	-0.076
	Mach	04710	-	11.4	3.17	2.20	-0.31
	Mach	0878	-	8.4	1.76	1.50	-0.14
	Mach	85710	-	4.4	0.48	0.60	+0.25
	Mach	85735	-	4.4	0.48	0.54	+0.12
	Mach	86710	-	4.3	0.46	0.47	+0.02
	Mach	86735	-	4.0	0.42	0.47	+0.12
	Mach	86760	-	3.8	0.38	0.37	-0.026
10	Mach	0878	-	4.4	0.48	0.60	+0.25
	Mach	85710	-	1.99	0.11	0.15	+0.36
	Mach	85735	-	1.88	0.10	0.12	+0.20

<sup>a</sup>  $q$  in the incident shock, normal to the shock front

nearly approach those characterized by Type D, they may be somewhat higher than those calculated from the corresponding measured overpressures. A possible explanation for this observed increase in dynamic pressure may be found in the response of the pitot-static gage to dust-loading of the air (App D). Apparently the gage registers the dynamic pressure of the dust, and as  $(\rho u^2)_{\text{dust}}$  rather than as  $(\frac{1}{2} \rho u^2)_{\text{dust}}$ .

In the region of regular reflection, on the other hand, only two out of five measured dynamic pressures were greater than those calculated, the mean deviation being -3.3 per cent. Again the waveforms exhibited the rounded fronts and irregularities characteristic of thermal and mechanical interaction near the ground. But the deviation is so small that it is probably not significant, and we may assume that other factors in the reflection process acting to reduce the dynamic pressure counteract any tendency toward increased dynamic pressures that results from dust loading. One such factor is the variation of incident overpressure with height above the ground that causes reflected pressures to be less than ideal as based on the incident pressures at 10 feet.

Figure 1.12 is a graphic comparison of measured and calculated dynamic pressures for Shot 9 upon which is superimposed a curve of dynamic pressure derived from Porzel's theoretical dynamic pressure height-of-burst chart (Fig. 1.1). The break in the curve drawn through the dynamic pressures calculated from measured overpressures, which is more or less corroborated by the experimentally measured values, illustrates vividly the importance of gage height above ground in the region where the Mach stem is only a few feet high. For example, at a ground distance of 2160 feet the Mach stem was 9 feet high, and the dynamic pressure measured at the 10-ft level, while lower than that calculated from the overpressure in the Mach stem, was considerably higher than those measured at the 25- and 40-ft levels. The theoretical curve of  $q$  vs distance (Porzel) differs considerably from that for measured or calculated  $q$ 's; these differences might be anticipated, however, since this curve is based upon ideal overpressures and dynamic pressures at ground level so that in it the regions of regular and Mach reflection were joined in a smooth curve. As experimental measurements have shown, actual dynamic pressures in the transition region are quite sensitive to the height above ground at which measurements are taken.

### 1.5.3 Dynamic Pressures in the Precursor Region

Before discussing the significance of the experimentally measured dynamic pressures in the precursor region we wish to emphasize existing uncertainties to which these data are subject:

1. On Shots 1 and 10 the set ranges of the gages in the precursor region were much smaller than the signals received; consequently the response of the recording system was nonlinear. For the Consolidated system used, the galvanometer deflection is asymptotic to approximately twice the deflection used for set range, reaching this saturation value for an input about four times that corresponding to the set range. Calibrations of the recording system subsequent to the operation were used to correct for this nonlinearity. Thus the dynamic pressures listed are the minimum values consistent with these calibrations.

UNCLASSIFIED

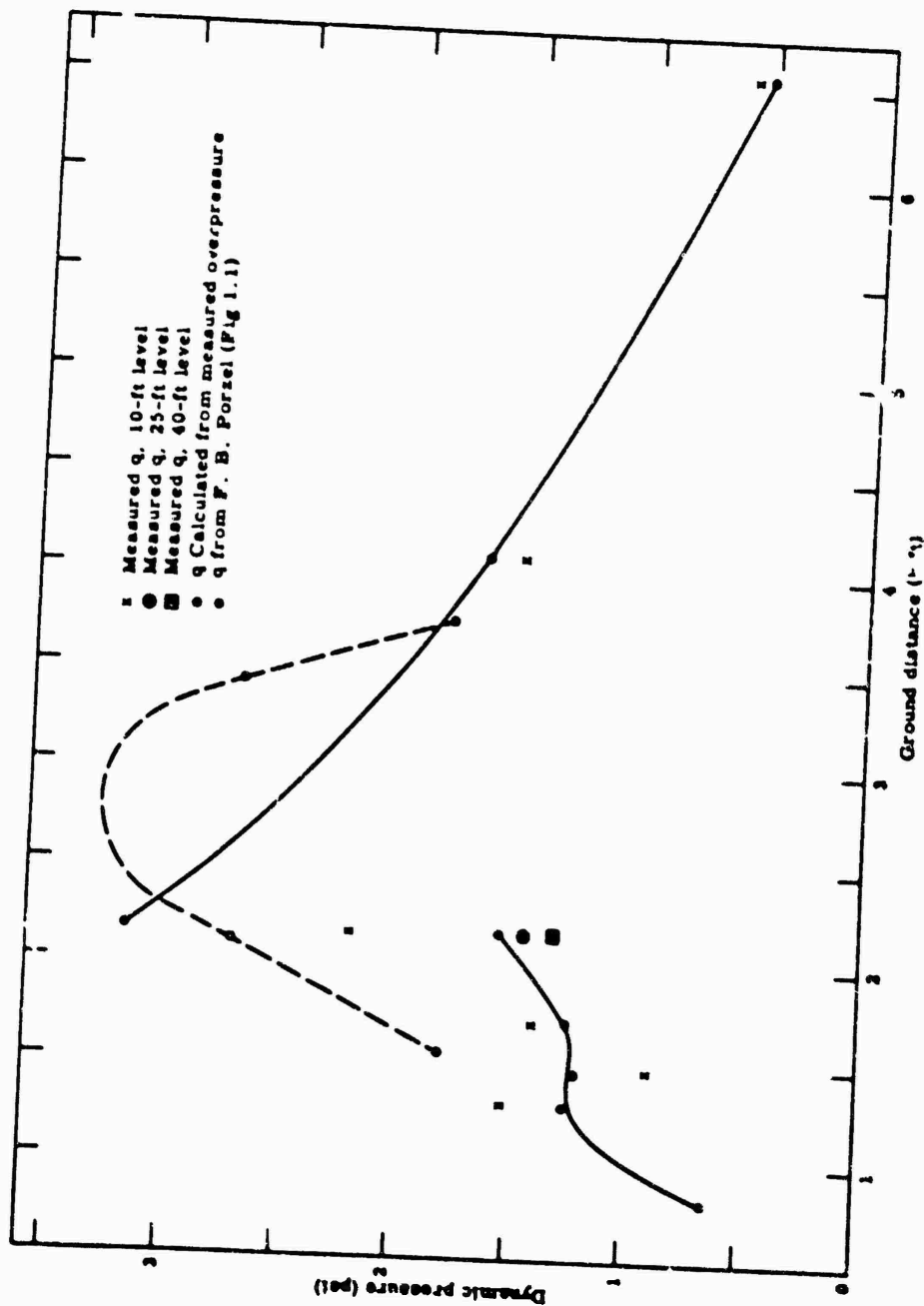


Fig. 1.12 -- Comparison of Measured and Calculated Dynamic Pressures on Shot 9

UNCLASSIFIED

CONFIDENTIAL DATA

However, records from three gages, 82F13, 17F10, and 17F40 (Fig. C.4), used on Shot 10 indicated that either the gages or the recording system were completely saturated; therefore the values of dynamic pressure for these gages (Table 1.5) have been presented simply as greater than the saturation values obtained from the calibration records.

2. The records were also corrected in accordance with the calibration curves presented as Figs. 1.3 and 1.4 by assuming that the angle between wind direction and the appropriate axis of the gage was that obtained from the geometry of the actual burst point and that flow was horizontal. Values of  $q$  were further corrected from  $q_c = \frac{1}{2} \rho u^2 (1 + 0.25 M^2 + 0.025 M^4 + \dots)$  to  $q = \frac{1}{2} \rho u^2$  by assuming the Mach number to be that obtained from the overpressure, using the Rankine-Hugoniot relation. Both corrections did not exceed a total of 15 per cent in the value of  $q$  in any instance.

Motion pictures of the precursor on Shot 10 show that initially the direction of flow was upward at an angle of  $40^\circ - 60^\circ$  and probably became horizontal sometime after the dust front had passed. The dust reached only a definite height and the particles at the front moved horizontally as they reached this maximum height. Therefore the initial values of dynamic pressure (as represented by  $q_1$  and  $q_2$  of waveform Type E, Fig. 1.11) should be corrected for this angle. An exact correction can not be made since the direction of flow is not known accurately; however, it is believed that such a correction could not more than double the measured initial pressures ( $q_1$  and  $q_2$  in Tables 1.1 and 1.5). Even if these initial pressures were doubled, they would still be less than the values measured later ( $q_3$  and  $q_4$  in these same tables), which were measured after the dust front behind the precursor shock wave had arrived at the gage, at which time flow was probably horizontal.

3. With the exception of the gage at Station 3-289 on Shot 1, which was at the very end of the precursor, all instrument towers and gages in the precursor on Shots 1 and 10 were destroyed during passage of the shock wave. Postshot photographs of the gage from Station 3-285 on Shot 1 (Fig. 1.13) and Station F-200 on Shot 10 (Fig. 1.14) illustrate the complete destruction that took place. Comparison of the dynamic pressure records from these gages with overpressure records from the same locations and from corresponding ground-baffle gages indicates that the gages probably operated long enough to record maximum pressures actually obtained in the blast wave. This conclusion cannot, of course, be stated as an absolute certainty.

Since the towers and gages were blown away, the question arises as to what effect acceleration or changing orientation may have had on the output of the gage. Previous tests<sup>19</sup> of the Wiancko transducer indicated that its acceleration sensitivity would be less than 1 per cent of set range at accelerations of the order of 50 g, as were observed on Shot 1 (Table 1.9). Double integration of the record from this accelerometer (which was mounted on the same tower as the pitot-static gage nearest ground zero) indicates a displacement of only 6 inches when the record from the pitot-static gage failed. On Shot 10 accelerometers were mounted at the 10-ft level at Stations F-280 and F-216, both of which were nearer ground zero than Station F-282, where the

~~FORMERLY RESTRICTED DATA~~ UNCLASSIFIED

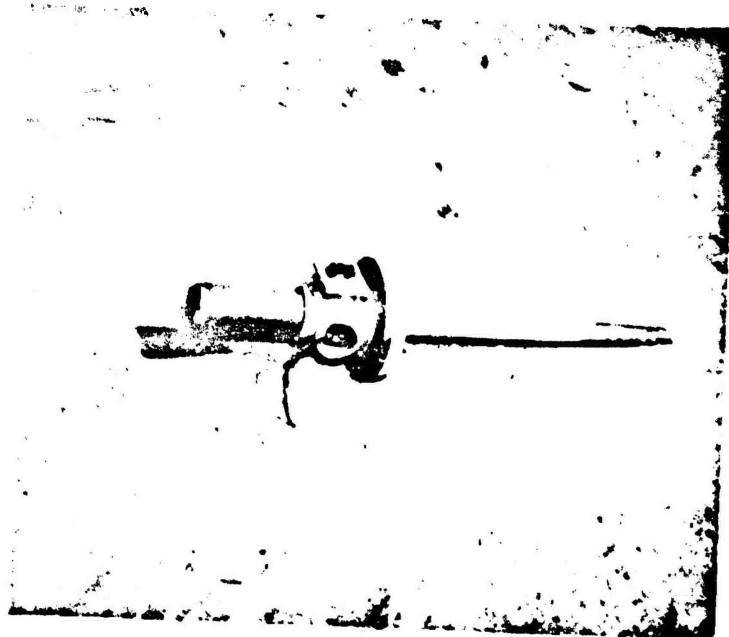


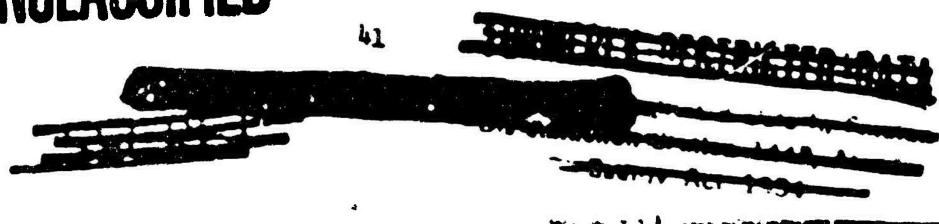
Fig. 1.13 -- Remains of Pitot-Static Gage from Station 3-285, Shot 1



Fig. 1.14 -- Post-Shot View of Station F-200, Shot 10

**UNCLASSIFIED**

41



closest pitot-static gage was installed. At the time these accelerometers failed the indicated displacements were only 6 inches and 3 inches, respectively. Therefore the dynamic pressure records from gages that were destroyed were probably not seriously affected by either acceleration or orientation.

4. For convenience the differential pressures measured by the pitot-static gages in the precursor region have been labeled  $q$  (dynamic pressure) in the tables and figures. However, since  $q$  has been defined as  $\frac{1}{2}\rho u^2$  only for a gas, and since these measurements were made in the presence of considerable quantities of suspended dust, this label is misleading.

In this new experiment dust loaded into the shock wave caused the shock front to become rounded at the point of loading, but the front shocked up again as it traveled down the tube. A major result of these shock-tube tests is evidence that the Wiancko gage registers the dynamic pressure of dust particles, at least those 1-100 microns in diameter, as  $\frac{1}{2}\rho_d u_d^2$ , where  $u_d$  is the velocity of the dust particles and  $\rho_d$  is dust density (ie, the mass of dust per unit volume, not the density of the individual dust particles). This coefficient of one should depend somewhat upon dust density, particle size, and gage construction; however, this dependence appears to be fairly weak.

Let us now examine the dynamic pressures measured in the precursor on Shots 1, 10, and 11 in the light of these observations. The waveforms (Figs. C.1, C.6, and C.7) show initial low dynamic pressures, which, even if corrected for angle of incidence, are considerably lower than those recorded after arrival of the dust front behind the precursor shock wave; the same phenomenon was observed in the shock tube. The corresponding overpressure records have rounded rises, the rounding being less pronounced at greater heights above ground. This rounding can be attributed to dust loading and to rapid expansion of the precursor front near the ground; that there is a rapid expansion can be deduced from photographs showing that the inclined front is straight to within about five feet of the ground.

Table 1.11 is a comparison of the maximum  $q$ 's measured in the precursor with those calculated from the overpressure as measured simultaneously by the pitot-static gage. On Shot 1 at the two closer stations where the precursor was strongest the measured  $q$ 's were approximately 20 and 10 times those calculated; but at the farthest station, which was near the point where the precursor was dying out, measured and calculated  $q$ 's were in good agreement. On Shot 10 the measured  $q$ 's were about 3-4 times those calculated except for one value 7.5 times as great. On Shot 11 the maximum measured  $q$  was about twice that calculated, and that in the initial step was 4 times that calculated.

Appendix E presents arguments indicating that measured  $q$ 's in the dust-laden shocks of the strengths encountered here would not be expected to be more than 3-4 times those calculated from the overpressures and suggests possible explanations for the few extremely high measured  $q$ 's.

In Fig. 1.15 the  $q$ 's measured in the precursor are compared graphically with idealized curves derived from Porsel's dynamic

UNCLASSIFIED



TABLE 1.11 - Comparison of Measured and Calculated Dynamic Pressures in Precursor Region

Shot No.	Gage No.	Ground Range (ft)	$\Delta P$ (psi)	q (calculated) (psi)	q (measured) (psi)	$\frac{q_{meas}}{q_{calcd}}$
1	84F10	2600	2.00	5.4	115	21
	85F10	2600	1.50	4.1	40	9.8
	89F13	2600	4.4	0.52	0.55	1.06
			9.7	2.38	2.20	0.925
10	82F13	1169	30.0	18.4	> 57	3.1
	17F10	1422	26.4	15.1	> 9.6	> 0.64
	17F40	1422	12.9	4.0	> 11.6	> 2.9
	00F10	1920	11.0	2.95	10.9	3.7
	00F25	1920	12.1	3.55	11.6	3.3
	00F40	1920	8.1	1.65	12.4	7.5
11	4F5	3435	5.24	0.74	3.0	4.0
			11.5	3.3	5.92	1.8

pressure height-of-burst chart (Fig. 1.1). The single measurement on Shot 11 and that at a ground range of 2600 feet on Shot 1 are in good agreement with the theoretical curves. The two values for a ground range of 1422 feet on Shot 10 were measured under conditions such that the gage and/or recording system were completely saturated, and although the measured values are apparently low, we know that the actual values were somewhat higher. Other experimentally measured q's all appear to be considerably higher than the theoretical values, however. Consequently, although it appeared initially that dynamic pressures measured in the precursor were approximated by the ideal curves,<sup>20</sup> at present the over-all agreement between measured and ideal dynamic pressures does not seem as good. In the light of present knowledge that the gages register dust as  $\rho u^2$  rather than  $\rho_0 u^2$  it would seem that any agreement between measured and ideal values is mere coincidence. On the basis of the discussion in Appendix E it is believed that dynamic pressures measured are influenced primarily by relative air and dust densities and by need of energy to the material behind the precursor front from higher-pressure regions above the precursor.

#### 1.5.4 Dynamic Pressures in Secondary Shocks

While this information about secondary shocks is not of primary importance to this study, it is felt that it adds to the completeness of the discussion of data from this series of measurements.

In the overpressure records from Shot 9 a compression wave pulse is seen to move from the end toward the beginning of the negative phase as the shock wave progresses. This pulse appears as a positive

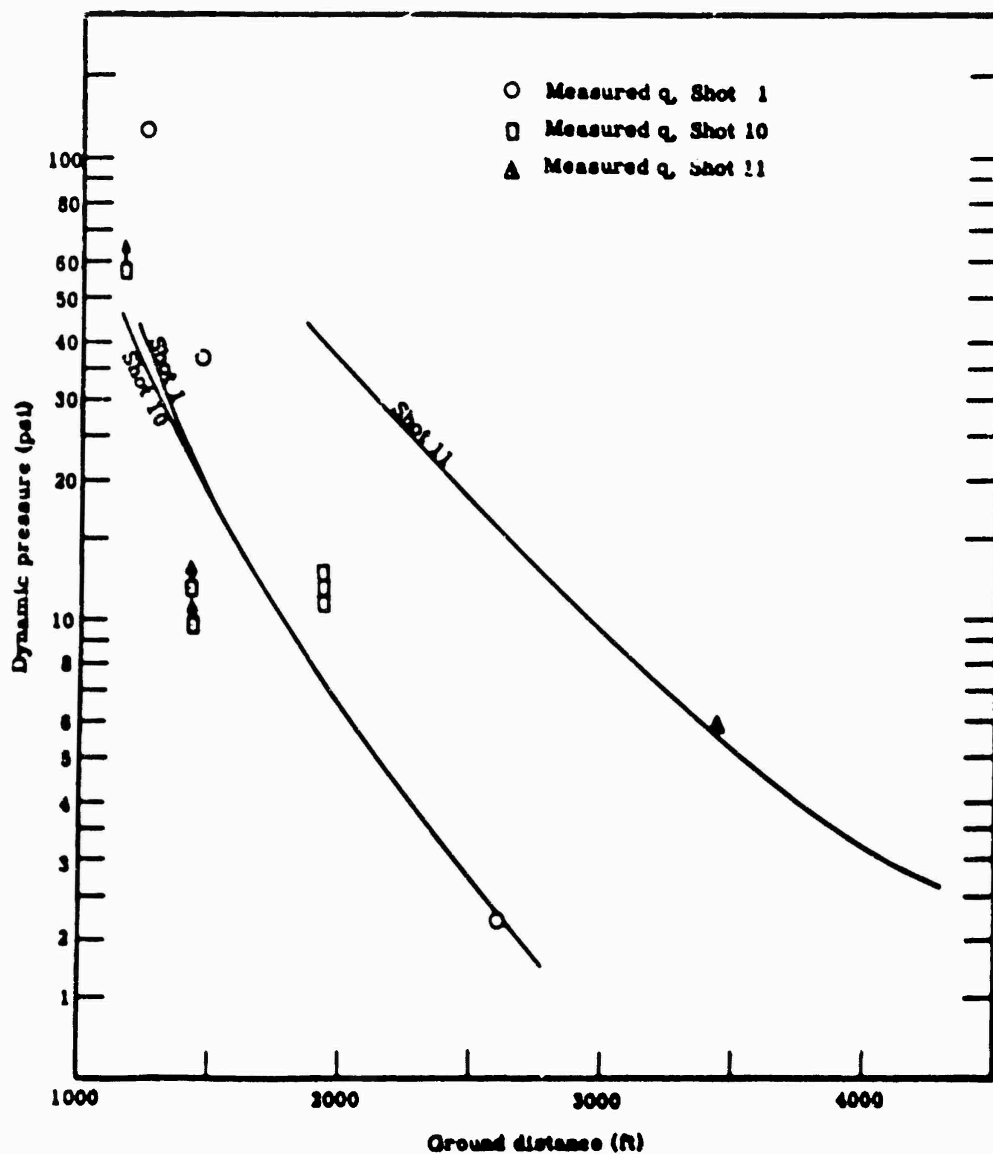


Fig. 1.15 -- Comparison of Dynamic Pressures Measured in the Precursor with Dynamic Pressure-Distance Curves from Porsel (Fig. 1.1)

UNCLASSIFIED

signal in the dynamic pressure records, indicating that the winds actually reversed their direction and blew in the direction away from ground zero during this pulse.

Overpressure records from Stations F-286 and F-285 on Shot 9 give evidence of a secondary shock near the end of the negative phase that does not appear in the dynamic pressure records; there is a similar situation in the records from Stations F-208 and F-285 on Shot 10. Apparently in these instances there was no reversal of wind direction.

## 1.6 CONCLUSIONS AND RECOMMENDATIONS

Experimental evidence from this series of measurements on UPSHOT-KNOTHOLE indicates that when a precursor has not formed, measured dynamic pressures are in reasonable agreement with those calculated from the measured overpressures. When the shock front is disturbed and there is some dust in the shock wave, measured dynamic pressures in the region of Mach reflection are, on the average, about 8 per cent higher than those calculated from the overpressure; in the region of regular reflection dynamic pressures measured under the same conditions did not differ significantly from those calculated. These deviations are not to be interpreted as correction factors, however, but merely as indications of the small extent to which measured dynamic pressures may differ from those calculated. Thus it would seem that when there is no precursor dynamic pressures are sufficiently well known for most practical purposes.

Laboratory tests have indicated that the pitot-static gage registers dust in the shock wave as approximately  $\log u_d^2$ . Differential pressures measured in the precursor region are therefore believed to represent the dynamic pressure of the air plus the 'dynamic pressure' of the dust. The ratios of measured 'dynamic pressures' to those calculated from the overpressures in the usual fashion vary from 2 to 20. The exact value of this ratio for any particular condition will depend upon the amount of dust being carried along by the shock wave and upon the amount of energy fed into the material behind the shock front.

A structure exposed to a blast wave will be affected by any suspended dust, and measurements of dynamic pressure should include the contribution of the dust as well as that of the air. The pitot-static gage measures the particular combination

$$q = q_{\text{air}} + q_{\text{dust}} = \frac{1}{2} \rho_a u_a^2 + \rho_d u_d^2$$

On the other hand, the drag force per unit frontal area on a structure will probably be a different combination expressed as

$$F/A = C_D q_a + C'_D q_d$$

**UNCLASSIFIED**

In general drag coefficients for air,  $C_D$ , may vary from 0.4 to 2.0 for different structural shapes, whereas that for dust,  $C'_D$ , for reasons cited in Appendix D, is expected to be approximately 1 for small obstacles. Dynamic pressures measured in the field under conditions of dust loading are certainly greater than could be explained on the basis of the dynamic pressure of air alone, and there is a need for measurements that will distinguish between the contributions of air and dust.

It is recommended that intensive laboratory studies be made of the effect of dust loading on shock waves to determine

1. The accelerations and velocities of dust particles of various sizes as a function of time after entry into the shock wave in the absence of obstacles to the flow.
2. How dust interacts with obstacles, both gages and structures.
3. The progress of shock waves through dust-laden air.
4. Any alteration of these shock waves by dust.
5. How dust is picked up from the ground by passing shock waves.

Measurements of overpressure and dynamic pressure at locations above the ground are needed on future full-scale tests on which precursors are anticipated to provide experimental data not subject to the uncertainties of the results reported here. Every effort should be made to obtain measurements throughout the entire passage of the blast wave. Supplementary measurements of air density and temperature as well as dust density and velocity are needed to permit better understanding of the complicated interactions in the precursor and thus permit more reliable prediction of damage from nuclear explosions producing precursors.

**UNCLASSIFIED**

## CHAPTER 2

### PRESHOCK PRESSURE MEASUREMENTS

#### 2.1 OBJECTIVE

This phase of Project 1.1d was initiated specifically to determine experimentally whether there was any observable increase in air overpressure prior to arrival of the main shock wave. Measurements were taken at two elevations above ground.

#### 2.2 BACKGROUND AND THEORY

Previous measurements<sup>9,22/</sup> have demonstrated unquestionably the occurrence of one type of preshock pressure increase -- the precursor shock wave -- under given conditions. Formation of the precursor is ascribed<sup>8,9,10/</sup> to heating of the air near the ground surface by thermal radiation from the fireball. The precursor shock wave, which obtains its energy from the main shock wave, actually precedes the main shock wave, traveling at an increased velocity through the heated layer of air.

But the question has arisen whether the sudden thermal heating of the air can in itself produce a rise in pressure; such an effect would depend essentially upon whether the incident thermal radiation were delivered considerably more rapidly than the heated air could expand. It seemed likely too, that experimental investigation of such a pressure increase might provide information that would aid in interpreting the precursor phenomenon.

#### 2.3 INSTRUMENTATION

Instrumentation for the preshock pressure measurements consisted of Wiancko air pressure gages in side-on baffles, mounted at the 2- and 10-ft levels. On Shot 9, Station F-214 at intended ground zero and Station F-215 at an intended ground range of 500 feet were instrumented. Only the gages at Station F-215 were used on Shot 10.

#### 2.4 RESULTS AND DISCUSSION

##### 2.4.1 Shot 9

Pressure-time records from the various gages used are presented

as Fig. 2.1, and the resultant data are summarized in Table 2.1. On Shot 9 all gages indicated a preshock pressure increase that reached its maximum 0.1-0.2 second after zero time but decreased to zero before arrival of the main shock wave. At Station F-214 these rises were fairly rapid and the peaks well defined, occurring 2.5 msec earlier at the 2-ft level than at the 10-ft level. Over-all pressure increases were approximately equal, being about 0.45 psi. At Station F-215 the pressure increase occurred later and in the form of a broad, rounded pulse; arrival times at the 2- and 10-ft gages were virtually simultaneous, but the over-all pressure increase at the 10-ft level was only about half that at the 2-ft level. Recorded overpressures may, because of their small magnitudes, be in error by  $\pm 30$  per cent.

Arrival times of the main shock wave at the 2- and 10-ft levels would indicate that it was not 'toed out' at either station on Shot 9.

It should be pointed out here that the Wiancko canisters were thermally insulated from their mounts and were side-on to intended ground zero. However, because the drop missed ground zero on Shot 9, the baffles at Station F-214 were facing away from the burst and the baffles at Station F-215 were facing obliquely (at an angle of  $19^\circ$  between the thermal rays and the faces) into the burst. Thus it seems unlikely that the gages at Station F-214 were subject to radiation heating, but those at F-215 may have been heated somewhat. Evidence that these pressure rises were not the result of electrical disturbances is the fact that no signals were recorded by either the static or differential pressure elements of the pitot-static gage at Station F-214. Neither element would be expected to observe this preshock pressure signal, but both should be sensitive to electrical disturbances. The static pressure element would not be sensitive enough to see the early signal, and the differential element would not respond to any pressure change affecting both component gages simultaneously.

#### 2.4.2 Shot 10

A monotonic increase in air pressure from zero time until arrival of the first shock wave was observed in the records from the two gages at Station F-215 on Shot 10 (Fig. 2.1). Again the pressure at the 2-ft level was higher than at the 10-ft level. An analysis of the records from all other air pressure gages used by this project on Shots 1 and 9 revealed that any inherent drift of the pressure-time traces from zero time until shock arrival was randomly distributed positive and negative. Moreover, the magnitude of any such drift (all were less than 0.2 psi) is considerably less than the pressures of 3.5 and 2.9 psi recorded on Shot 10. Other gages used on Shot 10 to measure overpressure also indicated preshock pressure increases, the magnitudes of which decreased with increasing distance from ground zero (0.5-1 psi at 1000-1200 feet as compared with 0.1-0.2 psi at 2000 feet). From this evidence it must be concluded that the preshock increase in air pressure observed at Station F-215 on this shot was real and that it decreased in magnitude with increasing height above ground and with distance from ground zero.

~~FORMERLY SECRET~~  
**UNCLASSIFIED**

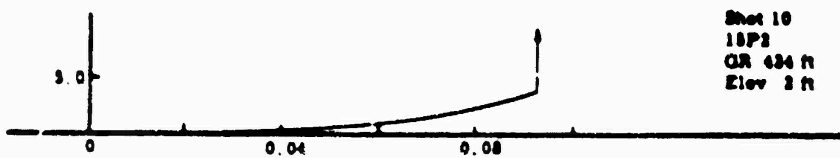
~~Handle As Restricted Data~~  
**SECRET**

UNCLASSIFIED

TABLE 2.1 - Presrock Pressure Measurements

Shot	Sta No.	Gage No.	Elev (ft)	Ground range (ft)	Slant range (ft)	$t_a$ (sec)	$t_r$ (sec)	$\Delta P_1$ (psi)	Presrock pressure increase (psi)	Time of maximum pressure (sec)
9	F-214	14P2	2	840	2560	1.1003	1.1037	9.09	0.42	0.1007
		14P10	10	840	2533	1.0976	1.1080	6.50	0.45	0.1032
9	F-215	15P2	2	956	2602	1.1305	1.1357	8.75	0.23	0.160
		15P10	10	956	2597	1.1297	1.1421	9.00	0.13	0.160
10	F-215	15P2	2	424	674	0.0922	0.0922	59.6	3.5	0.0922
		15P10	10	424	666	0.0950	0.0950	56.0	2.9	0.0950

Preshock pressure (psi)



Time (sec)

UNCLASSIFIED

Preshock Pressure-Time Waveforms from Shots 9 and 10



The first shock wave to arrive at Station F-215 had overpressures of 69.6 psi at the 2-ft level and 56.0 psi at the 10-ft level. It arrived at the 2-ft level 2.8 msec before it arrived at the 10-ft level. Thus it is apparent that this shock was 'toed out' at this station and that the precursor had formed closer to ground zero than this ground range of 424 feet.

## 2.5 CONCLUSIONS AND RECOMMENDATIONS

These measurements have shown that for certain heights of burst and yields, thermal radiation alone may cause preshock increases in air pressure in a limited region. However, additional measurements of this type on future full-scale tests of nuclear weapons are not justified as it would appear that adequate measurements of preshock signals can be made using pressure instrumentation designed for other purposes.

**UNCLASSIFIED**

## CHAPTER 3

### GAGE EVALUATION AND SUPPORTING AIR BLAST MEASUREMENTS

#### 3.1 SCOPE AND DESIGN OF THE EXPERIMENT

Field evaluation tests of four new or improved gages were conducted on UPSHOT-KNOTHOLE to determine their suitability for use on full-scale tests of nuclear weapons. In addition to dynamic and static pressures these gages were designed to measure air density, temperatures prior to and during passage of the shock wave, sonic velocity, and wind or particle velocity. Direct measurement of these variables is desirable, particularly for nonideal shock waves, to permit more accurate assessment of blast effects and a better understanding of the interrelation of the phenomena involved. As a result, blast effects to be expected under varying conditions should be more accurately predictable.

Prototypes of two newly developed gages, the centripetal density gage and the whistle temperature gage, and of modified versions of two previously used gages, the q-tube and the sonic wind and sound speed indicator (SWASSI), comprised the group to be field-tested. Groupings of these instruments were installed at appropriate locations on Shots 1, 9, and 10 in conjunction with installations of pitot-static and resistance temperature gages so that measured dynamic pressures and temperatures could be used to evaluate the performance of the experimental gages. Figure 3.1 shows the group of gages installed at Station 3-289 on Shot 1.

Pitot-static gage measurements of dynamic pressure have already been discussed in Ch 1. Data from the resistance temperature gage are presented in Table 3.1 and tracings of the temperature-time waveforms in Fig. 3.2. In the three instances in which valid temperature measurements were obtained there was excellent agreement between measured temperatures and those calculated from corresponding measured overpressures. This agreement must be taken into account in evaluating data from the experimental gages.

#### 3.2 CENTRIPETAL DENSITY GAGE

##### 3.2.1 Background

Air density is a significant parameter in evaluating the effects of nonideal shock waves like those produced from atomic explosions

UNCLASSIFIED

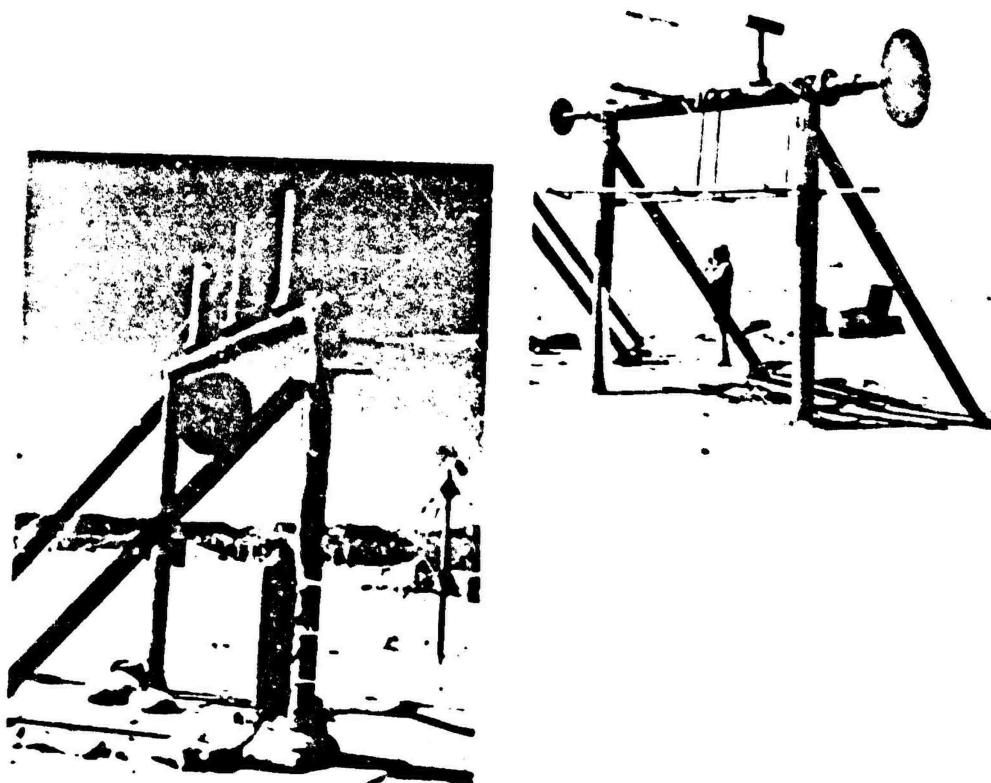


Fig. 3.1 -- Views of Experimental Gages Installed in Field. Top Photograph Shows, Left to Right, Wiancko Air Pressure Gage in Side-on Baffle, Pitot-Static Gage, Resistance Temperature Gage, q-Tube, and Density Gage. Lower Photograph Shows a Density Gage, SWASSI, and Resistance Temperature Gage Installed at Another Location.

over land surfaces. Thus it was felt that experimental data on air densities within such shock waves should be generally applicable to evaluating shock wave theory as well as specifically applicable to evaluating data on measured dynamic pressures.

Direct measurements of density have been made on previous experimental nuclear bursts<sup>22</sup> using a beta densitometer. However, this instrument measured total density of matter, both air and dust. It was hoped that the centripetal density gage developed by Sandia Corporation would measure a quantity more nearly approximating true air density, exclusive of dust.

UNCLASSIFIED

UNCLASSIFIED

TABLE 3.1 - Shock Temperatures, Resistance Temperature Gauge

Shot No.	Sta No.	Gage No.	Ground range (ft.)	$t_a$ (sec)	$t_r$ (sec)	$\Delta t_1$ (sec)	$\Delta T_1$ ( $^{\circ}\text{C}$ )	$\Delta T_1$ (calcd)	$\Delta T_2$ ( $^{\circ}\text{C}$ )	$\Delta T_2$ (calcd)	$\Delta t_+$ (sec)	$\Delta t_-$ (sec)
1	3-289	89TR10	2600	1.0694	-	0.0129	25	27	46	43	a	a
Temperature element bad before shot time												
9	F-216	16TR10	1500	1.3908	1.3908	-	16	-	67	64	a	a
	F-217	17TR10	1633	1.3908	1.3908	-	16	-	67	64	a	a
	F-208	08TR10	4000	1.3908	1.3908	-	16	-	67	64	a	a
Temperature element bad before shot time												
10	F-217	17TR10	1422	0.356	-	-	-	-	-	-	-	-
	F-208	08TR10	3916	2.1246	-	-	24	23	-	-	0.83	-
Amplifier bad												

a Instrument destroyed during blast

b Not readable

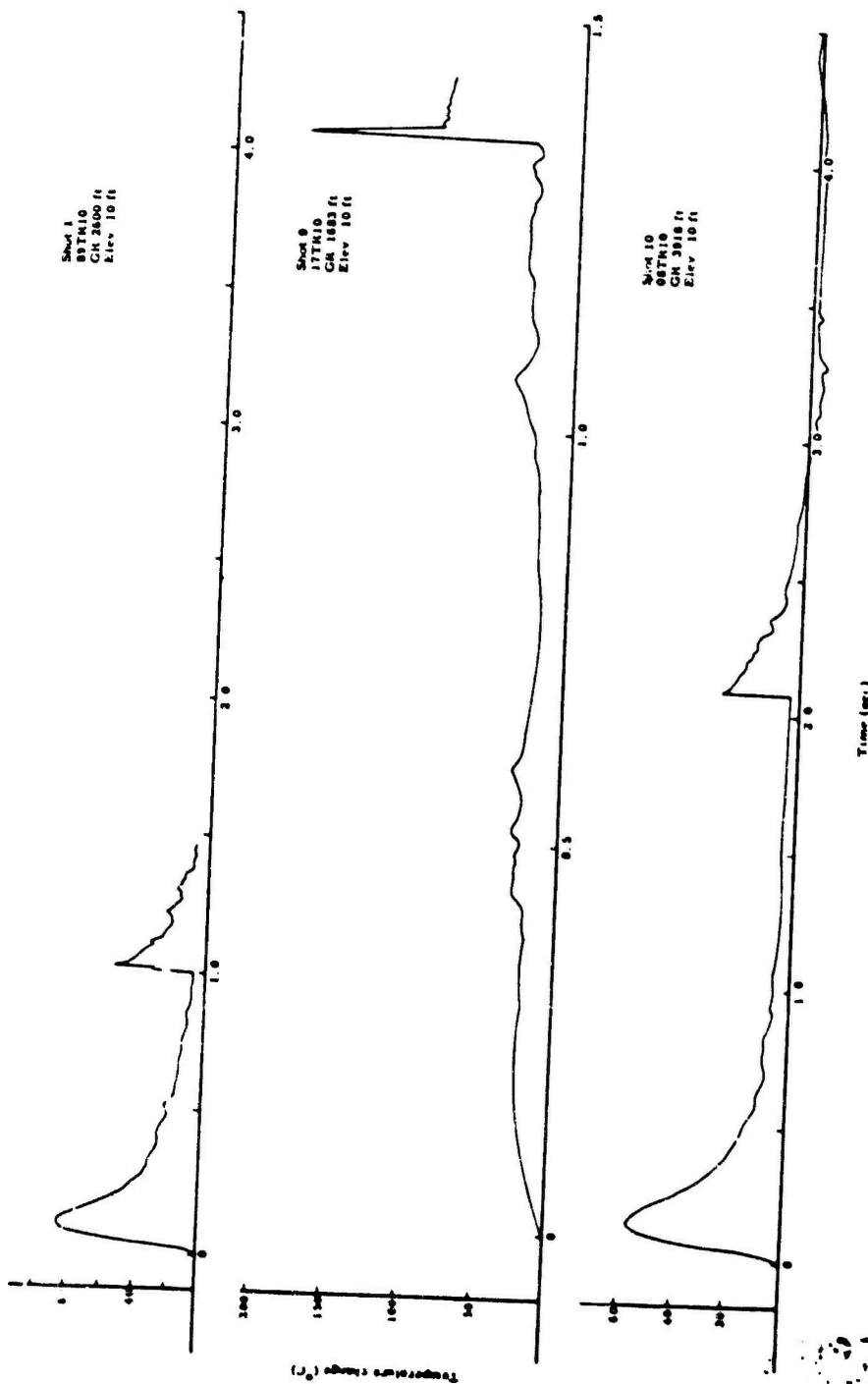


Fig. 3.2 -- Temperature-Time Waveforms, Resistance Temperature Gage

UNCLASSIFIED

55

~~SECRET~~

Exempt Act 1054

### 3.2.2 Instrumentation

The centripetal density gage<sup>23/</sup> (Fig. 3.3) was designed to take continuous measurements of air density from zero time throughout passage of the shock wave. A rotating air column is produced in the gage by a set of blades mounted radially on a disc after the fashion of blades in a conventional centrifugal air blower. At the circumference of this disc are two pressure pickup tubes, one facing in the direction of rotation, the other in the opposite direction. These pressure pickups provide a reading of differential pressure, which is proportional to the dynamic pressure imparted to the air by the rotor; but since the speed of rotation is constant, the differential pressure is also proportional to the density.

To obtain equal fill times for the two pressure openings and ensure essential freedom from hysteresis, a diaphragm-type differential pressure transducer (Fig. 3.4) was designed for use with the density gage. Movement of the diaphragm unbalances an inductive bridge circuit.

For use in the field the entire gage assembly was mounted in a side-on baffle 36 inches in diameter (Fig. 3.5). A static pressure gage incorporating the same type of transducer element was also mounted in the side-on baffle, immediately below the density gage.

Static tests of the density gage in a variable-density and -temperature chamber and in the wind tunnel<sup>23/</sup> indicated that measured differential pressures were directly proportional to density and were essentially insensitive to Mach number of the air flow past the baffle and to the angle of incidence of the wind with the baffle for angles less than  $10^\circ$ .

In field use the gage and recording system were checked for linearity of response by applying known pressure differences to the differential transducer element. A record of the galvanometer deflection corresponding to the air density at calibration is obtained. This density is calculated from measured ambient temperatures and pressures. Together these measurements provide a calibration curve of galvanometer deflection vs air density.

A single density gage was installed at Station 3-289 on Shot 1 of UPSHOT-KNOTHOLE, and on each of Shots 9 and 10 gages were installed at Stations F-217 and F-208.

### 3.2.3 Results and Discussion

Measured density ratios ( $\rho/\rho_0$ ) have been compared with those calculated from the overpressures (Table 3.2); overpressures used for calculation were averages of those obtained by Projects 1.1b<sup>18/</sup> and 1.1c<sup>24/</sup>. Overpressures measured by the static element of the density gage are listed in Table 3.3. Note the excellent agreement between measured and calculated density ratios except for that from gage 17D10 on Shot 10. This gage was the only one in the precursor, the measured density ratio being considerably greater than that calculated. Unfortunately the record ceased prior to arrival of the heavy dust front behind the precursor front. The relation presented by Porzel<sup>19/</sup> (see

**UNCLASSIFIED**

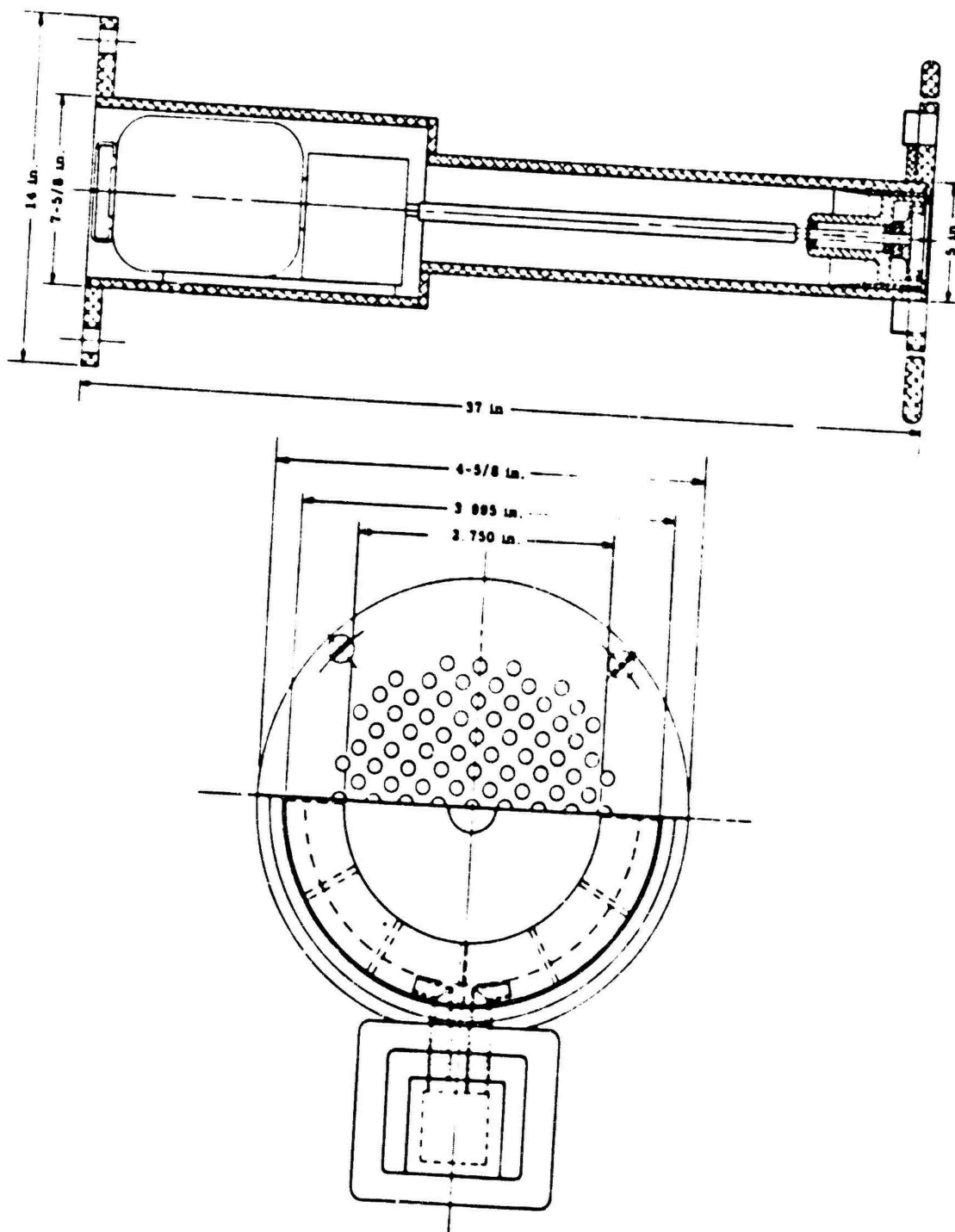


Fig. 3.3 — Detail Drawing, Centripetal Density Gage

UNCLASSIFIED 57

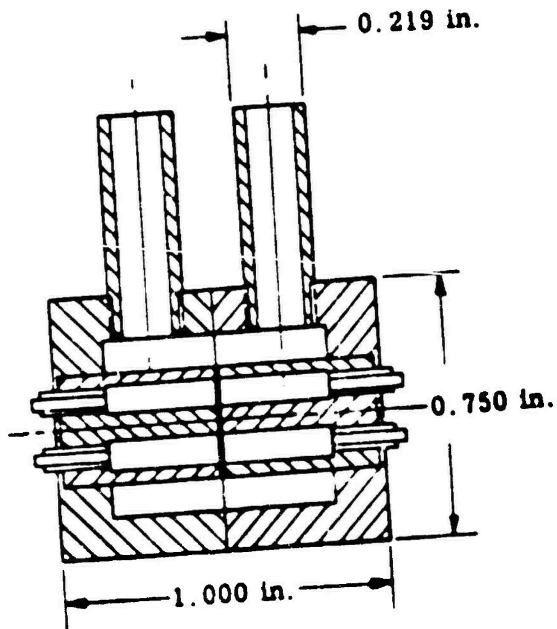


Fig. 3.4 -- Diaphragm-Type Differential Pressure Transducer

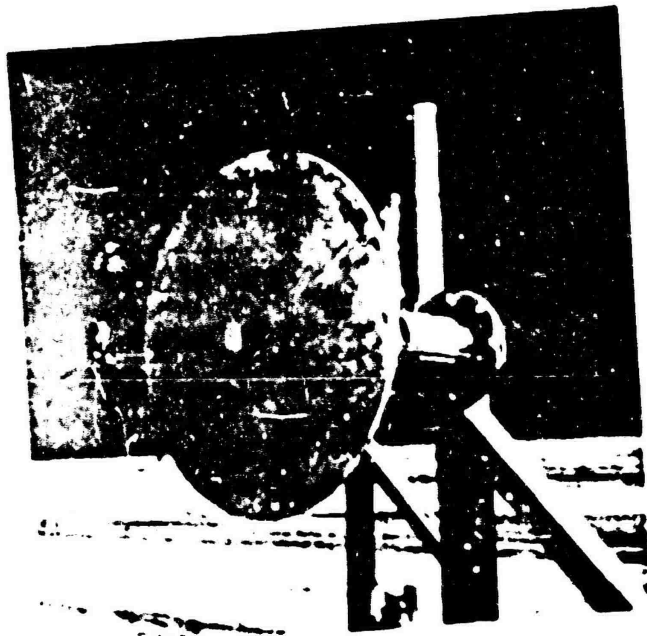


Fig. 3.5 -- Density and Static Pressure Cages in Side-on Baffle in Field

CLASSIFIED



UNCLASSIFIED

TABLE 3.2 - Density, Centripetal Density Gage

Shot No.	Sta No.	Gage No.	Ground range (ft)	$t_a$ (sec)	$t_r$ (sec)	$\Delta t_1$ (sec)	$\rho_1/\rho_0$ (meas)	$\rho_1/\rho_0$ (calcd)	$\rho_2/\rho_0$ (meas)	$\rho_2/\rho_0$ (calcd)	$\Delta t_+$ (sec)	$\Delta t_-$ (sec)
1	3-289	5A010	2000	1.0708	-	0.0100	1.25	1.23	1.50	1.50	0.73	a
9	P-217 P-208	17D19	1939	1.3939	1.4034	-	1.29	1.28	1.75	1.75	0.59	a
		50010	4005	2.3239	-	-	1.47	1.40	-	-	0.61	3.17
10	P-217 P-208	17D10	1422	0.3334	-	-	1.95 <sup>b</sup>	1.55	-	-	c	c
		50010	5913	2.1324	-	-	1.25	1.23	-	-	0.67	a

a Not reliable;  $\rho_0 = 0.99$  before time zero; <sup>b</sup> Tower destroyed during blast

TABLE 3.3 - Overpressure, Centripetal Density Gage

Shot No.	Sta No.	Gage No.	Ground range (ft)	Slant range (ft)	$t_a$ (sec)	$t_r$ (sec)	$\Delta t_2$ (sec)	$\Delta P_1$ (psi)	$\Delta P_2$ (psi)	$\Delta t_+$ (sec)	$\Delta t_-$ (sec)
1	3-289	5A010	2000	2000	1.706	-	0.0140	4.0	10.0	0.712	2.90
9	P-217 P-208	17D10	1939	2903	1.3934	1.4034	-	4.5	13.9	0.619	3.49
		50010	4005	4732	No record		-	-	-	-	-
10	P-217 P-208	17D10	1422	1415	0.3334	-	-	15.7	-	-	a
		50010	5913	5903	2.1341	-	-	4.7	-	0.71	3.40

a Instrument destroyed during blast

also App E) for a shock wave moving through uniformly dust-laden air would account for a higher air density ratio. However, in this instance the shock wave was loaded with dust at the ground, and the shock front reached the gage before the dust front; therefore quantitative comparison is not justified, and no conclusion can be drawn about this apparently high density ratio. There is still some question whether the gage would register any dust component. The record from this same gage indicated that upon arrival of the precursor shock wave the density had decreased to 0.8 its value at zero time; the magnitude of this decrease before arrival of the main shock wave is in agreement with the measured temperature increase at this station<sup>25</sup>; the pressure gage showed an increase in ambient pressure of not more than 1.2 per cent (0.15 psi).

Density-time and overpressure-time waveforms for the gages at Stations F-217 and F-208 on Shots 9 and 10 are presented in Fig. 3.6. The record from gage 17D10 on Shot 10 exhibits oscillations characteristic of the gage operated at its present rotor speed. Waveforms for the other records have been derived by drawing curves through the averages of these oscillations. Since the frequency of these oscillations increases with increasing rotor speed, they may be eliminated entirely by operation at high rotor speeds and installing an electrical filter. Such modification should not affect density measurements in the frequency range of interest.

### 3.2.4 Conclusions and Recommendations

Except in the extremely dusty atmosphere of the precursor this gage has proved eminently satisfactory for use in field measurements of air density under the conditions of full-scale nuclear tests, as demonstrated by the excellent agreement between measured and calculated density ratios.

Redesign to reduce the size and weight of the gage would facilitate handling in the field, and in redesign the rotor speed should be increased to eliminate troublesome oscillation. Both these recommendations are being acted upon.

### 3.3 q-TUBE

#### 3.3.1 Background

In its original form the q-tube<sup>11</sup> was subject to inherent mechanical defects in the operation of the strain gage elements used to measure deflection of the sensing element by wind drag forces. Development of the differential pressure transducer for use in the centripetal density gage (Section 3.2.2) led to an improved modification of the original q-tube which would, it was hoped, prove feasible as an alternate to the pitot-static gage for measuring dynamic pressure under field conditions on full-scale tests, particularly at lower overpressure levels.

**UNCLASSIFIED**

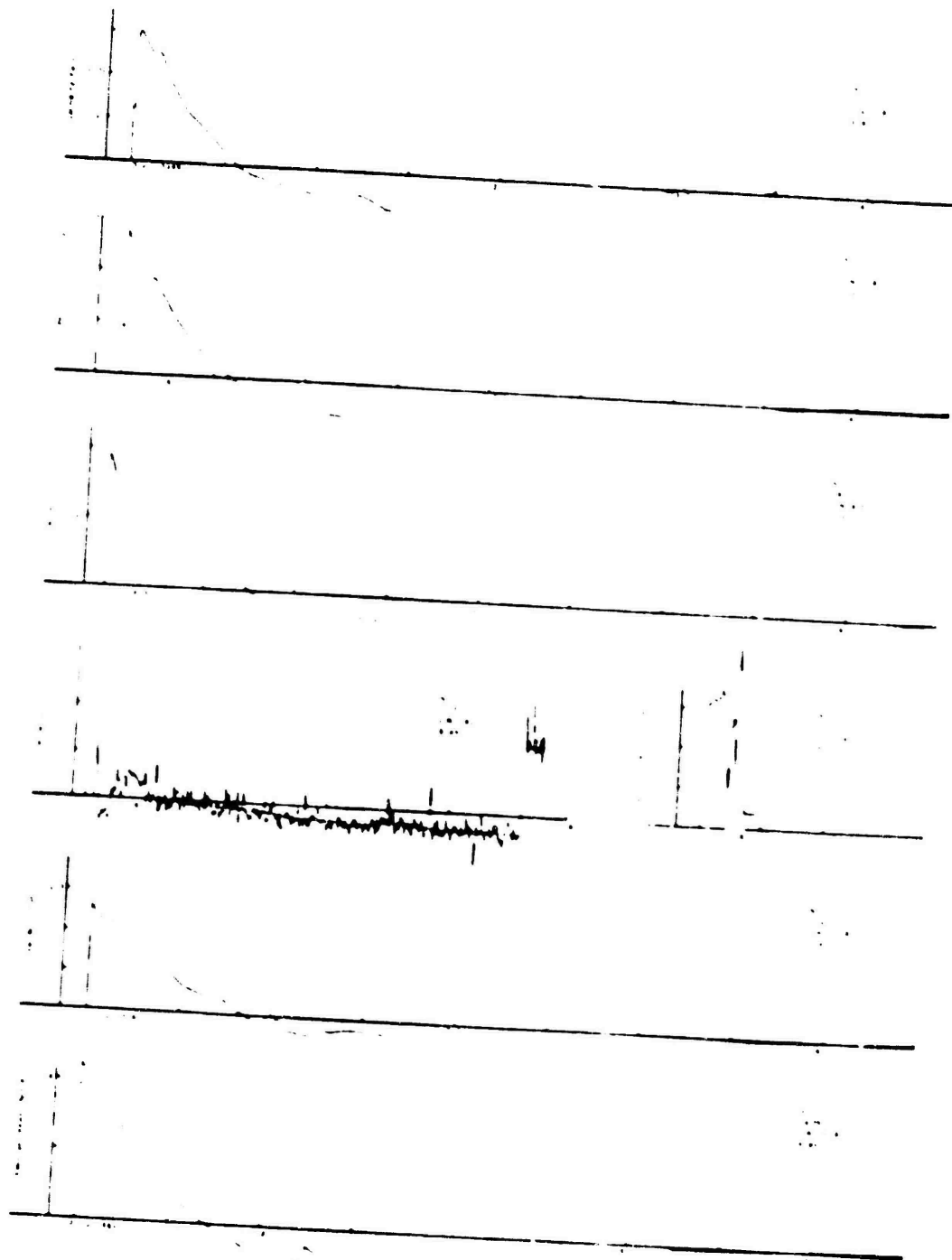


Fig. 3.6 -- Density-Time and Overpressure-Time Waveforms from Centripetal Density Gage

**UNCLASSIFIED**

51

~~CONFIDENTIAL~~

~~CONFIDENTIAL~~

~~CONFIDENTIAL~~

~~CONFIDENTIAL~~

### 3.3.2 Instrumentation

Except for replacement of the strain gages by differential pressure pickups, the q-tube and its mount are essentially the same as described in an evaluation report on its field performance during TUMBLER-SNAPPER.<sup>11</sup> Details of the modified sensing element are illustrated in Fig. 3.7; differential pressure pickups at the front and back of the deflecting disc are connected to the differential pressure transducer as shown. Theoretically the front opening should see total pressure and the back opening a pressure that is less than free-stream static pressure by some fraction of dynamic pressure. Thus the differential pressure as recorded by this instrument should exceed the dynamic pressure by a factor between 1 and 2. Wind-tunnel tests of the gage have shown this factor to be 1.49 for Mach numbers of less than 0.6;<sup>29</sup> hence the sensitivity of this gage is somewhat greater than that of an instrument that measures the difference between static and stagnation pressures, as does the pitot-static gage.

Because the time available for fabrication of test prototypes of the modified gage was relatively short, it was planned to install but a single gage on each shot. These were placed in regions such that ideal shock waves having overpressures of 10 psi or less were anticipated. As discussed in Ch 1, a second gage was installed at Station F-286 on Shot 10 to measure dynamic pressures in the tree stand. Field installation of the q-tube is shown in Fig. 3.1.

### 3.3.3 Results and Discussion

Peak dynamic pressures measured by the q-tube are listed in Table 3.4, while tracings of the corresponding pressure-time curves are presented as Fig. 3.8. Table 3.5 compares measured dynamic pressures with those calculated from the overpressures at the same locations.

The record from the q-tube at Station 3-269 indicated that the gage failed approximately 24 seconds after zero time, and a post-shot survey of this station revealed that the instrument could have been knocked from its mount by flying debris (Fig. 3.9).

This gage was near the outer limit of the precursor and exhibited the two-step waveform seen by all other gages at this station. The peak dynamic pressure in the initial short-duration step as measured by this gage was considerably higher than that calculated and that measured by the pitot-static gage. But the peak dynamic pressure measured in the second step, which is attributed to the main shock wave, is in excellent agreement with that calculated as well as that measured by the pitot-static gage.

On Shot 9 the peak dynamic pressure measured by gage 08q11 at Station F-208 deviated by less than 3 per cent from that calculated. Although on Shot 10 the same gage recorded a dynamic pressure 35 per cent greater than calculated, the measured dynamic pressure was within 6 per cent of that measured by the pitot-static gage at the same location.

While the gage at Station F-286 in the tree stand measured a peak

UNCLASSIFIED

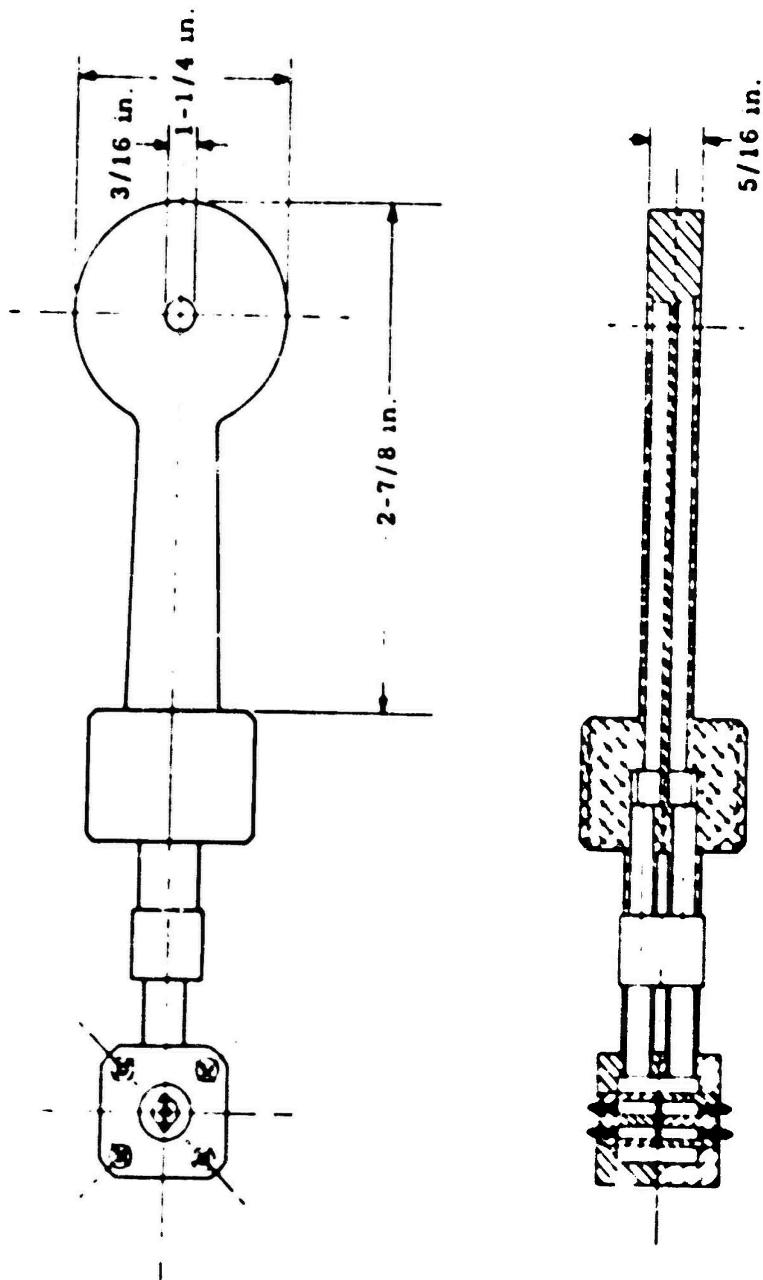


Fig. 3.7 -- Detail Drawing of Sensing Element for q-Tube

TABLE 3.4 - Dynamic Pressures - q-Tube

Shot No.	Sta No.	Gage No.	Elev (ft)	Ground range (ft)	t <sub>a</sub> (sec)	t <sub>r</sub> (sec)	Δt <sub>2</sub> (sec)	q <sub>1</sub> (psi)	q <sub>2</sub> (psi)	Δt <sub>+</sub> (sec)	Δt <sub>-</sub> (sec)
1	3-289	89q12	10	2600	1.0712	-	0.0126	0.69	2.29	0.730	a
9	P-208	08q11	11.6	4075	2.8249	-	-	1.81	-	0.88	3.00
10	P-208	08q11	11.6	3918	2.1317	-	-	0.65	-	0.67	b
	P-208	89q60	60	6386	4.146	-	-	0.160	-	b	b

a Instrument destroyed during blast  
b Not readable

TABLE 3.5 - Comparison of Measured and Calculated Dynamic Pressures, q-Tube

Shot No.	Gage No.	q (measured) (psi)	q (calculated) (psi)	Fractional deviation
1	89q12	0.69	0.52	+ 0.33
	89q12	2.29	2.30	- 0.038
9	08q11	1.81	1.76	+ 0.028
10	08q11	0.65	0.48	+ 0.35
	89q60	0.160	0.10	+ 0.60

UNCLASSIFIED

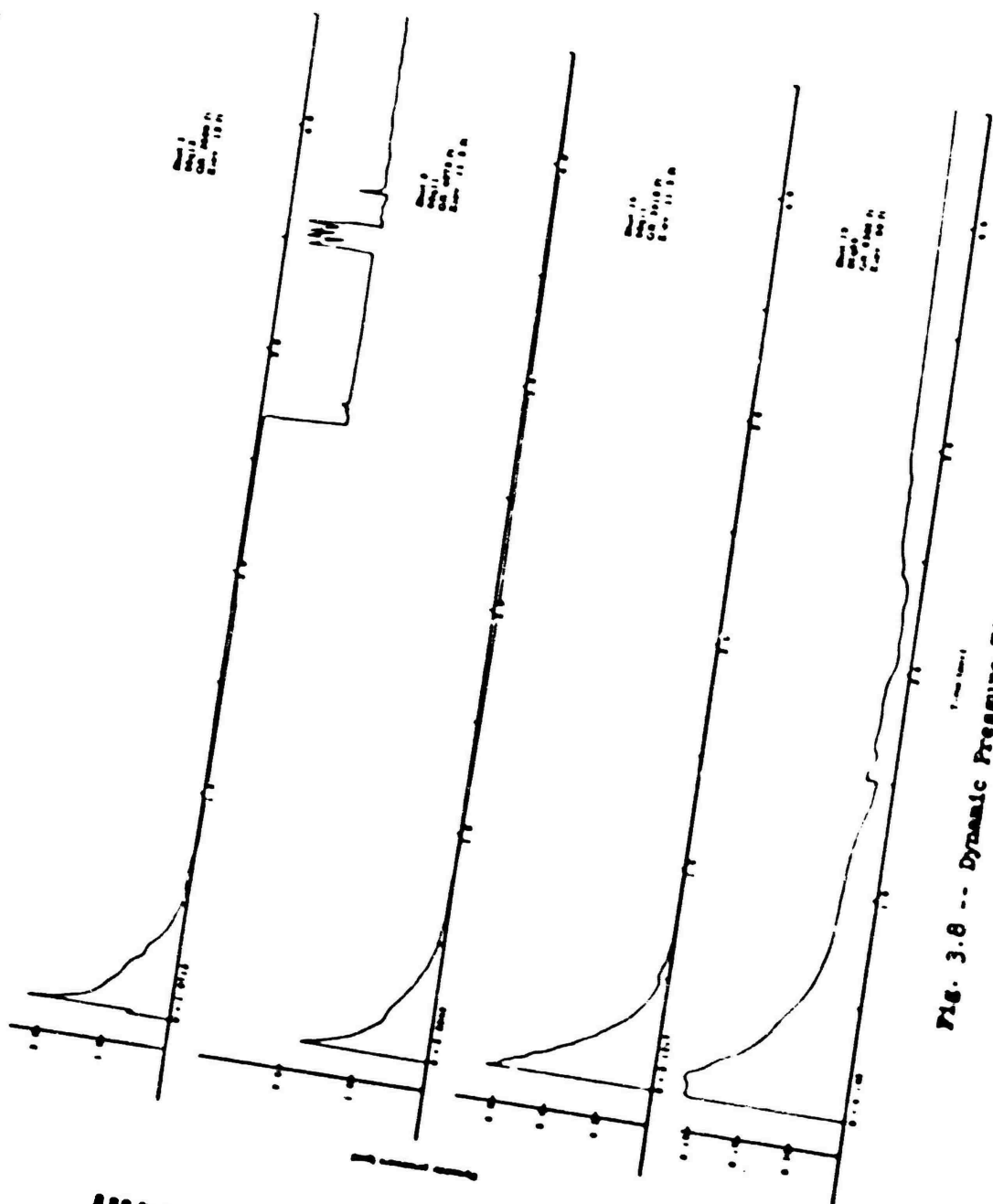
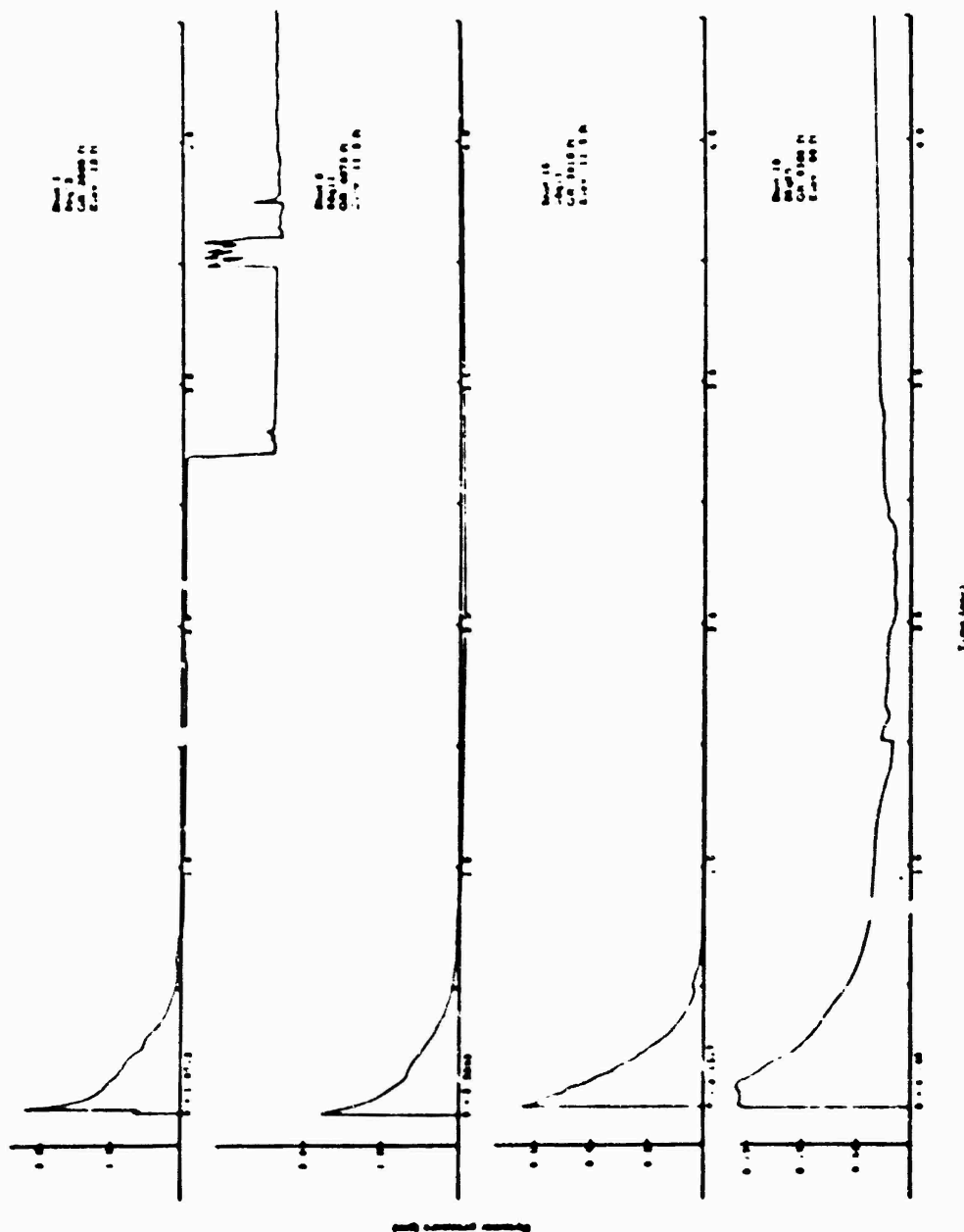


Fig. 3.8 -- Dynamic Pressure-Time Waveforms from q-Tube

UNCLASSIFIED



**UNCLASSIFIED**

65

~~CONFIDENTIAL~~



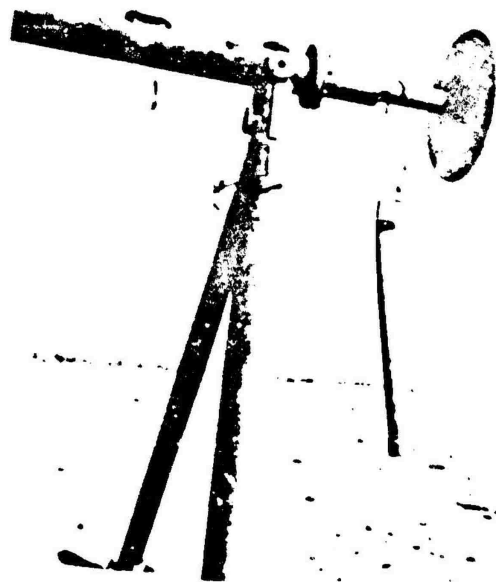


Fig. 3.9 -- Post-Shot View of Station 3-289,  
Showing Piece of Pipe which  
Apparently Knocked the q-Tube at  
this Station from its Mount

dynamic pressure that deviated rather seriously from the calculated  $q$ , it must be borne in mind that measurement was made at a low overpressure level and also that little is known about the effect of the tree stand itself on dynamic pressures.

#### 3.3.4 Conclusions and Recommendations

It is felt that the generally good agreement of the dynamic pressures measured by the q-tube with those measured by the pitot-static gage and those calculated from the measured overpressures is an indication that the gage in its present form is suitable for use in the field. The gage as used in these tests was acoustically underdamped and did ring, but matching the acoustical damping of the two lead-in tubes to the pressure pickups and making it more nearly critical would reduce this ringing.

### 3.4 WHISTLE TEMPERATURE GAGE

#### 3.4.1 Background

A need for accurate experimental data on preshock air temperatures resulting from full-scale detonation of nuclear weapons has been recognized for some time. In its present form the resistance temperature gage developed by Sandia Laboratory for use in measuring temperatures within the shock wave<sup>11,12</sup> is unsuitable for making preshock measurements because of its inherent susceptibility to heating by thermal radiation from the fireball. Previous experimental measurements of preshock temperatures have made use of thermocouples<sup>27</sup> and of instruments designed to measure sonic transit times.<sup>22,28</sup> These instruments were not completely ideal for use in the field. If thermocouples are to have a fast response, they must be made small and become rather fragile for use under field conditions. Sonic velocity methods have the drawbacks of being subject to noise interference and requiring complex electronic equipment.

The whistle temperature gage which was field-tested for the first time on UPSHOT-KNOTHOLE was originally conceived as a means for measuring preshock temperatures. During its development it appeared that it might also function throughout the shock wave and measure temperatures both prior to and following the arrival of the shock front.

#### 3.4.2 Instrumentation

The whistle temperature gage is essentially an open-ended resonant cavity which is caused to whistle by drawing air past its open end by means of a vacuum pump. A standing wave is thus formed whose wave length,  $\lambda$ , is four times that of the cavity. The speed of sound for air,  $c$ , the frequency,  $f$ , and the temperature,  $T$  (in degrees Kelvin), are related as

$$c = \lambda f, (c/c_0)^2 = T/T_0.$$

Thus the frequency depends only upon the air temperature, and if the ambient frequency,  $f_0$ , is measured at temperature  $T_0$ , a corresponding measurement of frequency  $f$  provides a measure of temperature  $T$ .

A microphone picks up the output of the whistle and feeds it to an FM discriminator (Fig. 3.10) whose output is in turn recorded on a galvanometer. The deflection,  $d$ , of the galvanometer is proportional to the frequency of the whistle. Thus if zero deflection corresponds to  $f_0$  at  $T_0$ ,

$$f = f_0 + kd.$$

From these relations the temperature of the air can be computed.

This method of recording the signal from the gage was adopted during the planning stage when it was uncertain whether the Ampex

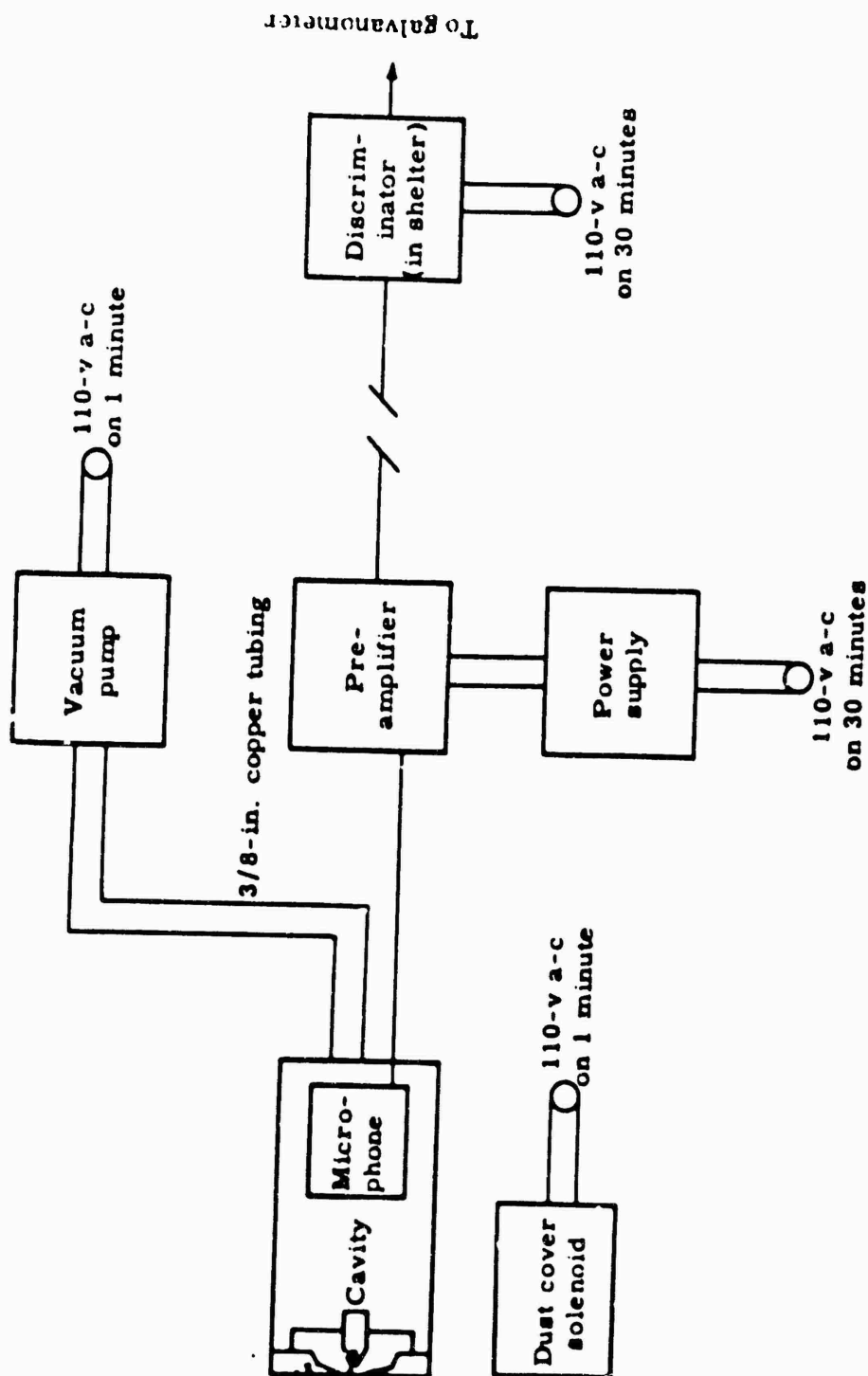


Fig. 3.10 -- Block Diagram Showing Operation of Whistle Temperature Gage

FORMERLY RESTRICTED DATA

Handle As Restricted Data In Foreign

Dissemination Section 144

Energy Act 1954

68

SECRET

magnetic tape recorder would be available for use in the field. Recording could be considerably simplified if the microphone output signal were directly recorded by the Ampex recorder.

A detail drawing of the gage in its mount is presented as Fig. 3.11. Invar, an alloy having a temperature expansion coefficient of essentially zero, was used for the resonant cavity. The cavity is mounted in the front of a canister similar to that of the Wiancko air pressure gage, and the microphone is mounted in the rear of the canister. A side-on baffle of the kind used for air pressure measurements serves as a mount for the canister assembly. A solenoid-operated drop-away shield helps prevent the cavity from filling with dust prior to use.

Experimental models of the whistle temperature gage were installed at Station 3-289 on Shot 1 and at Station F-217 on Shot 10. Figure 3.12 shows the gage mounted at Station 3-289 with the dust cover removed.

### 3.4.3 Results and Discussion

Data from these two stations are presented in Table 3.6. On Shot 1 the gage operated satisfactorily until shock arrival and showed no change in temperature. Upon arrival of the shock front, however, operation of the gage became intermittent; it did operate during the last portion of the positive phase and throughout cross over into the first portion of the negative phase. If the record is extrapolated back to arrival time of the shock wave, the extrapolated value for peak temperature is in good agreement with that measured by the resistance temperature gage.

On Shot 10 the tape which had been placed over the orifice of the cavity after calibration to provide a semipermanent seal against entering dust was inadvertently left on during the shot. Consequently the gage did not function at all on this shot.

### 3.4.4 Conclusions and Recommendations

Whereas both full-scale and laboratory tests have indicated that the whistle gage can be used to measure air temperatures, it is doubtful whether the gage in its present form will function throughout passage of the shock wave. It is possible that its response during passage of the shock wave may be improved by redesign of the orifice and cavity.

Certainly before this gage is satisfactory for field use it will have to be modified to eliminate the tendency for dust to clog the cavity and interfere with its operation. Measures should be taken to eliminate bulky accessory equipment like the vacuum pump. Laboratory study should be continued, but no plans made to use the gage on full-scale field tests until the results of such a study become available.

FORMERLY RESTRICTED DATA

Handle As Restricted Data in Future  
Dissemination Section 1.44b, Atomic  
Energy Act 1954.

SECRET

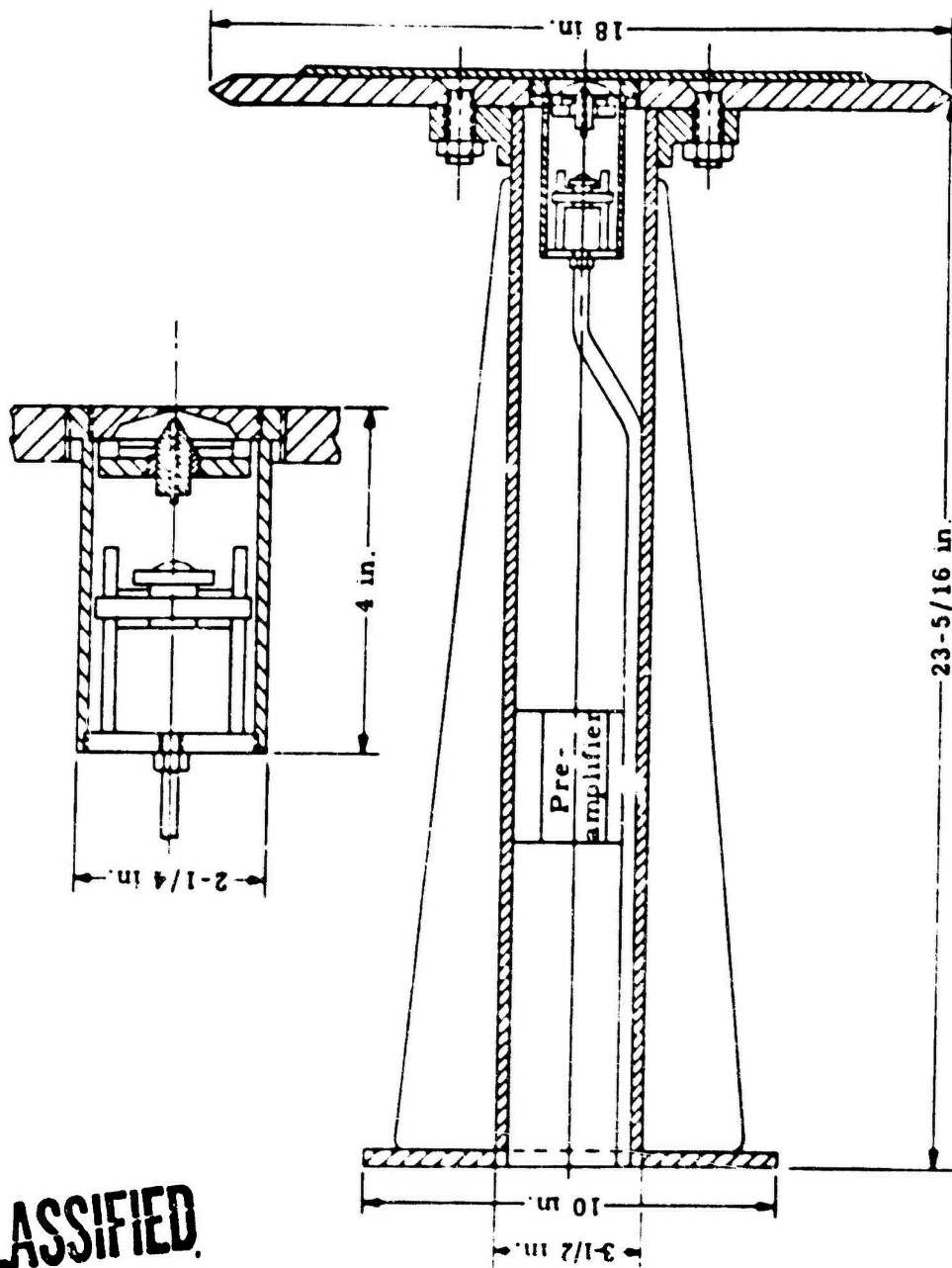


Fig. 3.11 -- Detail Drawing of Whistle Temperature Gage

UNCLASSIFIED

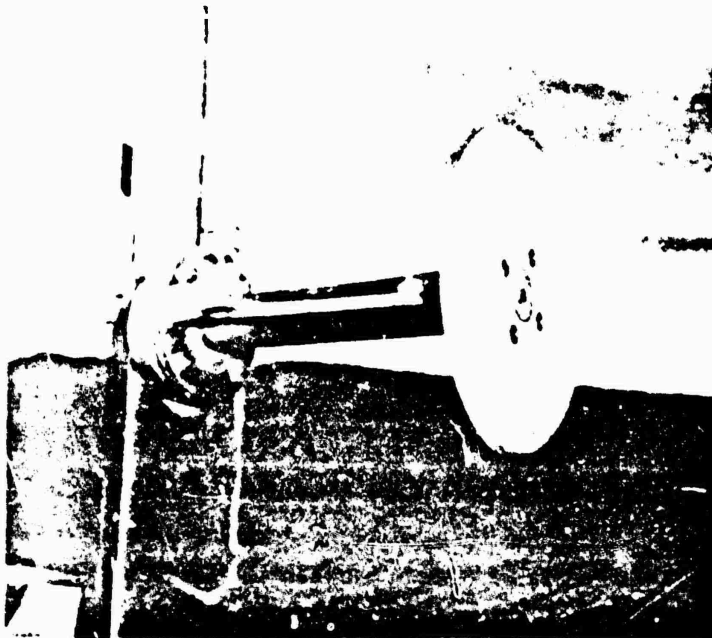


Fig. 3.12 -- Whistle Gage Mounted in the Field with Dust Cover Removed

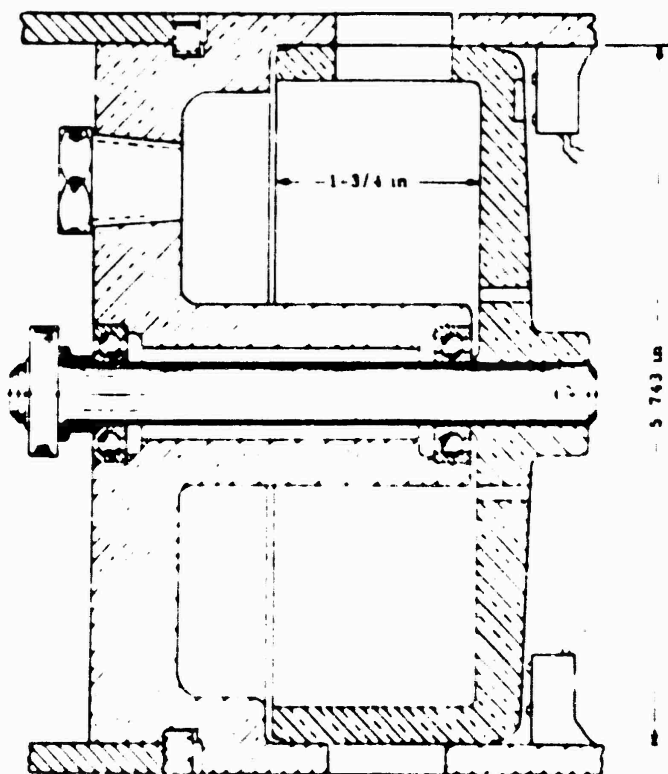
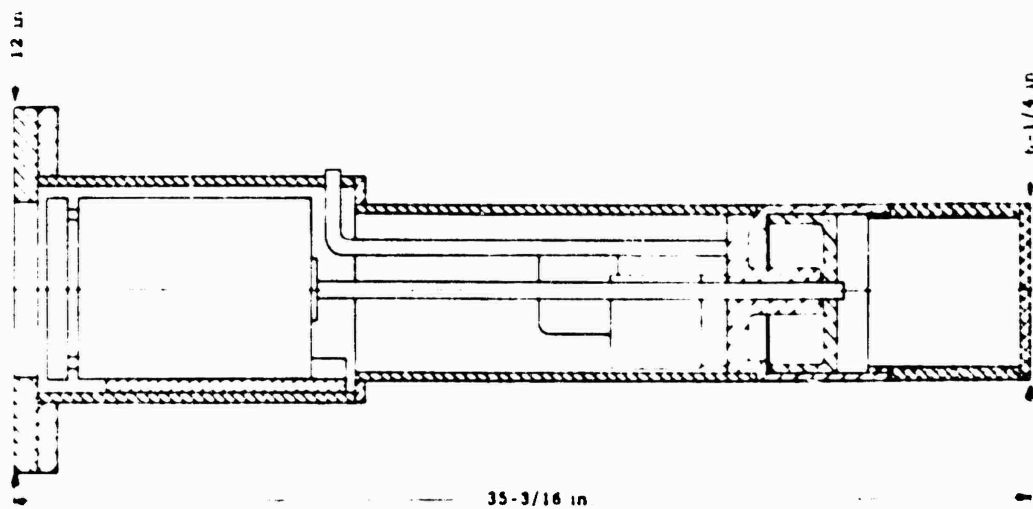
TABLE 3.6 - Temperatures, Whistle Temperature Gage

Shot No.	Sta No.	Gage No.	Ground range (ft)	$t_a$ (sec)	$\Delta T$ ( $^{\circ}\text{C}$ )	$\Delta T$ ( $^{\circ}\text{C}$ ) (calcd)	$\Delta t_+$ (sec)	$\Delta T_o$ ( $^{\circ}\text{C}$ )
1	3-289	89TW10	2600	1.0714	49 <sup>a</sup>	43	0.59	0
10	F-217	17TV10	1422	Did not function				

<sup>a</sup>Operation intermittent; extrapolated value

UNCLASSIFIED

~~CONFIDENTIAL~~  
~~CONFIDENTIAL~~  
~~CONFIDENTIAL~~  
~~CONFIDENTIAL~~



**UNCLASSIFIED** -- Detail Drawing of Siren Sound Source for SWASST

### 3.5 SONIC WIND AND SOUND SPEED INDICATOR (SWASSI)

#### 3.5.1 Background and Theory

This instrument was designed to measure wind and sound speeds when wind direction is known; essentially it is a speaker-microphone arrangement incorporating equipment to measure transit times of sound pulses in two opposite directions. In the form in which it was used on TUMBLER-SNAPPER<sup>11</sup> and IVY<sup>12</sup> the gage did not operate properly because the sound source, a crystal transducer, did not deliver sound pulses powerful enough to override the noise produced by the shock wave. The crystal transducer used as the receiver rings at its natural frequency when struck by the shock wave, and in earlier models it was necessary that the transmitted pulse be of the same frequency to obtain the desired sensitivity. As a result there was no way of distinguishing the transmitted signal from this shock-induced noise. Both defects have been corrected by using a more powerful pulse of a frequency differing from the natural frequency of the receiver.

#### 3.5.2 Instrumentation

A pulsed siren is used as the sound source in the current modification of the SWASSI (Fig. 3.13). The siren is a rotor-stator type, and it emits a pulse whose length, frequency, and repetition rate are governed by the rotational speed and geometry of the rotor-stator openings. At the normal rotational speed of 135 rps the pulse length is approximately 400 msec and its frequency 19.4 kc. The waveform closely resembles a sine wave, and the sound beam has a full width of about 70°, over which the intensity is nearly constant. Timing signals to mark the emission of each sound pulse are generated by a small magnet mounted on the rotor and coils mounted on the stator.

The microphones have a flat response in the 19.4-kc region, and while their sensitivity is less than at their natural frequency of 50 kc, the powerful signal from the siren results in outputs in excess of those from the 50-kc signal in earlier models. Since the received pulse is fed to a tuned amplifier, any 50-kc noise is filtered out. These amplifiers have a band width of approximately 4 kc; consequently the rotor speed is critical within 5 per cent if the signal is to be passed by the amplifiers. The detection, amplification, and recording systems and calibration procedures are analogous to those used with earlier models.<sup>11</sup>

A single SWASSI was installed on Shot 1 and two on each of Shots 9 and 10. In Fig. 3.1 the SWASSI is shown mounted on the cross piece of a goal post tower. The center pipe contains the siren and the two end pipes the receivers. The crosspiece was aligned at an angle of 45° with the line from ground zero to the center pipe of the gage. Except for that at Station P-217 on Shot 10 it was anticipated that all gages would be in regions such that ideal shock waves would obtain.

The output of one of the receiver amplifiers used on Shot 1 was displayed on an oscilloscope and photographed to obtain detailed information about the size and shape of the transmitted pulse as compared with those of any noise pulses.



### 3.5.3 Results and Discussion

Table 3.7 is a compilation of data for Shots 1, 9, and 10. On Shot 1 the siren did not attain its proper operating speed until about 10 seconds after arrival of the shock front because the line voltage to the motor was too low. Consequently the pulses from the receivers were not strong enough to trigger the interval timer. A photographic record of the microphone output did indicate, however, that the problem of noise interference has been solved, for only one noise pulse at the instant of shock arrival was of sufficient amplitude to trigger the interval timer.

TABLE 3.7 - Sound and Wind Velocities - SWASSI

Shot No.	Sta No.	Gage No.	Ground range (ft)	$t_a$ (sec)	$\Delta T$ ( $^{\circ}C$ )	$\Delta T$ (calcd) ( $^{\circ}C$ )	$u$ (ft/sec)	$u$ (calcd) (ft/sec)
1	3-289	89SWS13	2600	No record				
9	F-217	17SWS13	1683	1.400	50	66	300	350
	F-208	8SWS13	14060	2.810	40	47	410	406
10	F-217	17SWS13	1422	No record past zero time				
	F-208	8SWS13	3918	No record past zero time				

On Shot 9 the gage at Station F-217 operated satisfactorily, but that at Station F-208 failed about 100 msec after arrival of the shock front because of mechanical binding in the rotor of the siren. This defect was corrected prior to using the same gage on Shot 10. The measured peak temperatures and particle velocities in the shock wave are compared with those calculated from the measured overpressures in Table 3.7. Agreement is not particularly good. There was a much larger scatter in the transit times of the transmitted pulses emitted between zero time and the end of the positive phase of the shock wave than in those measured before zero time and after the end of the negative phase. The scatter prior to shock arrival is probably attributable to local turbulence caused by thermal interaction. Also the actual ground zero on Shot 9 was displaced to an extent that the direction of the blast winds was more nearly along the line of the transmitter and receivers rather than at an angle of  $45^{\circ}$ , and there was very likely interference from the turbulent wake of the mounting pipes along an appreciable portion of the sound path.

On Shot 10 all gages functioned properly until zero time when three of the four records went off scale. Presumably this malfunction was the effect of the electromagnetic transient on the interval timers, although the exact cause cannot be determined. This difficulty had

UNCLASSIFIED

UNCLASSIFIED

never been experienced on previous experiments and was totally unexpected.

A comparison of the records from the free runs at calibration time with the prezero-time portions of the records from Shots 1, 9, and 10 in the light of the ambient temperatures and winds has indicated that the electronic detection system is not sufficiently stable and that the transit times may be considerably in error.

#### 3.5.4 Conclusions and Recommendations

As it stands the SWASSI is still not a field gage. One of the principal defects of earlier models has been overcome in incorporating the pulsed siren sound source. However, the electronic system for measuring transit times is unsatisfactory still, and work is in progress on further remedial modification.

UNCLASSIFIED



## APPENDIX A

### ABBREVIATIONS AND SYMBOLS

A	In gage code, accelerometer
a	(subscript) air
B	In gage code, back dynamic pressure element of pitot-static gage
b	Ratio of density of dust suspended in air to that of air
c	Speed of sound
D	In gage code, density element of the density gage
d	(subscript) dust
DS	In gage code, static pressure element of the density gage
E	Energy gained by the mass of material in a unit volume behind the shock front in passing through the shock front
e	Internal energy per unit mass
F	In gage code, front dynamic pressure element of the pitot-static gage
GR	Ground range; distance from GZ to a specified position
GZ	Ground zero; point directly beneath burst
g	Acceleration of gravity ( $32.2 \text{ ft sec}^{-2}$ )
h	Specific heat of dust
I	Impulse per unit area
i	(subscript) incident shock wave
M	Momentum per unit area
m	Mass per unit area
n	Registering coefficient for dust (multiplying factor for $\rho u^2$ which gives the dynamic pressure of dust)
o	(subscript) ambient condition ahead of shock front
P	Pressure
$\Delta P$	Overpressure

$q$  Dynamic pressure ( $\frac{1}{2} \rho u^2$ )  
 $q$  In gage code, the q-tube  
 $q_c$  Stagnation pressure minus free-stream static pressure  
 ( $q_c = q(1 + 0.25 M^2 + 0.025 M^4 + \dots)$ )  
 $q_{1,2,3,4}$  Dynamic pressure measured at time  $\Delta t_{1,2,3,4}$   
 $r$  (subscript) reflected shock wave  
 $S$  In gage code, static pressure element of pitot-static gage  
 $SW$  In gage code, sonic wind and sound speed indicator (SWASSI)  
 $T$  Temperature  
 $\Delta T$  Temperature increase in shock wave  
 $t$  Time  
 $\Delta t$  Time interval after arrival of shock wave  
 $t_a$  Time of arrival of first pressure signal of blast as  
 referred to zero time of burst  
 $TR$  In gage code, resistance temperature gage  
 $TW$  In gage code, whistle temperature gage  
 $U$  Shock velocity  
 $u$  Particle velocity  
 $V$  Specific volume ( $V = 1/\rho$ )  
 $Y$  In gage code, yawmeter  
 $y$  Ratio of dynamic pressure in dust-laden shock to that in  
 clean shock  
 $\alpha$  Angle between incident shock front and reflecting plane  
 $\gamma$  Ratio of specific heat at constant pressure to that at  
 constant volume  
 $\eta$  Ratio of density behind shock front to that in front of  
 shock front ( $\rho/\rho_0$ )  
 $\lambda$  Wave length  
 $\mu = \frac{\gamma + 1}{\gamma - 1}$   
 $\rho$  Density  
 $\rho_c$  Ratio of absolute pressure behind shock front to that in  
 front of shock front  
 $\varphi$  Yaw angle  
 $\theta$  Pitch angle

**FORMERLY RESTRICTED DATA**

Handle As Restricted Data in Foreign  
 Dissemination Section 144B, Atomic  
 Energy Act 1954

77

**SECRET**

UNCLASSIFIED

## APPENDIX B

SUMMARY DATA FOR OPERATION UPSHOT-KNOTHOLE

	Shot 1	Shot 9	Shot 10	Shot 11
Date	March 17	May 8	May 25	June 4
Time (GMT)	1320: 00.329	1529: 55.302	1530: 00.332	1514: 56.675
Location (area)	T-3	FF	FF	T-7-3 (over Station 3-303)
Yield (KT)	16.2	26	14.9	60.8
Method	RC	RC	RC	RC
Height of burst (ft)	300 (tower)	2423 (air)	524 (air)	1334 (air)
Height of burst (ft) (scaled to 1 KT at sea level)	112	763	204	316
Ground zero (relative to aiming point) (ft)		837 S 15 W	139 S 86 W	232 N 172 W
Atmospheric pressure (mb)				
Ground zero	876	900	901	867
Burst height	800	825	804	824
Air temperature (°C)				
Ground zero	2.7	16.7	14.8	13.3
Burst height	7.9	8.0	13.1	12.2
Relative humidity (%)				
Ground zero	43	19	32	30
Burst height	38	23	23	38
Surface wind (direction and velocity) (knots)	calm	190 05	360 04	045 03
Atmospheric transmission (% ml)	94	92.5	91	93

APPENDIX C

MEASURED WAVEFORMS, SHOTS 1, 9, 10

UNCLASSIFIED

~~XXXXXXXXXXXXXXXXXXXX~~  
~~XXXXXXXXXXXXXXXXXXXX~~  
~~XXXXXXXXXXXXXXXXXXXX~~  
~~XXXXXXXXXXXXXXXXXXXX~~

~~XXXXXXXXXXXXXXXXXXXX~~  
~~XXXXXXXXXXXXXXXXXXXX~~

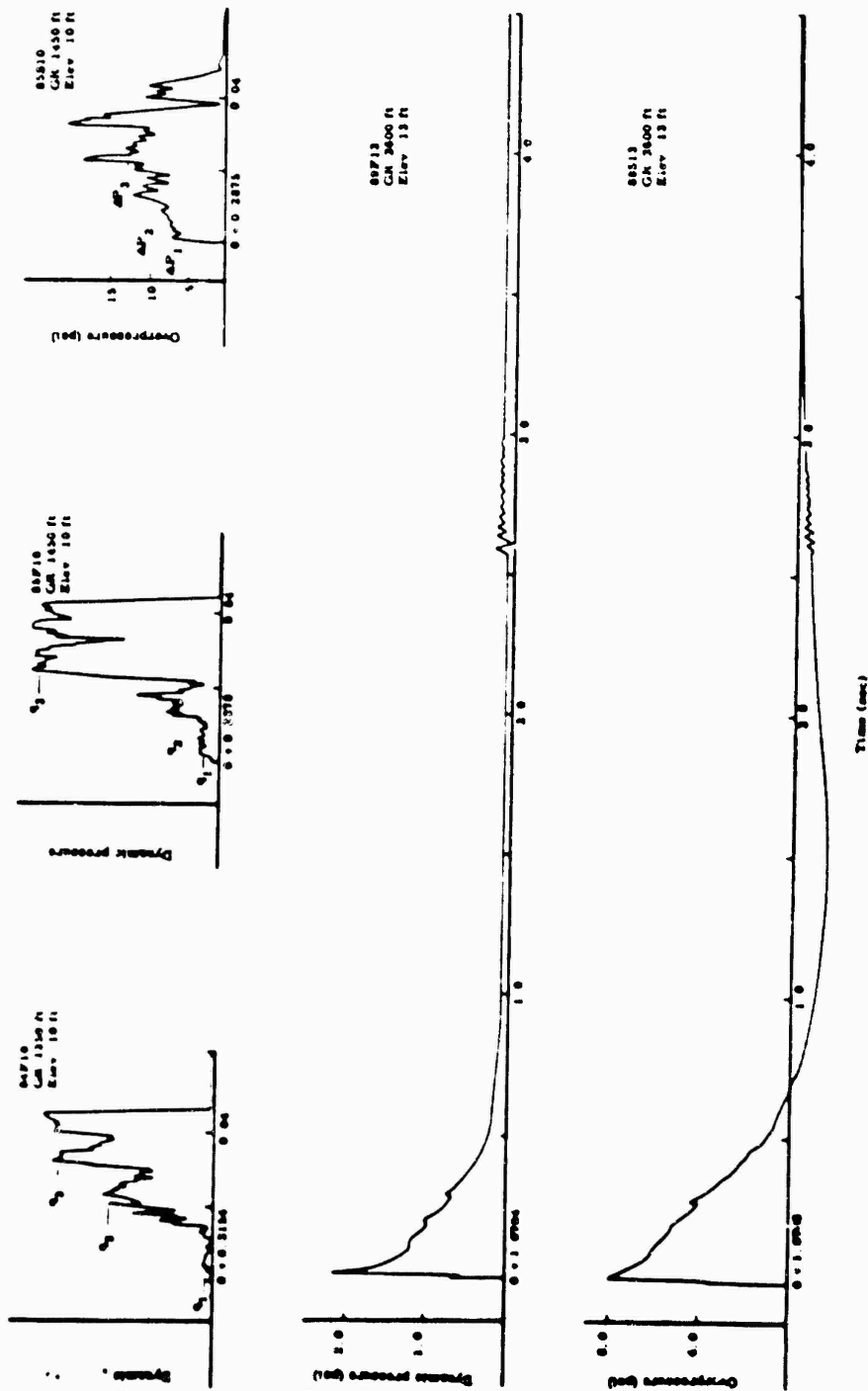


Fig. C.1 -- Pressure-Time Waveforms -- Pitot-Static Gage, Shot 1

UNCLASSIFIED

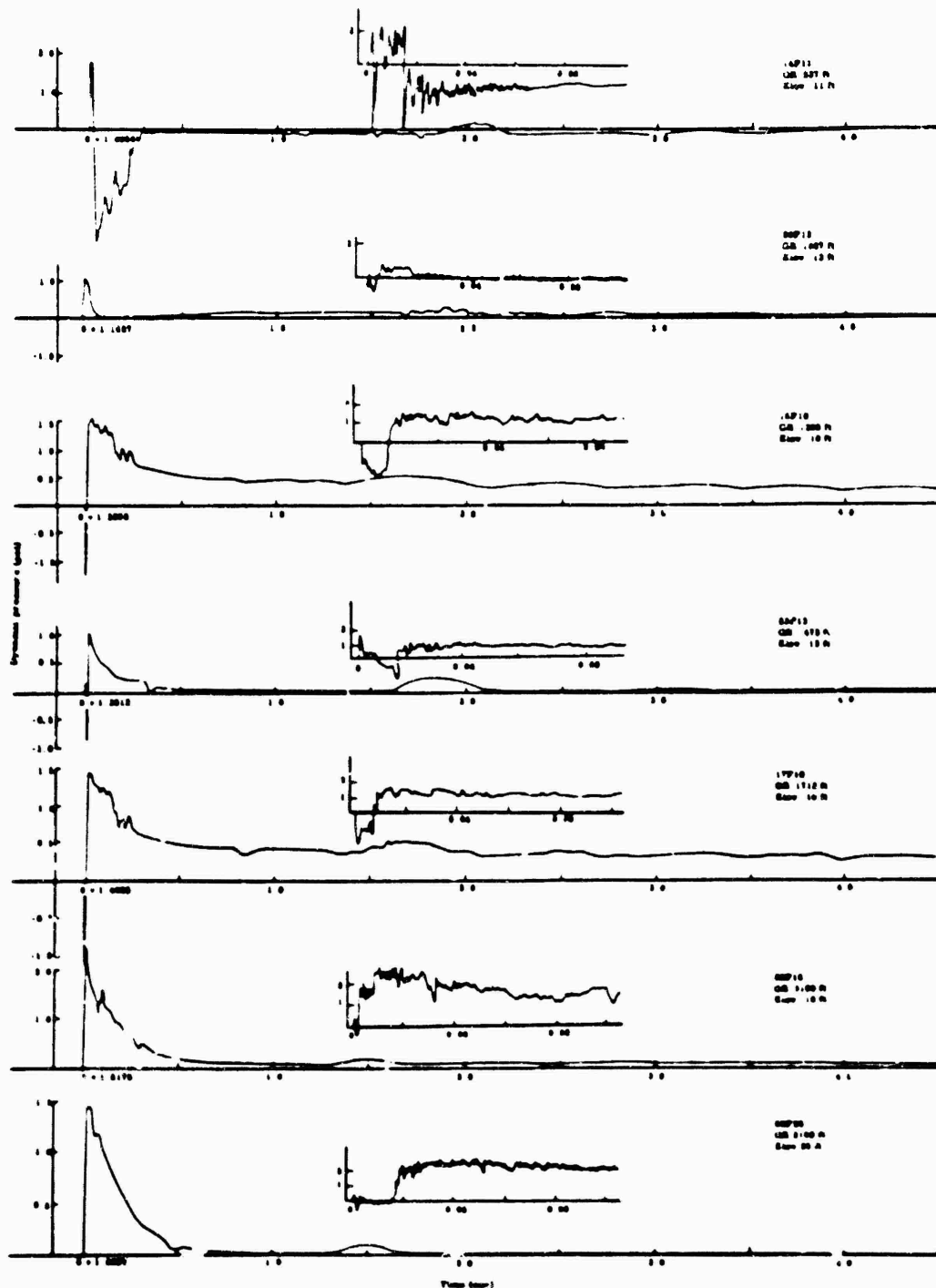


Fig. C.2 -- Dynamic Pressure-Time Waveforms -- Pitot-Static Gage, Shot 9

UNCLASSIFIED



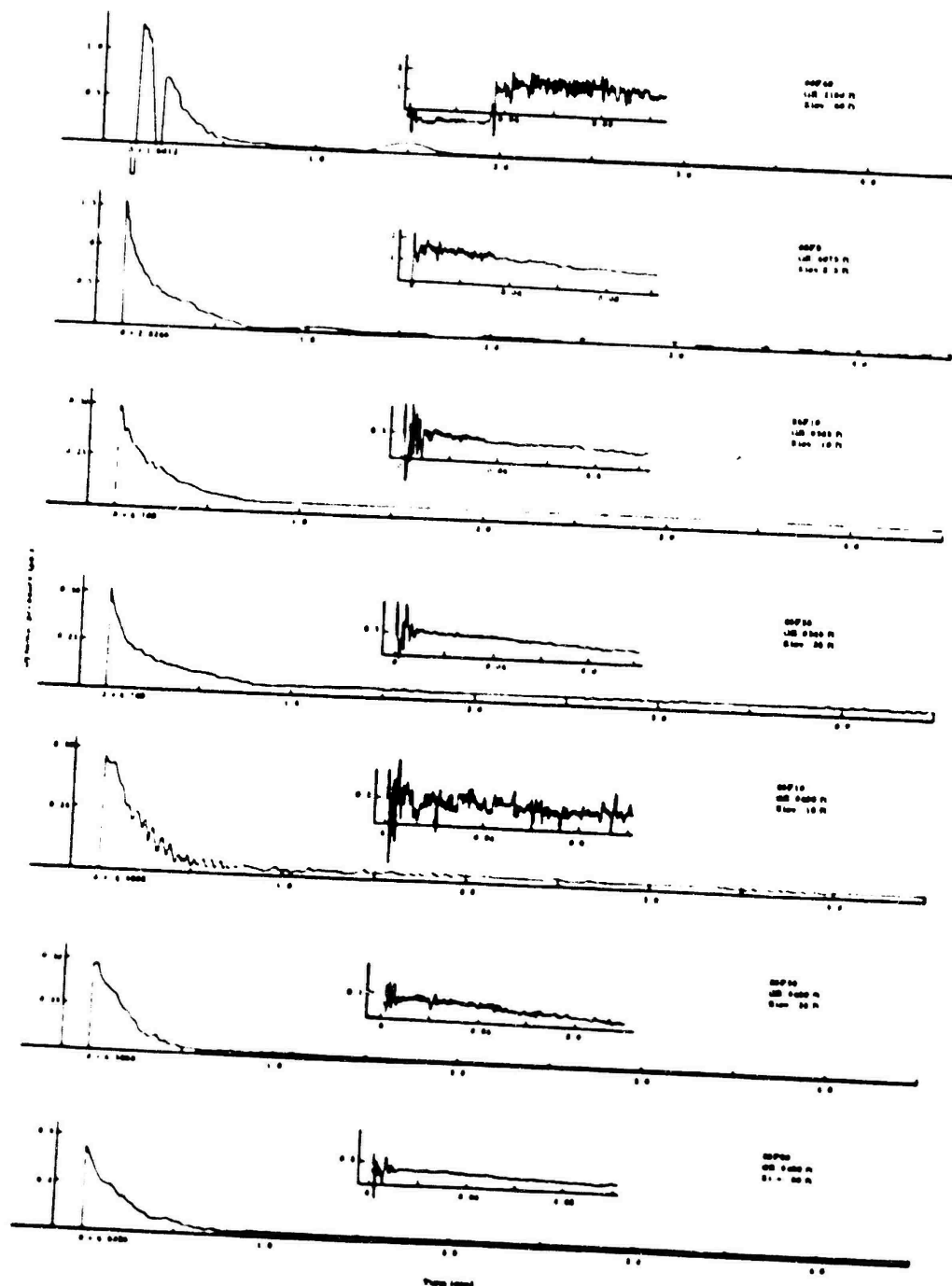


Fig. C.3 -- Dynamic Pressure-Time Waveforms -- Pitot-Static Gage, Shot 9

UNCLASSIFIED

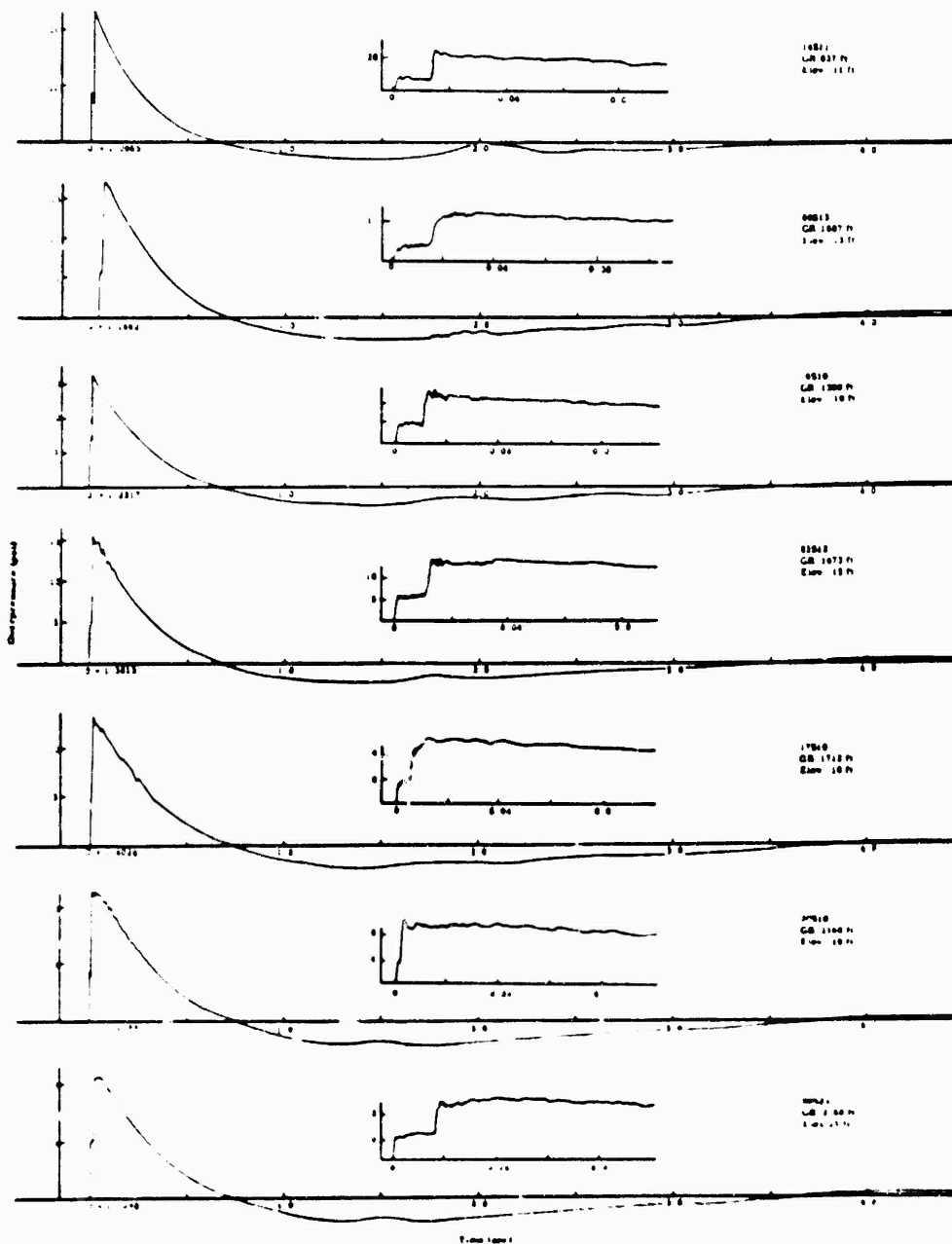


Fig. C. 4 -- Overpressure-Time Waveforms -- Pitot-Static Gage, Shot 9

**UNCLASSIFIED**

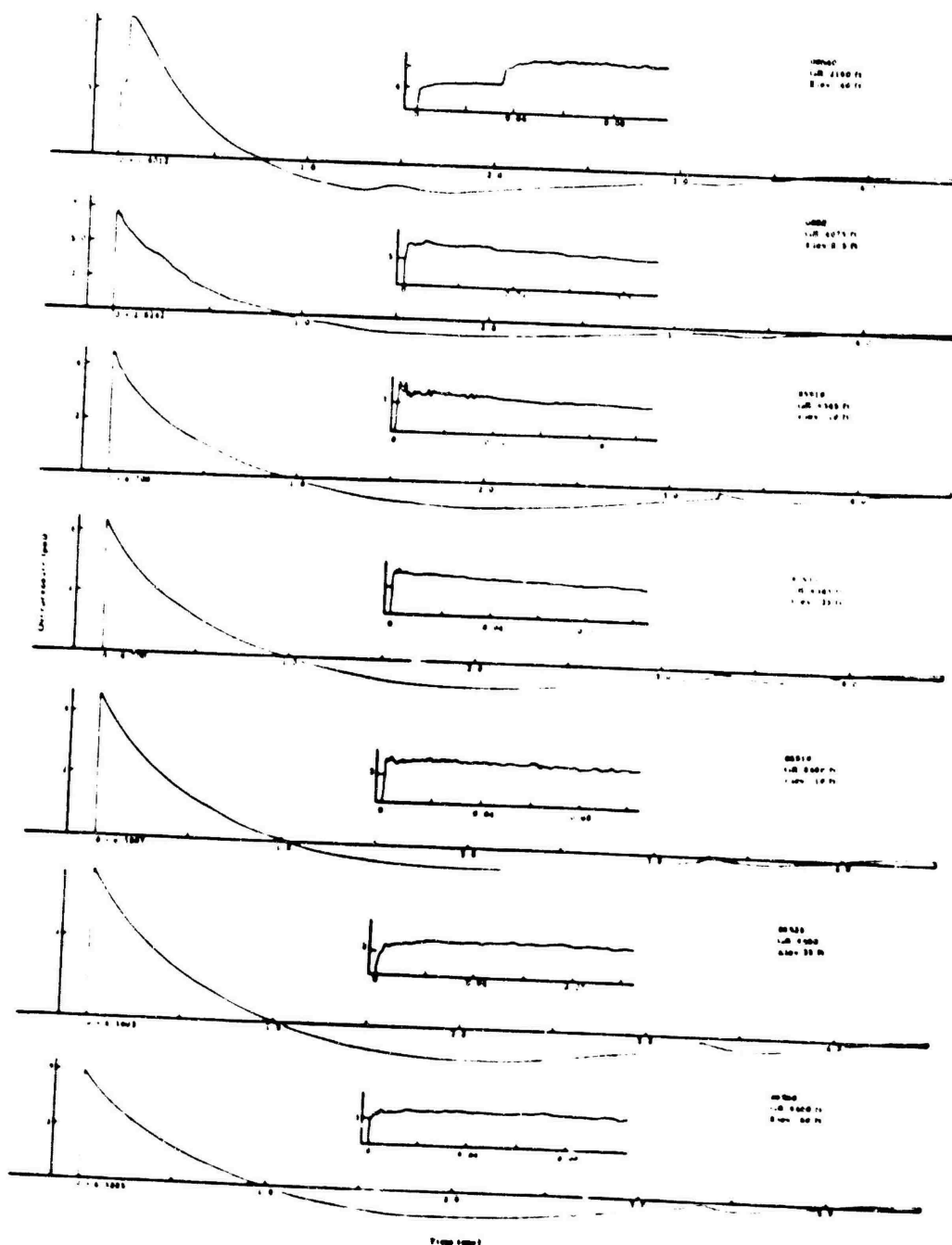


Fig. C.5 -- Overpressure-Time Waveforms -- Pitot-Static Gage, Shot 9

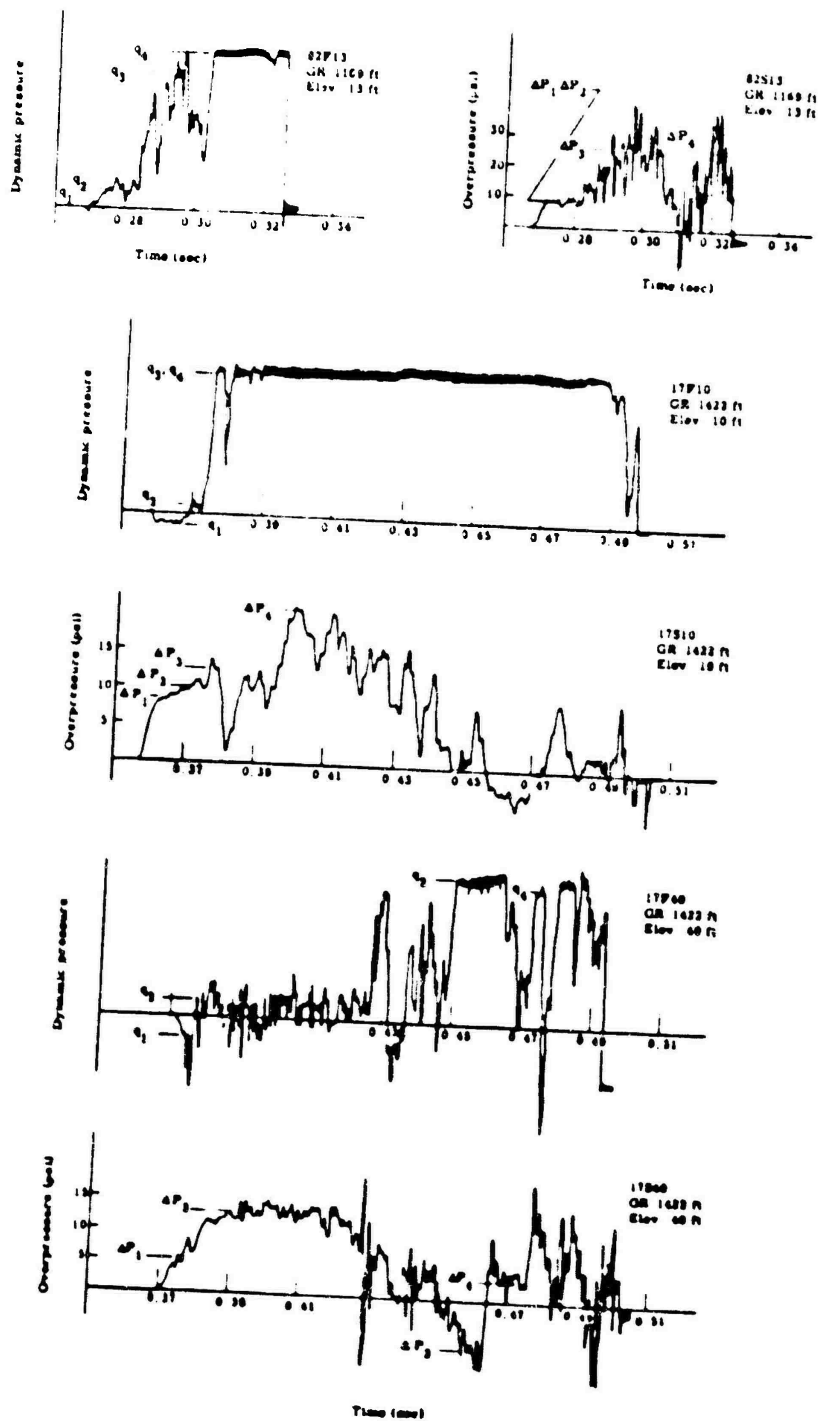


Fig. C. 5 -- Pressure-Time Waveforms in Precursor -- Pitot-Static Gage, Shot 10

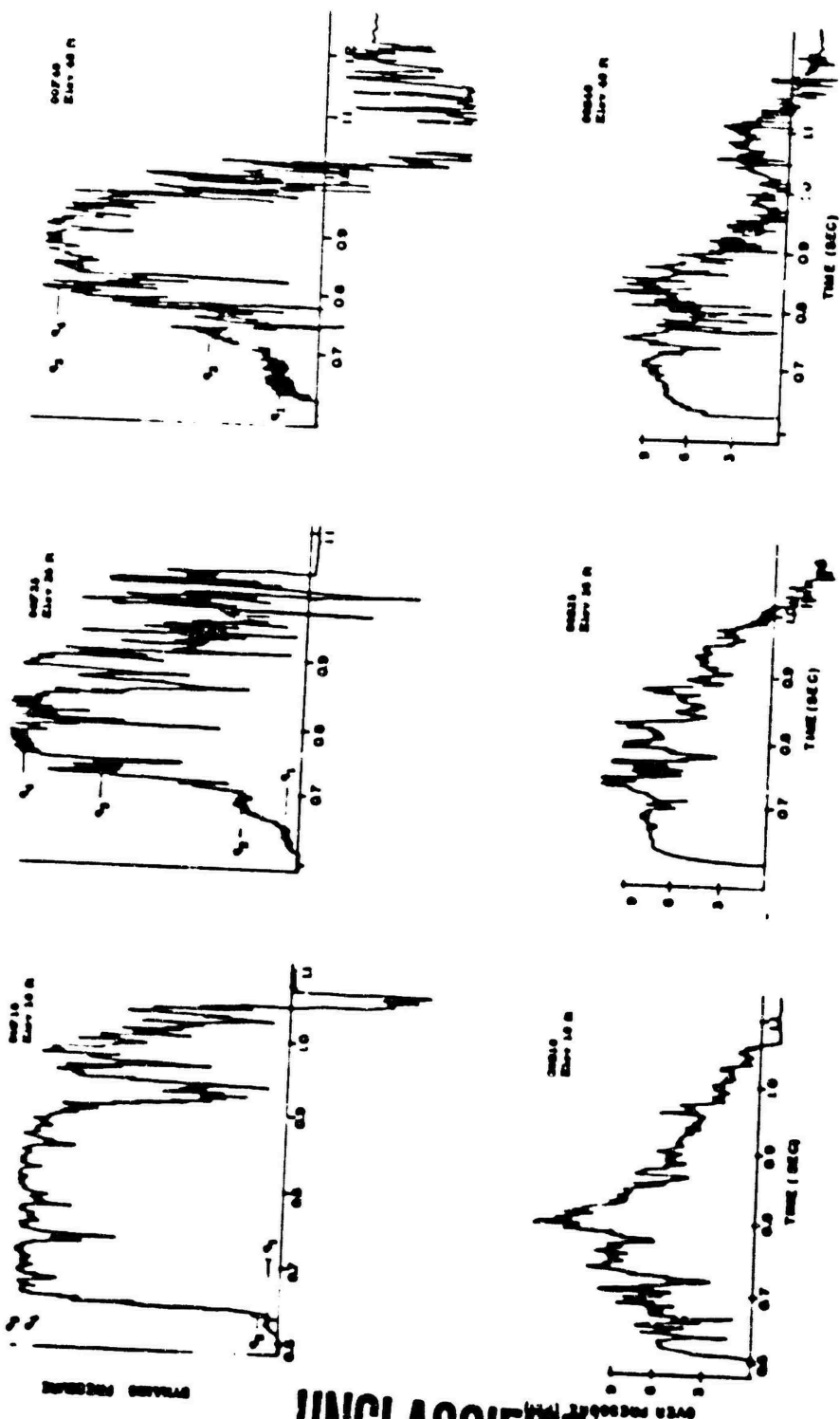


Fig. C.7 -- Pressure-Time Waveforms in Precursor -- Pitot-Static Gage, Shot 10

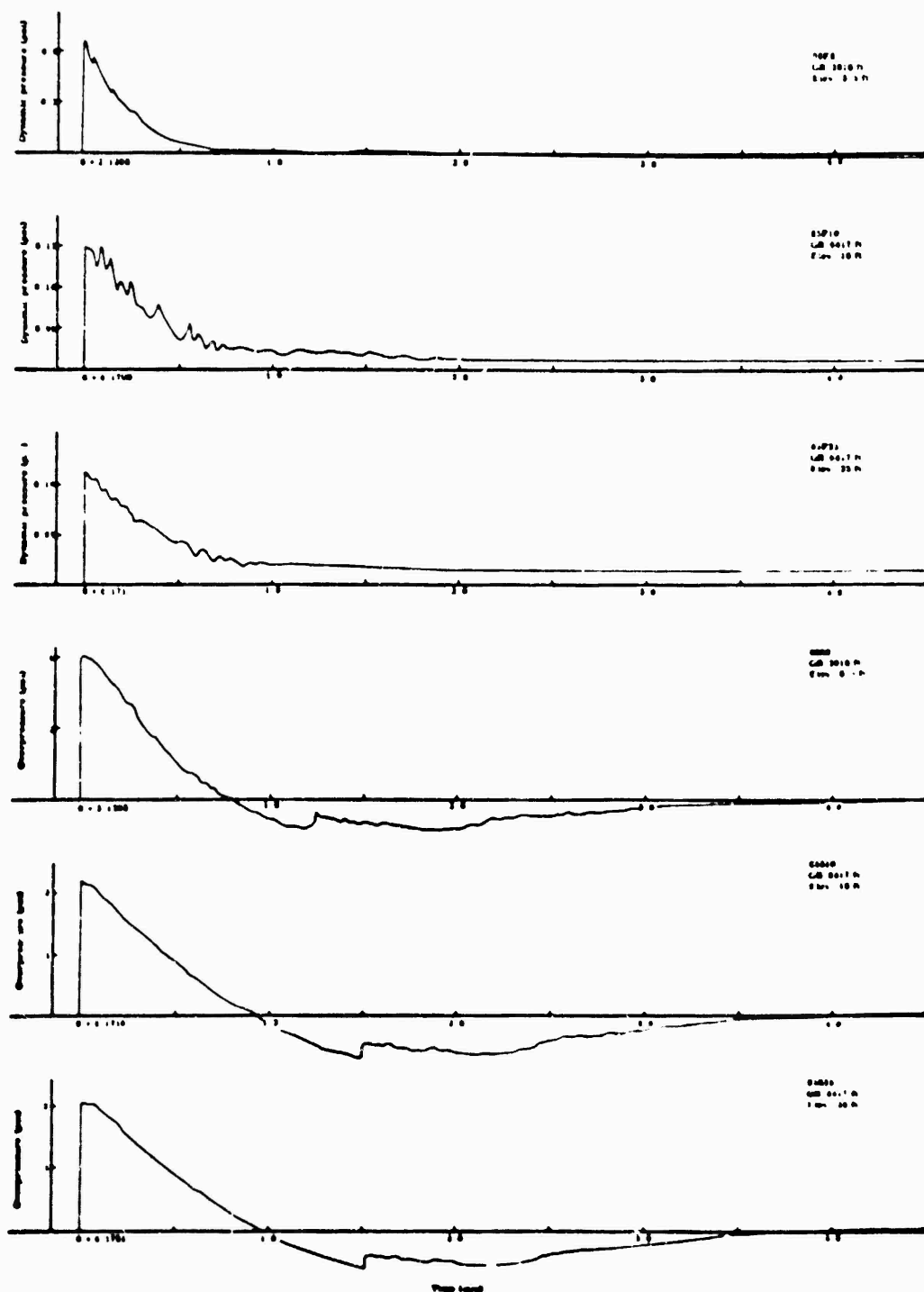


Fig. C.8 -- Pressure-Time Waveforms (Nonprecursor) -- Pitot-Static  
Gage, Shot 10

UNCLASSIFIED

87

~~FORMERLY RESTRICTED DATA~~

~~SECRET~~

~~NO DISTRIBUTION OUTSIDE THE COMSEC~~

~~SECRET~~

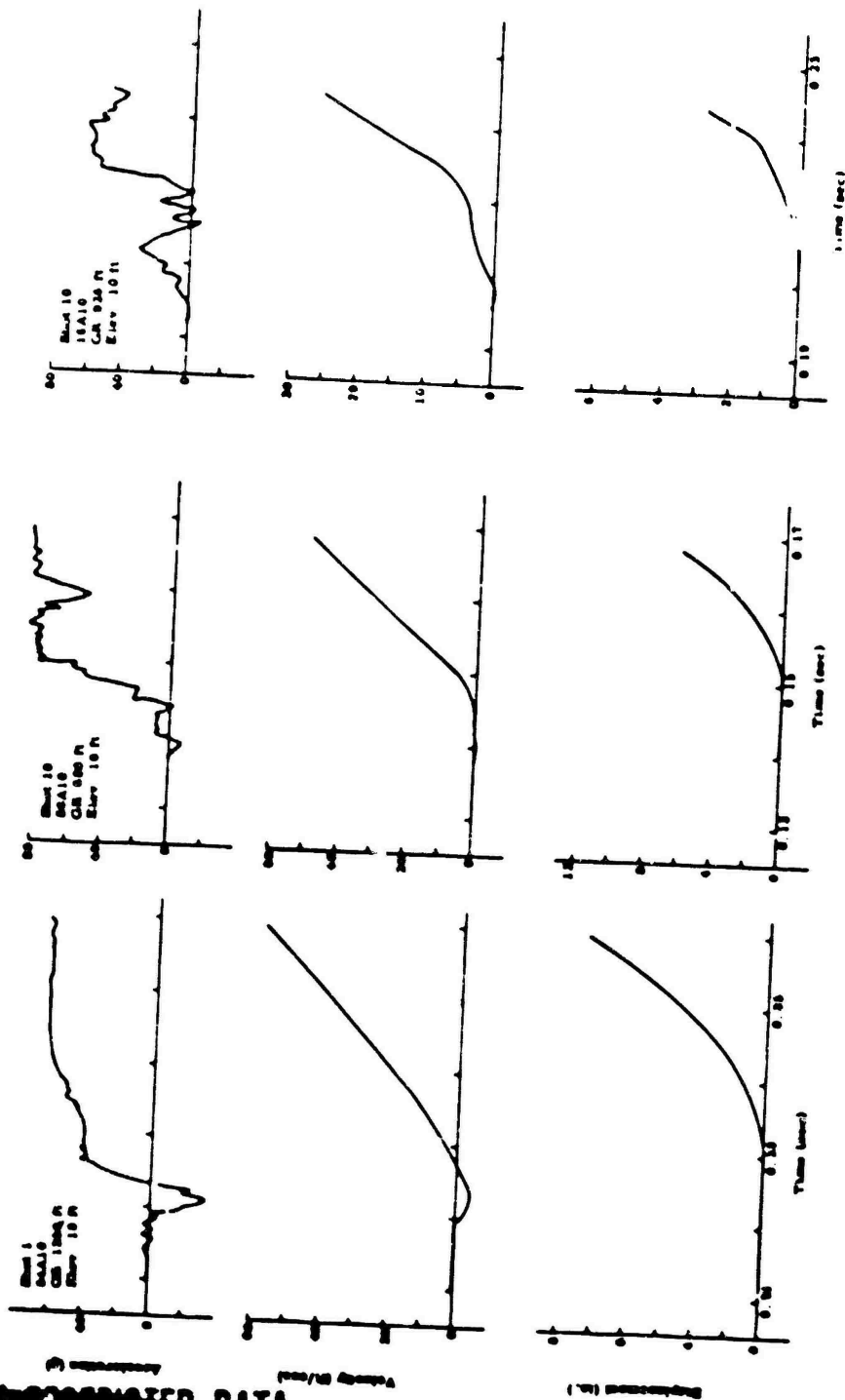


Fig. C.9 -- Acceleration, Velocity, and Displacement Waveforms -- Shots 1 and 10

## APPENDIX D

### PRELIMINARY INVESTIGATION OF THE RESPONSE OF PRESSURE GAGES TO DUST-LADEN AIR

J. R. Banister & C. D. Broyles

In full-scale nuclear explosions dust is often suspended in the air both before and after passage of the shock front, its concentration being greater behind the front. This dust is of concern because it may alter the waveform of the shock wave and because its concentration may be so great as to affect the dynamic load imposed upon an obstacle. During recent nuclear explosions dynamic pressures measured in regions of large quantities of suspended dust were higher than would be computed from the measured overpressure using the Rankine-Hugoniot shock relations.

This observation was at variance with the results of a cursory shock-tube experiment by Cook and Richardson<sup>19</sup> designed to investigate the effect of dust loading of a shock wave on dynamic pressures recorded by a differential pressure gage. They used a 4-msec square pressure pulse loaded with chalk dust and a pair of Wiancko air pressure gages oriented to simulate the Wiancko differential pressure element of a pitot-static gage. Although they found dynamic pressures little changed by dust during passage of the positive pulse, their results were difficult to interpret, particularly because it was uncertain whether the sharp spike which appeared in the record three milliseconds after passage of the shock wave was attributable to dust striking the gage or to some other phenomenon caused by the dust. They chose to neglect it, and decided that dust probably does not register on a Wiancko gage. Their conclusion seemed reasonable because the gage is so constructed that the dust momentum could have been absorbed by the acoustical damping material.

The possibility that the pressure spike observed by Cook and Richardson could be a result of dust loading and the results observed on full-scale tests led to reinvestigation of the problem in the present series of shock-tube experiments.

#### D.1 EXPERIMENTAL PROCEDURE

Experimental arrangements for the current study are similar to those used by Cook and Richardson with two exceptions. A finely powdered sand ( $\text{SiO}_2$ ) and a pulverized pumice, both of which probably contained particles of smaller size than the chalk dust used in earlier

UNCLASSIFIED

~~CONFIDENTIAL~~

~~CONFIDENTIAL~~

~~CONFIDENTIAL~~

~~CONFIDENTIAL~~



experiments, have been used. Also the positive pulse is of longer duration so that the dust is in the positive pulse when it arrives at the gage; ambiguous results can thereby be avoided, for it is now fairly certain that the spike observed in dynamic pressure curves from the earlier experiment was caused by dust striking the gage.

Both Rutishauser and Wiancko gages are used for these measurements, the Rutishauser gage being used as a standard against which to evaluate the performance of the Wiancko gage. The response of the Rutishauser gage to dust may be anticipated to a certain extent and thus give some idea of the distribution and velocity of the dust at the gage position.

A complete description of these gages and their operation is not essential here; however, some characteristics of the pickup elements are significant in interpreting the experimental results. The pressure pickup of the Wiancko gage<sup>22</sup> incorporates a variable reluctance controlled by rotation of a bourdon tube. This tube is subject to acoustic resonance which is damped by placing a Fiberglas wick inside it; the gages used in this experiment are so damped.

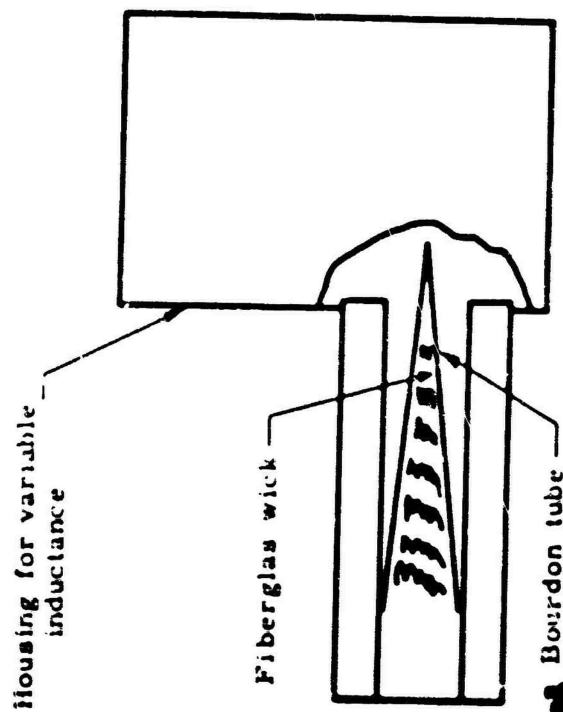
The pressure pickup of the Rutishauser gage is a variable-capacitance stator-diaphragm arrangement such that a change of capacitance between the stator and diaphragm produces a voltage signal which is nearly proportional to the pressure applied at the diaphragm. The face of the gage is  $3/4$  inch in diameter; the diaphragm, which is  $3/16$  inch in diameter, is at the center of and flush with the face. Because of its rapid response, details of the load imposed on the gage may be examined closely. Schematic cross sections of the two gages are shown in Fig. D.1.

A third type of pressure gage, the model P4-0 manufactured by the Beta Corporation, was used in some preliminary measurements. Like the Rutishauser gage it is a diaphragm-type gage but cannot be calibrated statically. It uses an electrokinetic transducer.<sup>23</sup>

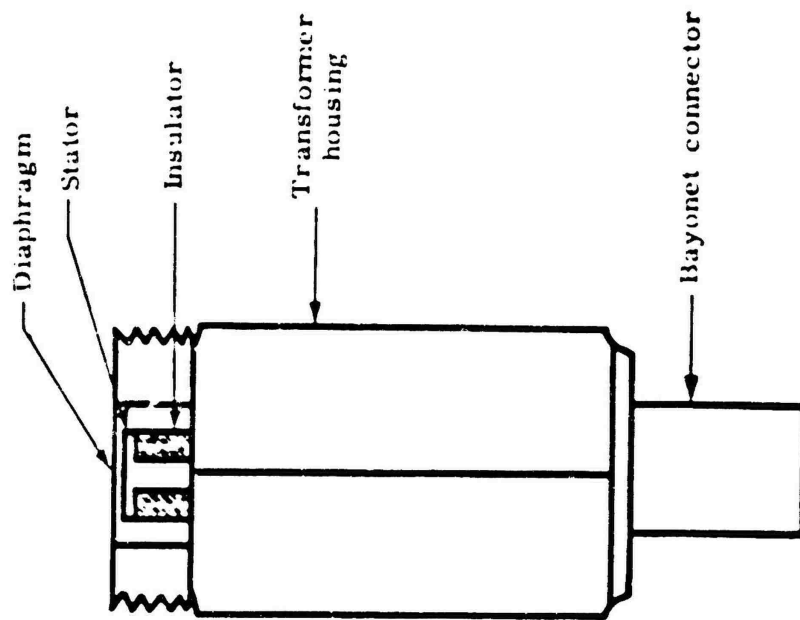
These gages are mounted in the shock tube in a manner similar to that described by Cook and Richardson. A nearly square pressure pulse is produced in the usual fashion.<sup>24</sup> This pulse passes through a screen approximately 4 feet from the cellophane diaphragm separating the compression chamber from the expansion tube, and a side-on and head-on gage are placed 8-1/4 inches beyond the screen (Fig. D.2). The compression chamber is long enough to produce a positive pulse of 10 msec.

Dust is added to the shock wave by loading the screen as uniformly as possible with weighed quantities of dust. Since all dust on the screen is removed by the shock wave, the amount of dust in suspension may be arrived at by estimating the percentage of dust shaken off during installation of the screen. Loads of about  $0.08 \text{ g cm}^{-2}$  (heavy load) and  $0.04 \text{ g cm}^{-2}$  (light load) are used; control runs are made using an unloaded screen.

Ranges of dust diameters are determined by microscopic examination of the dust on a calibrated slide. Particle diameters of the sand range from less than one to ten microns, those of the pumice from ten to one hundred microns. Specific gravities of both types of dust particles are estimated to be 2.5.



WIANCKO



RUTISHAUSER

Fig. D.1 -- Cross-Sectional Views of Wiancko and Rutishauser Gages

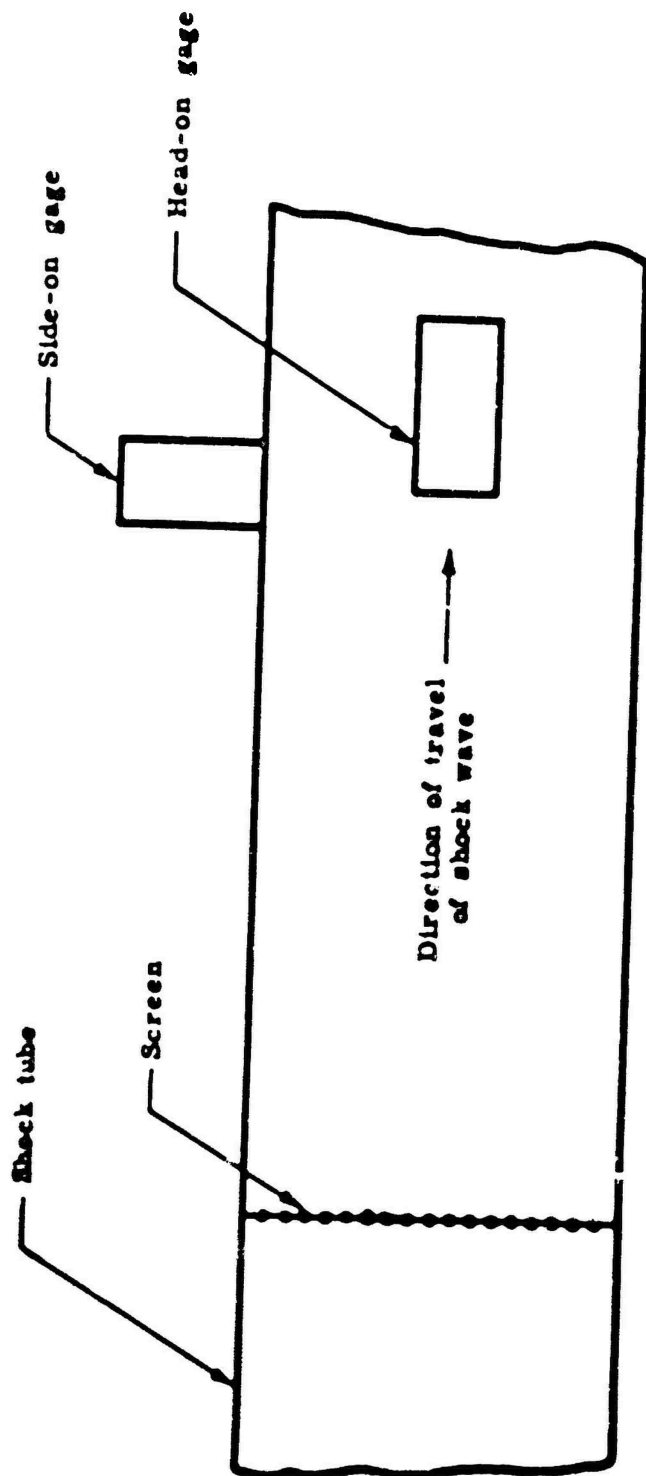


Fig. D.2 -- Diagram of the Experimental Arrangement

UNCLASSIFIED

Initial shock overpressures (before the shock strikes the screen) are 7.0 and 3.8 psi. Side-on measurements indicate that the screen attenuates the overpressure by 9 per cent for the stronger shock and 8 per cent for the weaker, but without significantly changing the wave shape.

Pressure-time records are obtained by feeding the outputs of the gages to a Tektronix Type 512 cathode-ray oscilloscope and using a Polaroid oscilloscope camera to photograph the traces. Records are obtained from the head-on gage alone, from the side-on gage alone, and of the difference between the readings of the head-on and side-on gages (dynamic pressure or  $q$ ).

All gages are calibrated by the static-pressure method, and care is taken that the sensitivities of all side-on and head-on pairs used for dynamic pressure measurements are equal.

Because the clean pressure pulse is approximately square, the Rankine-Hugoniot shock relations and the equations of state for air may be used to calculate various characteristic parameters of the shock wave which has passed through the dust-free screen. Computed values for these parameters of the strong and weak shock waves are listed in Table D.1.

TABLE D.1 -- Computed Characteristics of the Clean Shock After Passing Through the Screen

Shock over-pressure (psi)	Shock velocity (ft/sec)	Material velocity (ft/sec)	Density of air pulse ( $\text{g cm}^{-3}$ )	Dynamic pressure (psi)
6.2	1,380	352	0.00130	1.1
3.6	1,280	219	0.00117	0.38

Positive pulse duration: 10 msec      Ambient pressure: 12 psi  
Room temperature: 25°C, 298°K      Ambient density: 0.000967  $\text{g cm}^{-3}$   
Speed of sound: 1,140 ft/sec

## D.2 SOME THEORETICAL ASPECTS OF THE PROBLEM

One of the first questions that arises in an analysis of the experimental results is the manner in which the dust is accelerated. While it might at first seem that the shock front is responsible for dust acceleration, an elementary approximate calculation shows that this cannot be true for dust particles of ordinary density. Let us consider a single particle struck by the shock front, the force on which is approximately 2 PA where P is the shock overpressure, A is the frontal area of the particle, and the factor of 2 accounts for the

UNCLASSIFIED

pressure doubling at reflection. This force acts for a time  $x/U$  where  $x$  is the distance the shock must travel to envelop the particle and  $U$  is the velocity of the shock front. The total momentum imparted is approximately  $2 P \Delta x / U$ , and since the mass of the particle is approximately  $\Delta x \delta$ , where  $\delta$  is the density of the particle, the velocity imparted by the shock front alone is of the order of  $2P/U\delta$ . For a 6.2-psi shock overpressure and a particle density of  $2.5 \text{ g cm}^{-3}$  the resultant particle velocity is only 0.3 fps.

Our experimental situation is, of course, quite different in that the dust is packed into the openings of the screen and behaves more or less as a solid wall until it is driven clear. We may therefore describe the behavior of the dust by assuming the overpressure to be doubled on reflection, whereupon the force per unit area becomes  $2P$  and the acceleration of dust having a mass of  $m_d$  per unit area is  $2P/m_d$ . The differential equation is simple since acceleration is constant until the dust is clear of the screen; integrating twice and eliminating the time factor, we find that the velocity imparted to the dust in this stage is  $2 \sqrt{Ps/m_d}$ , where  $s$  is the thickness of the screen. Since this thickness is about 0.1 cm, the ejection velocity of dust is about 50 fps for heavy loads and strong shocks. This velocity is far less than that observed at the gage, and it is evident that in this phase the dust is broken up but does not attain its maximum velocity.

Drag forces, then, must account for most of the observed velocity of the dust particles. Drag forces may be approximated by using Stoke's law and assuming that dust particles behave as smooth spheres. The force on such a particle would be  $6\pi\eta r(u_a - u_d)$ , where  $r$  is the radius of the sphere,  $\eta$  the air viscosity, and  $u_a$  and  $u_d$  are the air and dust particle velocities. Using Newton's second law we may state

$$\frac{du_d}{dt} = \frac{2\eta}{2r^2\delta} (u_a - u_d) \quad (\text{D.1})$$

where  $t$  is time. This equation was used to calculate the times of Table D.2, assuming a dust particle density,  $\delta$ , of  $2.5 \text{ g cm}^{-3}$ . This treatment of drag forces is only approximate, however, since the dust particles are not smooth spheres, and at high Reynolds numbers Stoke's law gives a force lower than is observed experimentally.<sup>32</sup> Actual times required to reach various fractions of air velocity are probably considerably less than those listed in Table D.2, which should be regarded only as order-of-magnitude approximations. Moreover, Table D.2 does not imply that in the experimental arrangement dust particles attain the indicated fractions of the possible terminal velocities in the time intervals specified; this situation arises not from any failure of Eq D.1 but rather because locally  $u_a$  is reduced by dust that the air has already passed through.

**UNCLASSIFIED**

~~RESTRICTED DATA~~

~~RESTRICTED DATA~~

~~RESTRICTED DATA~~

~~RESTRICTED DATA~~

TABLE D.2 -- Times Required for Smooth Spheres to Reach Various Fractions of the Air Velocity (from Stoke's Equation)

Particle diameter (cm)	$u_d/u_a$				
	0.1	0.3	0.5	0.7	0.9
$10^{-4}$	$0.77 \times 10^{-6}$ sec	$2.6 \times 10^{-6}$ sec	$5.1 \times 10^{-6}$ sec	$8.8 \times 10^{-6}$ sec	$17 \times 10^{-6}$ sec
$10^{-3}$	Same except that the exponent of 10 is -4				
$10^{-2}$	Same except that the exponent of 10 is -2				
Specific gravity of the sphere ( $\delta$ ): 2.5-6 Air viscosity ( $\eta$ ) at $T = 40^\circ\text{C}$ : $190 \times 10^{-6}$ poise					

We may now examine the behavior of a mixture of air and dust upon encountering an obstacle, for example, a gage. This problem is not a simple one, and no analytical solution has been found as yet. If there were no dust, the problem would be relatively simple and is treated in texts on fluid dynamics.<sup>32-34</sup> For air alone the dynamic pressure, being the difference between the pressure at a stagnation point and that in free flow, would be  $q = \frac{1}{2} \rho_a u_a^2$  if we neglect the correction for the Mach number of the flow.

For dust particles of two comparatively extreme sizes the problem is also a simple one. If dust particles are of nearly molecular size, they behave in the same way as air and we may consider the density as that of the air augmented by that of the dust. If, on the other hand, dust particles are extremely large, we may neglect the effect of drag forces and the problem reduces to one of mechanics. Actual sizes of most dust particles are somewhere between these extremes, however.

For these intermediate particle sizes an approximate calculation has been made, too lengthy for inclusion here, which indicates that nearly all the dust mass moving toward an obstacle the size of a gage face does strike it, at least under the experimental conditions used here. This assumption may then be used to predict the response of the Rutishauser gage to dust. When dust particles are stopped by the diaphragm, the dust increases the apparent dynamic pressure by  $\rho_d u_d^2$ , where  $\rho_d$  is the dust density\* and  $u_d$  is the dust velocity. If the particles rebound, and if drag forces are neglected, we would expect the contribution from the dynamic pressure of the dust to be greater than  $\rho_d u_d^2$  when the mean free path of the rebounding particles is of the order of or greater than the dimensions of the gage face (or obstacle). If, on the other hand, the mean free path of the particles is small compared

\*  $\rho_d$  dust density is meant not the density of individual particles but the density of the dust as suspended in air.

UNCLASSIFIED

~~SECRET~~

Before discussing the experimental results it might be well to discuss the theoretical aspects of methods used for their evaluation. A fairly exact method would be to apply the principle of conservation of momentum since the loss in momentum for the clean and dust-laden shocks should be about equal. Unfortunately, however, it is difficult to evaluate the momentum of the dust-laden shock wave from the pressure-time records obtained, and admittedly more approximate methods must be used to analyze the data.

$$I' = \frac{1}{2} \int_0^{\tau} \rho_a u_a'^2 dt + n \int_0^{\tau} \rho_d u_d^2 dt \quad (D.2)$$
$$I = \frac{1}{2} \int_0^T \rho_a u_a^2 dt \quad (D.3)$$

Let us now consider the difference between these dynamic impulses:

$$\Delta I = I' - I = n \int_0^{\tau} \rho_d u_d^2 dt - \frac{1}{2} \int_0^{\tau} (\rho_a u_a^2 - \rho_a^i u_a^{i2}) dt. \quad (D.4)$$

**UNCLASSIFIED**

~~SECRET~~

equal to that for the clean shock. We may then write:

$$I = n \int_0^{\Delta t} \rho_d u_d^2 dt - \frac{1}{2} \rho_a (u_a^2 \Delta t - \int_0^{\Delta t} u_a'^2 dt) \quad (D.5)$$

since  $u_a$  is a constant during the interval  $\Delta t$ . Because the acceleration time of the dust particles is short and most of the dust is carried with the dust pulse, we approximate the last integral as  $\bar{u}_d^2 \Delta t$ , where  $\bar{u}_d$  is the average velocity of the dust at the gage. The actual value of the integral should be greater than this, so two of the simplifying assumptions have a tendency to cancel each other.

The first term is easily recognizable as being equal to  $n m_d \bar{u}_d$ , where  $m_d$  is the mass of dust per unit area. Thus we arrive at the expression

$$I \approx n m_d \bar{u}_d - \frac{1}{2} \rho_a \Delta t (u_a^2 - \bar{u}_d^2). \quad (D.6)$$

Note that  $n$  decreases monotonically as  $\bar{u}_d$  increases. This working expression is useful because  $\Delta I$  and  $\Delta t$  are determined experimentally and  $m_d$  is known, as are  $u_a$  and  $\rho_a$ . Certain reasonable limits may be specified for  $\bar{u}_d$ , or it may be calculated if  $n$  is assumed to be one for the Rutishauser data.

Experimental results may also be evaluated by comparing peak dynamic pressures observed for clean and dust-laden shock waves. Their ratio,  $y$ , is

$$y = \frac{(\frac{1}{2} \rho_a' u_a'^2 + n \rho_d' u_d'^2)_{\max}}{\frac{1}{2} \rho_a u_a^2} \quad (D.7)$$

Here the variables for the dust-laden shock wave are evaluated at the maximum dynamic pressure; note that we need to know  $\rho_a'$ ,  $u_a'$ ,  $\rho_d'$ ,  $u_d'$  to evaluate  $n$ ;  $y$  may be determined experimentally, and  $\rho_a$  and  $u_a$  have been calculated (Table D.1).

### D.3 ANALYSIS OF EXPERIMENTAL RESULTS

It is perhaps to the point to begin this discussion with a qualitative summation of the results as exemplified in some typical records (Fig. D.3) from the Wiansko and Rutishauser gages under various experimental conditions. All differential pressure records begin at the time the air disturbance arrives at the gage. Letter designations in the text indicate appropriate waveforms in Fig. D.3.

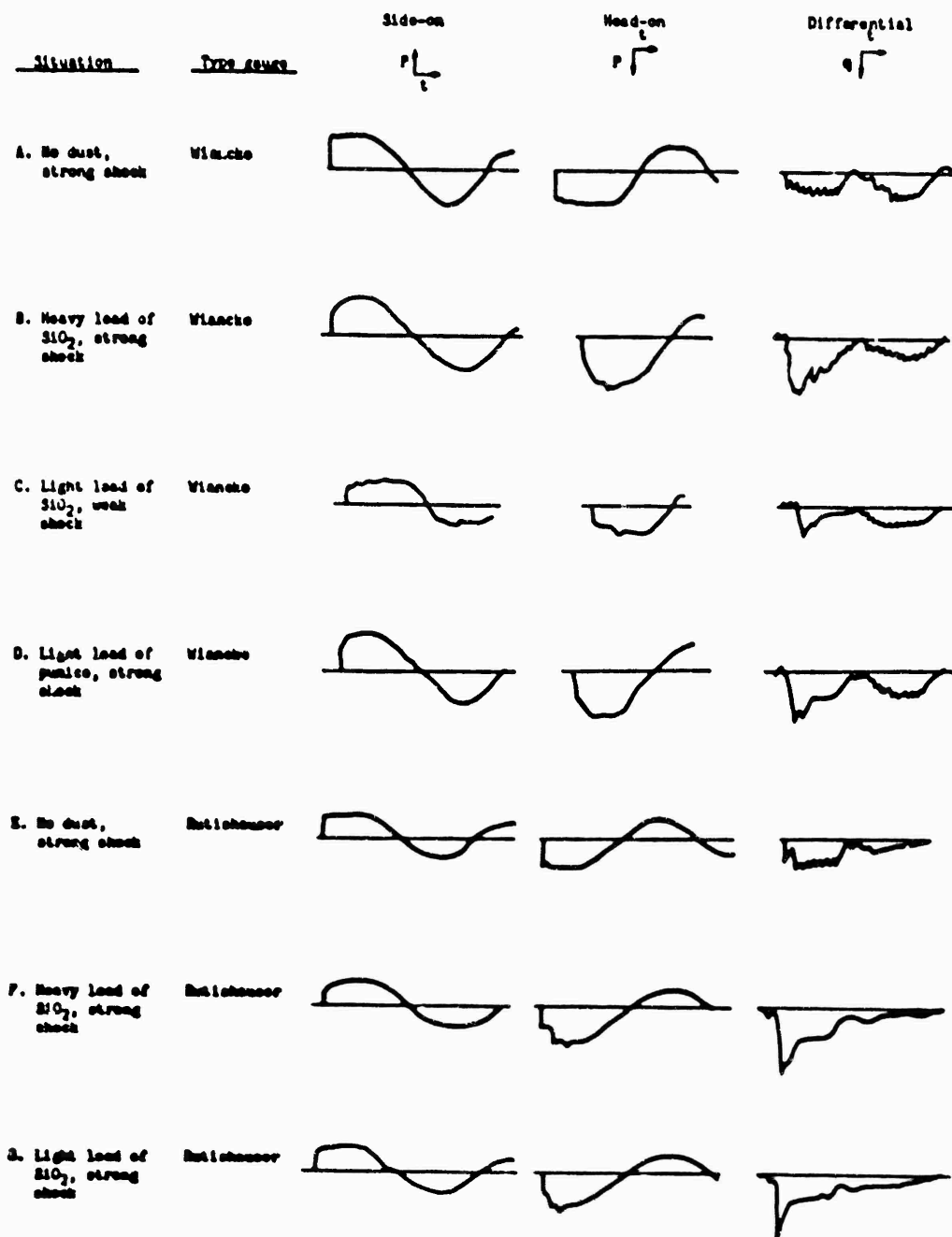
When there is no dust on the screen the waveform observed by the side-on gage (A and E) is little different from that when no screen is used although overpressures are reduced somewhat. But when dust is

**UNCLASSIFIED**

~~FORMERLY RESTRICTED DATA~~

Declassification Source 1-44, Atomic





Time scale for all traces:  $\boxed{10 \text{ msec}}$   
 Tracing starts when air disturbance arrives at gauge  
 Pressure scale varies

Fig. D.3 -- Some Wiancho and Raisensor

~~FORMERLY RESTRICTED DATA~~

**UNCLASSIFIED**

~~Handle As Restricted Data~~

~~Distribution Section 1, 2, 3, 4, 5, 6, 7, 8, 9, 10~~

~~GROUP 1, 2, 3, 4, 5, 6, 7, 8, 9, 10~~

~~SECRET~~

placed on the screen (all except A and E), the waveform is altered considerably; the pressure front is rounded, and in some instances a small shock is noted in the negative phase for the weaker shock (C).

Head-on gage records taken with and without the screen in place were quite similar except for some irregular increases\* near the end of the positive phase when no screen was used. Head-on records when the screen is dust-loaded (all except A and E) show a rounding of the pressure front similar to that in the records from the side-on gages. A rise caused by the first dust striking the gage occurs 2-3 msec after the first air disturbance, and the dust continues to register as an irregularity for several milliseconds.

Differential records taken with no dust on the screen indicate a nearly constant pressure during passage of the positive phase (A and E). When the screen is loaded with dust, these records show little displacement until arrival of the dust at the gage (all except A and E). The dust is registered as a sharp rise, the pattern varying somewhat from run to run; in general the dynamic pressure remains at a high level for about 3 msec for heavy dust loads and 2 msec for lighter loads, then drops to a level somewhat greater than would be expected for air alone.

Differential records from the Wiancko and Rutishauser gages under conditions of strong shocks and heavy loads (B and F) differ somewhat in their manner of decay from the peak value; for light loads the waveforms are similar (C, D, F, and G) and follow the pattern of the Rutishauser gage for heavy loads, ie, a plateau-type decay.

Wiancko gages in the side-on position show a slight increase with time in overpressure for the positive phase (A) whereas the Rutishauser gage in the corresponding position shows a constant overpressure (E) as does the Beta gage.

The Rutishauser gage in the head-on position shows a slight decrease in overpressure after the wave front strikes the gage (E). Fortunately this effect disappears before the dust pulse arrives.

No differences in delay time between arrival of the air and dust disturbances are noted for fine sand and pumice (B and D). Waveforms are similar although the duration of the dust pulse is somewhat longer and the dynamic pressure somewhat lower for pumice (D and G). For both heavy and light loads of pumice a plateau is observed behind the dust pulse (D).

Data from all runs are presented in Table D.3. While most of these are taken from the dynamic pressure records, the time interval between arrival of the air disturbance and arrival of the first dust was determined from the records of the head-on gage. Dynamic impulse was obtained by examining the interval between arrival of the dust pulse and arrival of the rarefaction wave from the open end of the shock tube. This interval was chosen to ensure including all the dust and to exclude complications introduced by the rarefaction. The dynamic impulse of the clean shock wave was measured for a corresponding interval.

\* Caused by cellophane shards from the ruptured diaphragm.

UNCLASSIFIED ~~FORMERLY RESTRICTED DATA~~

~~Excluded from automatic downgrading and declassification~~  
Excluded from automatic downgrading and declassification

TABLE D.3 -- Summary of Experimental Data

Initial* overpressure (psi)	Type gauge	Load per unit area (g cm <sup>-2</sup> )	Peak dynamic pressure (psi)	Delay (msec)	Dynamic impulse (psi-sec)
NO DUST					
7.0	Wiancko	-	1.1	-	0.0097
7.0	Wiancko	-	1.1	-	0.0108
7.0	Wiancko	-	1.2	-	0.0117
7.0	Rutishauser	-	1.7	-	0.0170
7.0	Rutishauser	-	1.9	-	0.0160
3.8	Wiancko	-	.2	-	0.0029
SiO <sub>2</sub>					
7.0	Wiancko	0.070	4.6	2	0.0200
7.0	Wiancko	0.064	3.3	2	0.0198
7.0	Wiancko	0.038	2.7	2	0.0133
7.0	Wiancko	0.035	3.3	2	0.0161
7.0	Rutishauser	0.085	5.0	2	0.0280
7.0	Rutishauser	0.085	4.7	2	0.0258
7.0	Rutishauser	0.047	4.4	2	0.0210
3.8	Wiancko	0.070	1.1	3	0.0064
3.8	Wiancko	0.035	1.1	3	0.0048
FUNICE					
7.0	Wiancko	0.070	3.0	2	0.0167
7.0	Wiancko	0.038	3.0	2	0.0157
3.8	Wiancko	0.035	1.1	3	0.0058

\* Before shock wave reached screen

In general, peak dynamic pressures measured by the Rutishauser gauge were higher than those measured by the Wiancko gauge under the same conditions. Comparison of dynamic pressures measured in the clean shock with those computed from theory indicates that the readings of the Rutishauser gauge were too high, probably as a result of inadequate calibration. If it is assumed that the error is one of non-linearity but that the zero trace is correct, the theoretical dynamic pressure may be used as a standard to correct\* the average peak pressure derived from the Rutishauser data, as was done in Table D.4. After this correction was made, the peak dynamic pressures read by the Wiancko gauge were the higher. In view of the correction required,

\* Readings of the Rutishauser gauge were multiplied by a factor of 1.1/1.8 where 1.1 is the theoretical value and 1.8 the average dynamic pressure observed by the Rutishauser gauge when no dust was present.

100

UNCLASSIFIED

~~SECRET~~

however, the significance of the trend is questionable. The correction was not made to the data on impulse, for to do so would lead to 'improbable results. In the future it will be advisable to use a calibration procedure that will eliminate such errors.

TABLE D.4 -- Average Peak Dynamic Pressures for Strong Shocks and SiO<sub>2</sub>

	Average dynamic pressure (psi)	
	Wiancko	Rutishauser
No dust	1.1	1.1
Heavy load	3.9	3.0
Light load	3.0	2.7

The average velocity of the first dust traveling between screen and gage may easily be calculated. Observed delays between the arrival of the air and dust disturbances were 2 msec for strong shocks and 3 msec for weak ones. About 0.6 msec should be required for the air disturbance to travel this distance. Therefore the average velocity of the first dust is 260 fps for the strong shock and 190 fps for the weak shock, in both instances about 80 per cent of the initial material velocity of the shock wave. However, the actual velocity of the first dust at the gage position should be higher than this since the dust starts from rest. Moreover, it is not surprising that the delay times for pumice and sand are the same since the acceleration times for the finer particles of either material are smaller than the time required for the dust to move from screen to gage.

Having some idea of the velocity of the dust, we may apply Eq D.6 to estimate the range of  $n$  under experimental conditions. The maximum possible value of  $\bar{u}_d$  may be specified as  $u_a$ , the material velocity behind the shock front; we can therefore calculate a minimum value of  $n$ . Setting a lower value of average dust velocity at the gage is more arbitrary. Since the average velocity of the first dust between screen and gage is approximately  $0.8 u_a$ , we have assigned a minimum value of  $0.7 u_a$  for the average dust velocity at the gage with some confidence since the dust behind the first dust is accelerated for a longer time. We may use this value to calculate an approximate maximum value of  $n$ . The maximum and minimum values of  $n$  in Table D.5 have been calculated for these limits of average dust velocity, using dust-pulse durations,  $\Delta t$ , of 3 msec for heavy loads and 2 msec for light loads. Note that maximum values of  $n$  are about one or greater and minimum values one or less.

This analysis may be extended by assuming  $n$  to be about one for the Rutishauser gage. This assumption is justified if we can show that the mean free path of the dust is small compared with the dimensions of the gage face. Since most of the dust is in the dust pulse, the dust density should be about  $m_d/\bar{u}_d\Delta t$ . For heavy loads of fine

UNCLASSIFIED

sand the density would be greater than  $2.5 \text{ mg cm}^{-3}$  since  $\bar{u}_d$  cannot be greater than  $u_a$ . Accordingly the mean free path (approximately  $r_0/3\bar{u}_d$ ) for the average particle radius (2.5 microns) would be less than 0.035 inch as compared with a radius of 0.375 inch for the face of the Rutishauser gage. Calculations for the light load lead to a similar result. Thus the mean free path is short enough to satisfy the limiting conditions. The calculated density is that of the free-stream dust; the actual dust density in front of the gage should be greater because of stagnation effects. Actually it is probably still greater even after the dust pulse has passed that lagging dust particles also have a registering coefficient of about one.

Using the Rutishauser data and assuming that  $n = 1$ , we may calculate the approximate value of  $\bar{u}_d$  from Eq D.6, which averages 266 fps or  $0.81 u_a$  for a strong shock loaded with sand. But since the average velocity of the first dust is about  $0.8 u_a$  for both strong and weak shocks, we may assume a similar relation for the weak shock. Similarly we assume that  $\bar{u}_d = 0.81 u_a$  for pumice with the reservation that the largest particles may not be included. With these values of  $\bar{u}_d$  we may now use Eq D.6 to approximate  $n$  for the Wiancho gage (Table D.5); the average was about one, the standard deviation being 0.3. Deviations appeared to be about random except that  $n$  was greater than one for heavy loads of sand and strong shocks and less than one for weak shocks loaded with sand.

By making additional assumptions we could use Eq D.7 to evaluate  $n$ . Rather than using the expression directly, let us take the information from the prior analysis and use it as a check since the peak dust densities should be about the same for the Rutishauser and Wiancho gages. If we use the same assumptions that were made for the dynamic impulse analysis and evaluate  $n$  as one for the Rutishauser data,  $n$  for the Wiancho gage averages 1.4 for heavy loads of sand and 1.2 for light loads when a strong shock is used. Thus while the dynamic impulse and peak dynamic pressure methods of evaluating  $n$  are in approximate agreement, the second method gives somewhat higher values of  $n$  for the Wiancho gage.

The high values of  $n$  for the Wiancho gage when used with strong shocks and heavy loads of sand may be associated with the discrepancy in shapes of the dynamic pressure curves. A possible explanation is that dust trapped in the gage during the dust pulse impedes release of pressure from the sensing element and results in an apparent increase in registering coefficient. Even if such a relaxation effect exists, however, it should be of little consequence in field work unless the gage is completely plugged, for there the dust pulse would be much longer and could be regarded as nearly a steady-state flow. For field measurements, then, the current best estimate for the Wiancho gage is that  $n = 1$  for the types of dust used for this experiment.

~~CONFIDENTIAL - SECURITY INFORMATION~~

~~Memorandum for the Director~~

~~Department of Defense~~

~~February 1964~~

UNCLASSIFIED

TABLE D.5 -- Summary of Dynamic Impulse Calculations

Shock overpressure* (psi)	Type gage	$\Delta I$ (psi-sec)	Dust load ( $\text{g/cm}^2$ )	$n_{\text{max}}^{\dagger}$	$n_{\text{min}}^{\ddagger}$	$n^{\S}$ calc
Results for fine $\text{SiO}_2$						
7.0	Wiancko	0.0093	0.070	1.4	0.9	1.2
7.0	Wiancko	0.0091	0.063	1.6	0.9	1.3
7.0	Wiancko	0.0026	0.038	0.9	0.4	0.7
7.0	Wiancko	0.0054	0.035	1.7	1.0	1.4
7.0	Rutishauser	0.0115	0.085	1.4	0.7	1.2
7.0	Rutishauser	0.0093	0.085	1.2	0.7	1.0
7.0	Rutishauser	0.0045	0.047	1.1	0.6	0.9
3.8	Wiancko	0.0035	0.070	0.9	0.5	0.7
3.8	Wiancko	0.0019	0.038	0.9	0.5	0.7
Results for pumice						
7.0	Wiancko	0.0060	0.070	1.0	0.5	0.8
7.0	Wiancko	0.0050	0.038	1.5	0.8	1.2
3.8	Wiancko	0.0029	0.035	1.4	0.9	1.1

\*Overpressure before striking screen;  $^{\dagger}$ Calculated on basis that  $\bar{u}_d/u_a = 0.7$ ;  $^{\ddagger}$ Calculated on basis that  $\bar{u}_d/u_a = 1.0$ ;  $^{\S}$ Calculated on basis that  $\bar{u}_d/u_a = 0.81$

#### D.4 CONCLUSIONS AND PLANS FOR FURTHER RESEARCH

While this experiment has given considerable insight into the response of the Wiancko and Rutishauser gages to dust-laden shock waves, most of the conclusions must be regarded as tentative in the light of the comparatively few measurements to date. However, it may be stated with certainty that suspended dust does affect dynamic pressures measured by the gages. A probable expression for the dynamic pressure measured is

$$\text{Dynamic pressure} = \frac{1}{2} \rho_a u_a^2 + n \rho_d u_d^2$$

where  $\rho_a$  and  $\rho_d$  are the air and dust densities and  $u_a$  and  $u_d$  their velocities. For the Rutishauser gage  $n$  should be about one provided the restrictions outlined earlier are satisfied. This experiment has indicated that  $n$  is also about one for the Wiancko gage (standard deviation 0.3). Because of the limited scope of the experiment to date this last conclusion applies only to dust particles having specific gravities of approximately 2.5 and diameters ranging from 1 to 100

**UNCLASSIFIED**

Caution is necessary in using total dynamic pressures measured by an instrument such as the pitot-static gage to calculate forces on an obstacle since no distinction can be made between the contributions of air and dust. At best such measurements can be regarded as an index of the dynamic pressure at the forward stagnation point on an obstacle of size similar to that of the pitot-static gage. The relation between drag forces and dynamic pressures is discussed more fully in Chapter 1. If used to measure pressure distribution, the Wiancko gage would provide satisfactory measurements of the forces on an obstacle in the path of a dust-laden shock wave provided the dust density were such that the mean free path of the dust particles was small compared with the dimensions of the obstacle.

Answers to these and other more general questions of immediate practical significance could be provided by continuing these laboratory tests and increasing their scope. Currently planned extensions of the program include

1. More extensive shock-tube studies of the responses of the gages to a variety of dust types, shock strengths, and screen-gage distances.
2. Studies of the interaction of dust with the shock wave, including different methods of introducing dust into the shock wave.
3. Investigating the effect of dust-air mixtures on obstacles; this problem would seem at present to be more easily attacked from the theoretical point of view, but some experimental work may be done.
4. Application of the results of these studies to determine the effects of dust in nuclear explosions.

**UNCLASSIFIED**

**SECRET**

## APPENDIX E

### DYNAMIC PRESSURES IN DUST-LADEN SHOCKS

Some theoretical relations for dust-laden shock waves are derived here, and dynamic pressures computed therefrom are compared with those measured by this project (Ch 1). An outline of the derivation of the shock relations for clean air is followed by an analogous derivation for dust-laden air. From these derived relations and the knowledge of how dust is registered by the gages are computed the 'theoretical' dynamic pressures used in this comparison.

#### E.1 SHOCK RELATIONS FOR CLEAN AIR

As pointed out in Ch 1, the conservation laws for mass, momentum, and energy at the shock front can be derived by assuming either (1) that the shock front is a discontinuity (of infinitesimal thickness) and not necessarily a case of steady flow or (2) that it is a condition of steady-state flow and not necessarily of infinitesimal thickness. The use to which we have put the shock relations here led us to choose the latter assumption. The conservation laws may be stated as

$$\rho_0 U = \rho (U - u) \quad \text{Mass}$$

$$\rho_0 U u = P - P_0 \quad \text{Momentum}$$

$$\frac{1}{2} (P + P_0)(V_0 - V) = \frac{P V - P_0 V_0}{\gamma - 1} \quad \text{Energy}$$

where  $\rho$  is the air density,  $U$  the shock velocity,  $u$  the particle velocity,  $P$  the absolute pressure,  $V$  the specific volume ( $V = 1/\rho$ ), and  $\gamma$  the ratio of specific heat at constant pressure to that at constant volume. The subscript  $c$  denotes ambient (pres shock) conditions. The shock is presumed to move into still air. From these conservation laws the Rankine-Hugoniot shock relations are obtained:

$$\frac{u}{c_0} = (\gamma - 1) \left[ \frac{\gamma - 1}{\gamma (\gamma + 1)} \right]^{\frac{1}{2}} \quad (E.1)$$

**UNCLASSIFIED**

~~FORMERLY RESTRICTED DATA~~

~~REMOVED FROM THE PUBLIC DOMAIN~~



$$\frac{U}{c_0} = \left[ \frac{\mu \xi + 1}{\gamma(\mu - 1)} \right]^{\frac{1}{2}}, \quad (\text{E.2})$$

$$\frac{c^2}{c_0^2} = \frac{\xi}{\gamma}, \quad (\text{E.3})$$

and

$$\gamma = \frac{\mu \xi + 1}{\xi + \mu} \quad (\text{E.4})$$

where  $c$  is the velocity of sound ( $c^2 = \gamma P/\rho$ ),  $\xi = (\Delta P + P_0)/P_0$ ,  $\gamma = \rho/\rho_0$ , and  $\mu = (\gamma + 1)/(\gamma - 1)$ . Also of interest is the energy,  $E$ , gained by that mass in a unit volume of the shocked medium in passing through the shock front,

$$E = \frac{1}{2} \rho u^2 + \frac{P - P_0}{\gamma - 1} \quad \rho = P(\gamma - 1) \quad (\text{E.5})$$

By combining Eqs E.1 and E.4 we obtain the relation for dynamic pressure:

$$q = \frac{1}{2} \rho u^2 = \frac{1}{2} P_0 \frac{\mu - 1}{\xi + \mu} (\xi - 1)^2 \quad (\text{E.6})$$

For a  $\xi$  less than about 8,  $\gamma$  for air is essentially constant and equal to 1.4. Substituting in Eq E.6 gives

$$q = 2.5 P_0 \frac{(\xi - 1)^2}{\xi + 6}, \quad (\text{E.7})$$

or in terms of  $\Delta P$ ,

$$q = 2.5 \frac{P_0^2}{P_0 + \Delta P}. \quad (\text{E.8})$$

## E.2 SHOCK RELATIONS FOR DUST-LADEN AIR

Derivation of these shock relations is based on the assumptions that (1) each dust particle always has the same velocity as the surrounding air, (2) air and dust temperatures are also the same, and (3) the space occupied by the dust particles is so small compared with the

**UNCLASSIFIED**

volume of air in which they are dispersed that the ideal gas laws still apply to the air component, that is  $V_{\text{air} + \text{dust}} = RT/\rho_{\text{air}}$ . Again we choose to think of applying these relations to the case of steady flow and therefore to shock fronts of finite thickness. Consequently the assumption regarding velocity equilibrium seems reasonable in the light of calculations in Appendix D indicating that the time taken for small particles to reach velocity equilibrium is approximately 1 msec. Likewise Porzel<sup>8/</sup> has shown that the time taken for dust particles of the order of 1 micron in diameter to reach thermal equilibrium is of the order of 1 msec. Since the specific gravity of dust particles is about  $3 \text{ g cm}^{-3}$  as compared with a density of about  $0.001 \text{ g cm}^{-3}$  for air, the space occupied by the dust is small compared with the volume of air it is dispersed in even though the dust density\* is 10 to 20 times that of air.

For dust-laden air the conservation laws<sup>†</sup> are

$$(1 + b) \rho_0' U' = (1 + b) \rho'(U' - u') \quad \text{Mass} \quad (\text{E.9})$$

$$(1 + b) \rho_0' U' u' = P' - P_0' \quad \text{Momentum} \quad (\text{E.10})$$

$$\frac{1}{2}(P' + P_0')(V_0' - V') = \frac{P'V' - P_0'V_0'}{\gamma - 1} + bh(T' - T_0') \quad \text{Energy} \quad (\text{E.11})$$

where  $b$  is the ratio of dust density to air density,  $h$  is the specific heat of the dust,  $T$  is the absolute temperature,  $\rho'$  is the mass of air per unit volume, and  $V' = 1/\rho'$ . Primes are used here to distinguish parameters for dust-laden shocks from those for shocks in clean air. From these conservation laws the following shock relations are obtained:

$$\frac{u'}{c_0'} = (\xi' - 1) \left[ \frac{\mu' - 1}{\gamma'(\mu'\xi' + 1)(1 + b)} \right]^{\frac{1}{2}}, \quad (\text{E.12})$$

$$\frac{U'}{c_0'} = \left[ \frac{\mu'\xi' + 1}{\gamma'(\mu' - 1)(1 + b)} \right]^{\frac{1}{2}}, \quad (\text{E.13})$$

\*Mass of dust per unit volume and not the specific gravity of the individual dust particles.

<sup>†</sup> This treatment is due to Porzel<sup>8/</sup>

UNCLASSIFIED

$$\frac{c'^2}{c_o'^2} = \frac{\xi'}{\eta'} , \quad (\text{E.14})$$

and

$$\eta' = \frac{\mu' \xi' + 1}{\xi' + \mu'} \quad (\text{E.15})$$

where

$$c'^2 = \frac{\gamma' P'}{\rho'} ,$$

$$\gamma' = \frac{\gamma + \frac{bh}{R} (\gamma - 1)}{1 + \frac{bh}{R} (\gamma - 1)} ,$$

and

$$\mu' = \frac{\gamma' + 1}{\gamma' - 1} = \mu + \frac{2bh}{R} .$$

The energy,  $E'$ , gained by that mass contained in a unit volume of the shocked medium in passing through the shock front is

$$E' = \frac{1+b}{2} \rho' u'^2 + \rho' \left[ \frac{P' V' - P_o' V_o'}{\gamma - 1} \right] + \rho' bh (T' - T_o') = P' (\eta' - 1) \quad (\text{E.16})$$

where the first term on the right is the kinetic energy per unit volume in the shocked medium and the second and third terms are the increases in internal energy per unit volume for air and dust, respectively. Substitution from Eqs E.9, E.10, and E.11 reduces these expressions to the simpler form.

The expression for the dynamic pressure of the air component alone is similar to Eq E.6:

$$q_a' = \frac{1}{2} \rho' u'^2 = \frac{P_o}{2} \frac{\mu' - 1}{(1+b)(\xi' + \mu')} (\xi' - 1)^2 . \quad (\text{E.17})$$

Experiments indicate (Appendix D) that the pitot-static gage responds to any dust present as  $\rho_d u_d^2$  where  $\rho_d$  and  $u_d$  are the density and particle velocity of the dust; consequently the total apparent dynamic pressure is

**UNCLASSIFIED**

$$\begin{aligned}
 q' &= \frac{1}{2} \rho' u'^2 + \rho_d u_d^2 \\
 &= \frac{1}{2} \rho' u'^2 (1 + 2b). \quad (E.18)
 \end{aligned}$$

Then the ratio of  $q$  for a dust-laden shock wave of strength  $\xi'$  to that for a shock in clean air of strength  $\xi$  is

$$y = (1 + 2b) \frac{q'}{q} = (1 + 2b) \frac{\rho' u'^2}{\rho u^2}, \quad (E.19)$$

or

$$y = \left( \frac{1 + 2b}{1 + b} \right) \left( \frac{\mu' - 1}{\mu - 1} \right) \left( \frac{\xi' - 1}{\xi - 1} \right)^2 \left( \frac{\xi + \mu}{\xi' + \mu'} \right). \quad (E.20)$$

Let us now digress from our discussion of dynamic pressure long enough to examine the effect of dust loading on shock strength (or overpressure). Forzel's main interest in his treatment of dust-laden shocks<sup>8</sup> was to obtain a relation between the strengths of the same shock in clean and dust-laden air, ie, between  $\xi$  and  $\xi'$ ; to do so he equated the excess energies per unit volume ( $E - E'$ ) behind the shock front in each instance, thus:

$$\xi' \frac{(\mu' - 1)(\xi' - 1)}{\mu' + \xi'} = \xi \frac{(\mu - 1)(\xi - 1)}{\mu + \xi}. \quad (E.21)$$

For shocks moving from clean into dust-laden air this relation gives an approximation of the shock strength,  $\xi'$ , in dusty air, any reflection of energy that might take place in passage from clean air to the dusty medium being neglected.

One might instead equate the energies gained by the material in a unit volume of the medium ahead of the shock in passing through the shock front in each instance, ie,  $E/q = E'/q'$  -- or alternatively, the energy gains per unit time per unit area of material passing through the front,  $EU/q = E'U'/q'$ . Results obtained using the first of these equations differ only slightly from those obtained using Eq E.21, but results from the latter equation seem intuitively unreasonable in that  $\xi'$  would be greater than  $\xi$ .

If we could actually measure  $\xi$ ,  $\xi'$ ,  $q$ , and  $q'$  for a shock wave traveling from clean into dust-laden air, it would be apropos to use Eq E.21 to evaluate  $y$  in Eq E.20 for comparison with dynamic pressure ratios derived from experimentally measured values. However, an experimental check of these relations is possible that does not depend on equating the excess energies. If we set  $\xi = \xi'$ , Eq E.20 permits us to predict the ratio of  $q'$  for a dust-laden shock to  $q$  in clean air

for the same shock strength. This ratio can then be compared with the ratio of the dynamic pressure measured in the precursor to that calculated for clean air from the measured overpressure (cf Ch 1, Table 1.11).

If we set  $\xi = \xi'$  in Eq E.19, we obtain

$$y = \left( \frac{1 + 2b}{1 + b} \right) \left( \frac{\xi + \mu}{\xi + \mu'} \right) \left( \frac{\mu' - 1}{\mu - 1} \right) . \quad (E.22)$$

This ratio has an upper limit that depends only on  $\xi$  as the dust density becomes increasingly larger, for

$$\lim_{b \rightarrow \infty} y = 2 \frac{\xi + \mu}{\mu - 1} . \quad (E.23)$$

For a  $\xi$  of 2 to 3 (the range covered by measurements in the precursor) values of  $y$  are presented in Table E.1 for various dust densities.

TABLE E.1 - Dynamic Pressure Ratios for Various Dust Densities and Shock Strengths

$\xi$	$y$				
	$b = 1$	$b = 2$	$b = \infty$	$b = 10$	$b = \infty$
2	1.90	2.28	2.67	2.90	3.20
3	2.00	2.45	2.98	3.25	3.60

These values of  $y$  are to be compared with those determined experimentally (Table 1.11, Ch 1). For measurements on Shots 10 and 11 these ratios could be said to be in rough agreement with those calculated when  $b = 0.5$  except for those determined from measurements by gage 00740. However, ratios based on measured values are in general somewhat greater than those calculated here. Measured  $q$ 's from gage 00740 and from the two gages on Shot 1 are much higher than are predicted from this simple theory.

Since this theory involves a treatment of conditions at the shock front only, and since in the precursor energy might be expected to feed into the precursor from the higher-pressure regions above it, qualitatively it might be anticipated that this simplified approach would give low predictions. There are two other possible reasons for this discrepancy, however. It may be that the measured  $q$ 's are not correct or that the dust actually registers with a coefficient of more than one. To understand better the phenomena observed, these questions will have

UNCLASSIFIED

to be resolved. An analysis of how much energy is fed into the precursor is in order, but it is certainly beyond the scope of the simplified approach used here.

### E.3 CONCLUSIONS

An outline for the derivation of shock relations for dust-laden shock waves has been presented; the derivation is analogous to that used for shock waves in clean air. Although these relations apply only to the shock front and are subject to several limiting assumptions, they may be used, with the assumption that dust registers as  $\rho_d u_d^2$ , to calculate dynamic pressures for given shock strengths and dust densities. When the theoretically calculated ratios of dynamic pressures for dust-laden shock waves to those for clean air were compared with the ratios measured on Operation UPSHOT-KNOTHOLE, it was found that some of the measured ratios were in reasonable agreement with those calculated by assuming dust densities of the order of 0.5 times the air densities. On the other hand some of the measured ratios were much higher than could be predicted from this simplified theory. Several possible contributory factors to this discrepancy are advanced:

1. Energy fed into the precursor from higher-pressure regions above could increase the dynamic pressure behind the shock front. This energy feed almost certainly takes place to some degree, but how significant it is is not known.
2. The excessively high ratios measured by several of the gages may be grossly in error. More measurements are needed to clarify this point.
3. The dust may register as  $n \rho u^2$ , where  $n$  is greater than 1. Rather elementary theoretical considerations of the mechanics of dust propagation would, however, lead to the feeling that it is unlikely that dust registers with a coefficient appreciably greater than one except for very low dust densities or large particle sizes.

**UNCLASSIFIED**

UNCLASSIFIED

REFERENCES

1. Capabilities of Atomic Weapons, Department of the Army Technical Manual TM 23-200, Revised ed, October 1, 1952 (Secret)
2. Courant, R. and Friedrichs, K. O., Supersonic Flow and Shock Waves, Interscience Publishers, Inc., New York, 1948, pp 120-131
3. Penney, W. G., and Pike, H. H. M., "Shock Waves and the Propagation of Finite Pulses in Fluids," Reports on Progress in Physics, 13, 46 (1950)
4. Chandrasekhar, S., On the Decay of Plane Shock Waves, Ballistic Research Laboratories report 423, 1943 (Unclassified)
5. von Neumann, J., Progress Report on the Theory of Shock Waves, National Defense Research Committee report OSRD-1140, 1943 (Unclassified)
6. von Neumann, J., Oblique Reflection of Shocks, Navy Department Bureau of Ordnance Explosives Research report No. 12 (BuO-ER-12), October 12, 1943 (Unclassified)
7. Polachek, H., and Seeger, R. J., Regular Reflection of Shocks in Ideal Gases, Navy Bureau of Ordnance Explosives Research report No. 13 (BuO-ER-13) February 12, 1944 (Unclassified)
8. Porzel, F. B., Height of Burst for Atomic Bombs, Los Alamos Scientific Laboratory report LA-1406 (to be published); Theoretical Blast Curves (draft copy), J-17837 (letter), May 25, 1953; Theoretical Blast Curves (draft copy), J-19704 (letter), August 26, 1953 (Secret, RD)
9. Aronson, C. J., et al, Free-Air and Ground-Level Pressure Measurements, Operation TUMBLER report WT-513, November 1952 (Secret, RD)
10. Shelton, F. H., The Precursor, Its Formation, Prediction, and Effects, Sandia Corporation report SC-2850(TH), July 27, 1953 (Secret, RD)

UNCLASSIFIED

## UNCLASSIFIED

11. Cook, T. B., and Karmermeyer, K., Sandia Laboratory Shock-Gauge Evaluation Tests, Operation TUMBLER-SNAPPER report WT-505, October 2, 1952 (Confidential, RD)
12. Cowan, M., Jr., Shock-Winds, After-Winds, and Changes in Air Temperature Resulting from Large Atomic Bursts Near the Earth's Surface, Operation IVY report WT-603, May 1953 (Secret, RD)
13. Liepman, H. W., and Puckett, A. E., Aerodynamics of a Compressible Fluid, John Wiley and Sons, New York, 1947, pp 25-27
14. Northrop, P. A., Instrumentation for Structures Program, Part II, Operation GREENHOUSE report WT-10, August 1951 (Secret, RD)
15. Rollosso, G. W., Test Procedures and Instrumentation for Projects 1.1c-1, 1.1c-2, 1.1d, and 1.4, Operation UPSHOT-KNOTHOLE report WT-787, December 1953 (Confidential)
16. Morris, W. E., Air Blast Measurements, Operation UPSHOT-KNOTHOLE report WT-710 (Secret, RD)
17. Pons, W. W., Blast Damage to Coniferous Tree Stands by Atomic Explosions, Operation UPSHOT-KNOTHOLE report WT-731, January 1954 (Confidential, RD)
18. Swift, L. M., Air Pressure vs Time, Operation UPSHOT-KNOTHOLE report WT-711 (Secret, RD)
19. Cook, T. B., and Richardson, H. M., The Response of Wiancko Gauges to Dust-Laden Shock Waves, Sandia Corporation Technical Memorandum No. 148-53-51 (Ref sym 1925-3-(22)), September 14, 1953 (Confidential)
20. Shelton, F. H., and Broyles, C. D., New Pressure-Distance Data for Low Heights of Burst and a Height-of-Burst Chart for Dynamic Pressure in the Precursor Region and for a Surface Detonation, Sandia Corporation Technical Memorandum No. 132-53-51 (Ref sym 1925-3-(14)), August 18, 1953 (Secret, RD)
21. Summary Report on Diagnostic Measurements (W. E. Ogle, Ed), Operation TUMBLER-SNAPPER report WT-550, November 1952 (Secret, RD)
22. Forzel, F. B., Blast Measurements, Operation TUMBLER-SNAPPER report WT-556, August 1952 (Secret, RD)
23. Church, P. K., and Valentine, J. W., Density Gage for Air Shock-Wave Measurements, Sandia Corporation report SC-3004(TR), October 15, 1953 (Unclassified)

UNCLASSIFIED



# UNCLASSIFIED

24. Shreve, J. D., Jr., Air Shock Pressure-Time vs Distance for a Tower Shot, Operation UPSHOT-KNOTHOLE report WT-712, August 1954 (Secret, RD)
25. Foushee, F. C., Sound Velocities Near the Ground in the Vicinity of an Atomic Explosion, Operation UPSHOT-KNOTHOLE report WT-776, December 1953 (Confidential, RD)
26. Church, P. K., A Differential Pressure Type g-Tube, Sandia Corporation report SC-3123(TR), November 23, 1953 (Official Use Only)
27. Broida, T. R., et al, Air Temperatures in the Vicinity of a Nuclear Explosion, Operation TUMBLER report WT-542, September 1, 1952 (Secret, RD)
28. McLoughlin, R. C., Sound Velocity Changes Near the Ground in the Vicinity of an Atomic Explosion, Operation TUMBLER report WT-546, March 1953 (Secret, RD)
29. Vulgan, E. J., "The Wiancko Air-Pressure Gauge," Appendix B to Pressure-Distance-Height Study of 250-lb TMT Spheres, Operation TUMBLER report WT-520, March 13, 1953 (Secret, RD)
30. Williams, M., "Electrokinetic Transducers," Rev. Sci. Inst., 19 640 (October 1948)
31. Bleakney, W., Welmer, D. K., and Fletcher, C. H., "The Shock Tube: A Facility for Investigation in Fluid Dynamics," Rev. Sci. Inst., 20, 807 (October 1949)
32. Fluid Motion Panel, Modern Developments in Fluid Dynamics, Vol II, Oxford University Press, London (1938)
33. Glauert, H., The Elements of Airfoil and Airscrew Theory (2nd ed), University Press, Cambridge (1948)
34. Lamb, H., Hydrodynamics (6th ed), Dover Publications, New York (1932)

~~FORMERLY RESTRICTED DATA~~  
~~\_\_\_\_\_~~  
~~\_\_\_\_\_~~  
~~\_\_\_\_\_~~

UNCLASSIFIED

~~\_\_\_\_\_~~  
~~\_\_\_\_\_~~

UNCLASSIFIED

# DISTRIBUTION

Copy

## ARMY ACTIVITIES

- 1 Asst. Chief of Staff, J-1, D.A., Washington 25, D.C.  
ATTN: Dep. ASST, J-1 (R&D)
- 2 Asst. Chief of Staff, J-4, D.A., Washington 25, D.C.
- 3 Chief of Ordnance, D.A., Washington 25, D.C. ATTN: ORDET AR
- 4-6 Chief Signal Officer, D.A., P&D Division, Washington 25, D.C. ATTN: S130P
- 7 The Surgeon General, D.A., Washington 25, D.C. ATTN: Chief R&D Division
- 8-9 Chief Chemical Officer, D.A., Washington 25, D.C.
- 10 The Quartermaster General, AFM, Liaison Officer, Research and Development Div., D.A., Washington 25, D.C.
- 11-15 Chief of Engineers, D.A., Washington 25, D.C. ATTN: BRMB
- 16 Chief of Transportation, Military Planning and Intelligence Div., Washington 25, D.C.
- 17-19 Chief, Army Field Forces, Ft. Monmouth, Va.
- 20 President, Board of AFM, Ft. Monmouth, Va.
- 21 President, Board of AFM, Ft. Monmouth, Va.
- 22 President, Board of AFM, Ft. Monmouth, Va.
- 23 Commanding General, U.S. Army Caribbean, Ft. Rucker, D.C. ATTN: G-1, G-2
- 24-25 Commander-in-Chief, Far East Command, AFM 200, 200 PM, San Francisco, Calif. ATTN: AFM 200, 200 PM
- 26-27 Commanding General, U.S. Army Europe, AFM 200, 200 PM, New York, N.Y. ATTN: AFM 200, 200 PM
- 28-29 Commandant, Command and General Staff College, Ft. Leavenworth, Kan. ATTN: ALLIG (AS)
- 30 Commandant, The Artillery School, Ft. Sill, Okla.
- 31 Secretary, The AAAH Branch, The Artillery School, Ft. Sill, Okla. ATTN: Lt. Col. Albert D. Spay, Dept. of Justice and Combined Arms
- 32 Commanding General, Medical Field Service School, Brooks Army Medical Center, Ft. Sam Houston, Tex.
- 33 Director, Special Weapons Development Office, Ft. Sill, Okla. ATTN: Lt. Arthur Jostbery
- 34 Commandant, Army Medical Service Graduate School, Walter Reed Army Medical Center, Washington 25, D.C.
- 35 Superintendent, U.S. Military Academy, West Point, N.Y. ATTN: Prof. of Ordnance
- 36 Commandant, Chemical Corps School, Chemical Corps Training Center, Ft. McClellan, Ala.
- 37 Commanding General, Research and Engineering Command Army Chemical Center, MD. ATTN: Deputy for R&E and Test Material
- 38-39 Commanding General, Aberdeen Proving Ground, MD. (Inner envelope) ATTN: RD Central Officer (for Director, Ballistics Research Laboratory)
- 40-42 Commanding General, The Engineer Center, Ft. Belvoir, Va. ATTN: Asst. Commandant, Engineer School
- 43 Commanding Officer, Engineer Research and Development Laboratory, Ft. Belvoir, Va. ATTN: Chief, Technical Intelligence Branch
- 44 Commanding Officer, Plotting / Control, Bore, S.J. ATTN: ODDO-TE
- 45 Commanding Officer, Army Medical Research Laboratory, Ft. Detrick, Md.
- 46-47 Commanding Officer, Chemical Corps Chemical and Biological Laboratory, Army Medical Center, MD. ATTN: Tech. Library
- 48 Commanding Officer, Transportation R&D Station, Ft. Belvoir, Va.
- 49 Director, Technical Documents Center, Space Signal Laboratory, Schriber, S.J.
- 50 Director, Veterinary Experiment Station, PO Box 611, Vicksburg, Miss. ATTN: Library

Copy

- 51 Director, Armed Forces Institute of Pathology, 17th and Independence Avenue, S.W., Washington 25, D.C.
- 52 Director, Operations Research Office, Johns Hopkins University, 1100 Connecticut Ave., Chevy Chase, Md. ATTN: Library
- 53-54 Technical Information Service, Oak Ridge, Tenn. (Surplus)

## NAVY ACTIVITIES

- 55-56 Chief of Naval Operations, D.N., Washington 25, D.C. ATTN: OP-10
- 57 Chief of Naval Operations, D.N., Washington 25, D.C. ATTN: OP-10 (USC)
- 58 Director of Naval Intelligence, D.N., Washington 25, D.C. ATTN: OP-10 (USC)
- 59 Chief, Bureau of Medicine and Surgery, D.N., Washington 25, D.C. ATTN: Special Weapons Defense Div.
- 60 Chief, Bureau of Ordnance, D.N., Washington 25, D.C.
- 61 Chief, Bureau of Ships, D.N., Washington 25, D.C. ATTN: Code 300
- 62 Chief, Bureau of Yards and Docks, D.N., Washington 25, D.C. ATTN: D-440
- 63 Chief, Bureau of Supplies and Accounts, D.N., Washington 25, D.C.
- 64-70 Chief, Bureau of Aeronautics, D.N., Washington 25, D.C.
- 71 Chief of Naval Research, Department of the Navy, Washington 25, D.C. ATTN: L11 (a) F. McRae, USN
- 72 Commander-in-Chief, U.S. Pacific Fleet, Fleet Post Office, San Francisco, Calif.
- 73 Commander-in-Chief, U.S. Atlantic Fleet, U.S. Naval Base, Norfolk 11, Va.
- 74-77 Commandant, U.S. Marine Corps, Washington 25, D.C. ATTN: Code 403
- 78 President, U.S. Naval War College, Newport, R.I.
- 79 Superintendent, U.S. Naval Postgraduate School, Monterey, Calif.
- 80 Commanding Officer, U.S. Naval Schools Command, U.S. Naval Station, Treasure Island, San Francisco, Calif.
- 81 Commanding Officer, U.S. Fleet Training Center, Naval Base, Norfolk 11, Va. ATTN: Special Weapons School
- 82-87 Commanding Officer, U.S. Fleet Training Center, Naval Station, San Diego 3, Calif. ATTN: (SPW School)
- 88 Commanding Officer, Air Development Squadron 3, FL-3, U.S. Naval Air Station, Moffett Field, Calif.
- 89 Commanding Officer, U.S. Naval Damage Control Training Center, Naval Base, Philadelphia 12, Pa. ATTN: AD Defense Course
- 90 Commanding Officer, U.S. Naval Unit, Chemical Corps School, Army Chemical Training Center, Ft. McClellan, Ala.
- 91 Joint Landing Force Board, Marine Barracks, Camp Lejeune, N.C.
- 92 Commander, U.S. Naval Ordnance Laboratory, Silver Spring 19, MD. ATTN: 88
- 93 Commander, U.S. Naval Ordnance Laboratory, Silver Spring 19, MD. ATTN: 88
- 94 Commander, U.S. Naval Ordnance Laboratory, Silver Spring 19, MD. ATTN: 8
- 95 Commander, U.S. Naval Ordnance Test Station, Inglewood, Calif. ATTN: 88
- 96 Officer-in-Charge, U.S. Naval Civil Engineering Res. and Development Lab., U.S. Naval Construction Battalion Center, Port Hueneme, Calif. ATTN: Code 700
- 97 Commanding Officer, U.S. Naval Medical Research Inst., National Naval Medical Center, Bethesda 14, Md.

UNCLASSIFIED

UNCLASSIFIED

Copy

~~CONFIDENTIAL~~

- 100-101 Laboratory, Washington
- 100-102 Commanding Officer and Director, U.S. Navy Electronics Laboratory, San Diego 52, Calif. ATTN: Code 4223
- 100-103 Commanding Officer, U.S. Naval Radiological Defense Laboratory, San Francisco 24, Calif. ATTN: Technical Information Division
- 100-104 Commanding Officer and Director, David W. Taylor Naval Basin, Washington 7, D.C. ATTN: Library
- 100-105 Commander, U.S. Naval Air Development Center, Johnsville, Pa.
- 100-106 Director, Office of Naval Research Branch Office, 1000 Jeary St., San Francisco, Calif.
- 100-107 Technical Information Service, Oak Ridge, Tenn. (Surplus)

AIR FORCE ACTIVITIES

- 110-108 Asst. for Atomic Energy, Headquarters, USAF, Washington 25, D.C. ATTN: D28/O
- 110-109 Director of Operations, Headquarters, USAF, Washington 25, D.C. ATTN: Operations Analysis
- 110-110 Director of Plans, Headquarters, USAF, Washington 25, D.C. ATTN: War Plans Div.
- 110-111 Director of Research and Development, Headquarters, USAF, Washington 25, D.C. ATTN: Combat Component Div.
- 110-112 Director of Intelligence, Headquarters, USAF, Washington 25, D.C. ATTN: AFOTB-134
- 110-113 The Surgeon General, Headquarters, USAF, Washington 25, D.C. ATTN: Sig. Def. Br., Pro. Med. Div.
- 110-114 Asst. Chief of Staff, Intelligence, Headquarters, U.S. Air Force Europe, APO 813, c/o PM, New York, N.Y. ATTN: Air Intelligence Branch
- 110-115 Commander, 477th Reconnaissance Technical Squadron (Augmented), APO 813, c/o PM, New York, N.Y.
- 110-116 Commander, For Best Air Force, APO 813, c/o PM, San Francisco, Calif.
- 110-117 Commander, Strategic Air Command, Offutt Air Force Base, Omaha, Nebraska. ATTN: Special Weapons Branch, Inspection Div., Inspector General
- 110-118 Commander, Tactical Air Command, Langley AFB, Va. ATTN: Documents Security Branch
- 110-119 Commander, Air Defense Command, Bnt AFB, Colo.
- 110-120 Commander, Air Materiel Command, Wright-Patterson AFB, Dayton, O. ATTN: WTAIDS
- 110-121 Commander, Air Training Command, Scott AFB, Bellville, Ill. ATTN: D28 O JFF
- 110-122 Commander, Air Research and Development Command, PO Box 1147, Baltimore, Md. ATTN: RCDH
- 110-123 Commander, Air Proving Ground Command, Eglin AFB, Fla. ATTN: APTB
- 110-124 Commander, Air University, Maxwell AFB, Ala.
- 110-125 Commander, Flying Training Air Force, Vance, Tex. ATTN: Director of Observer Training
- 110-126 Commander, Crew Training Air Force, Randolph Field, Tex. ATTN: APTB, D28 O
- 110-127 Commander, Headquarters, Technical Training Air Force, Jointport, Miss. ATTN: T2AD
- 110-128 Commandant, Air Force School of Aviation Medicine, Randolph AFB, Tex.

Copy

- 140-129 Commander, Wright Air Development Center, Wright-Patterson AFB, Dayton, O. ATTN: WYDEP
- 140-130 Commander, Air Force Cambridge Research Center, 230 Albany Street, Cambridge 39, Mass. ATTN: CBR, Atomic Warfare Directorate
- 140-131 Commander, Air Force Cambridge Research Center, 230 Albany Street, Cambridge 39, Mass. ATTN: CRGRT-2
- 140-132 Commander, Air Force Special Weapons Center, Kirtland AFB, N. Mex. ATTN: Library
- 140-133 Commandant, USAF Institute of Technology, Wright-Patterson AFB, Dayton, O. ATTN: Resident College
- 140-134 Commander, Lowry AFB, Denver, Colo. ATTN: Department of Armament Training
- 140-135 Commander, 1007th Special Weapons Squadron, Headquarters, USAF, Washington 25, D.C.
- 140-136 The RAND Corporation, 1700 Main Street, Santa Monica, Calif. ATTN: Nuclear Energy Division
- 140-137 Technical Information Service, Oak Ridge, Tenn. (Surplus)

OTHER DEPARTMENT OF DEFENSE ACTIVITIES

- 160-138 Asst. Secretary of Defense, Research and Development, D/O, Washington 25, D.C.
- 160-139 U.S. National Military Representative, Headquarters, SHAPE, APO 99, c/o PM, New York, N.Y. ATTN: Col. J. P. Bealy
- 160-140 Director, Weapons Systems Evaluation Group, OSD, RM 78100, Pentagon, Washington 25, D.C.
- 160-141 Asst. for Civil Defense, OSD, Washington 25, D.C.
- 160-142 Armed Services Explosive Safety Board, D/O, Building T-7, Brooklyn Point, Washington 25, D.C.
- 160-143 Commandant, Armed Forces Staff College, Norfolk 11, Va. ATTN: Secretary
- 170-144 Commanding General, Field Command, Armed Forces Special Weapons Project, PO Box 5100, Albuquerque, N. Mex.
- 170-145 Chief, Armed Forces Special Weapons Project, PO Box 5100, Washington 13, D.C.
- 180-146 Commanding General, Field Command, Armed Forces Special Weapons Project, PO Box 5100 Albuquerque, New Mex. ATTN: Tech. Training Group
- 180-147 Technical Information Service, Oak Ridge, Tenn. (Surplus)

ATOMIC ENERGY COMMISSION ACTIVITIES

- 190-148 U.S. Atomic Energy Commission, Classified Technical Library, 1901 Constitution Ave., Washington 25, D.C. ATTN: Mr. J. H. O'Leary (For RDB)
- 190-149 Los Alamos Scientific Laboratory, Argonne Library, PO Box 1603, Los Alamos, N. Mex. ATTN: Helen Bodman
- 190-150 Sandia Corporation, Classified Document Division, Sandia Base, Albuquerque, N. Mex. ATTN: Martin Lupton
- 210-151 University of California Radiation Laboratory, PO Box 808, Livermore, Calif. ATTN: Margaret Beland
- 210-152 Weapon Data Section, Technical Information Service, Oak Ridge, Tenn.
- 210-153 Technical Information Service, Oak Ridge, Tenn. (Surplus)

~~CONFIDENTIAL~~

UNCLASSIFIED





Defense Special Weapons Agency  
6801 Telegraph Road  
Alexandria, Virginia 22310-3398

OPSSI

MAY 8 1998

MEMORANDUM FOR DISTRIBUTION

SUBJECT: Declassification Review of Operation UPSHOT-KNOTHOLE Test Reports

The following 90 reports concerning the atmospheric nuclear tests conducted during Operation UPSHOT-KNOTHOLE in 1953 have been declassified and cleared for open publication/public release:

WT-702, WT-703, WT-705, WT-709 thru WT-711, WT-713 thru WT-719, WT-721 thru WT-742, WT-744 thru WT-746, WT-749 thru WT-755, WT-757 thru WT-761, WT-763, WT-764, WT-766 thru WT-781, WT-784 thru WT-787, WT-789, WT-790, WT-792 thru WT-796, WT-798, WT-801, WT-805, WT-808, WT-809, WT-811, WT-812, WT-814, WT-817, WT-820, and WT-822

An additional 6 WTs from UPSHOT-KNOTHOLE have been re-issued with deletions and are identified with an "EX" after the WT number. These reissued versions are unclassified and approved for open publication. They are:

WT-743, WT-747, WT-802, WT-810, WT-825, and WT-828

This memorandum supersedes the Defense Special Weapons Agency, OPSSI memorandum same subject dated June 11, 1997 and may be cited as the authority to declassify copies of any of the reports listed in the first paragraph above.

RITA M. METRO  
Chief, Information Security

DISTRIBUTION:  
See Attached